

Editorial corner – a personal view

Carbon nanotubes – attractive nanofillers for forming bio-, functional and structural polymer composites

*S. C. Tjong**

Department of Physics and Materials Science, City University of Hong Kong, Tat Chee Avenue, Kowloon, Hong Kong

Carbon nanotubes (CNTs) have attracted increasing interest from researchers due their exceptional mechanical, electrical and thermal properties. Polymer resins (thermoplastics, thermosets, elastomers) filled with low CNT contents exhibit superior mechanical strength and stiffness as well as excellent toughness (in some cases). Accordingly, the structures, mechanical and thermal properties of polymer/CNT composites have been extensively studied. Homogeneous dispersion of CNTs in the polymer matrix is a prerequisite for obtaining improved mechanical properties. Covalent and non-covalent functionalization of CNTs can enhance their dispersion in the polymer matrix.

Apart from their uses as structural materials, polymer/CNT composites also find potential applications in electromagnetic interference shielding, bipolar plates for fuel cells, chemical sensors, etc. The exceptional high electrical conductivity and large aspect ratio of carbon nanotubes render them attractive nanofillers for forming conducting nanocomposites with multifunctional properties. CNTs with large aspect ratios enable formation of conducting path network in the polymer matrix with very low percolation threshold. This is in sharp contrast to conventional microcomposites in which large filler contents are needed to achieve desired electrical properties. The conductivity and dielectric properties of polymer/CNT nanocomposites can be tailored over several orders of magnitude by proper aligning CNTs under electric or magnetic fields. It is noted that chemical functionalization of

CNTs frequently degrades the conductivity due to electron localization. In general, multi-wall carbon nanotubes synthesized by a chemical vapor process are more cost effective than single-wall nanotubes for technological applications.

CNTs have been reported to promote osteoblasts (bone forming cells) and neurons proliferation, and found to be effective nanocarriers for several biomolecules such as proteins, DNA and carbohydrates. Recently, polymer/CNT nanocomposites have been explored as scaffolds for cell growth and load-bearing implant materials for replacing defective human bones. However, some researchers reported that CNTs exhibit cytotoxicity to human dermal cells. Potential health hazard could also arise from the inhalation exposure. The discrepancy in such biocompatibility results can be attributed to the complicated physicochemical interactions between carbon nanotubes and biological cells, and to different cell viability methods and CNT sources. More efforts are needed to solve these issues prior to the incorporation of polymer/CNT nanocomposites into human body.



Prof. Dr. Sie Chin Tjong
Member of International Advisory Board

*Corresponding author, e-mail: aptjong@cityu.edu.hk
© BME-PT

Simulated body fluid and water absorption effects on poly(methyl methacrylate)/hydroxyapatite denture base composites

W. L. Tham, W. S. Chow*, Z. A. Mohd Ishak

School of Materials and Mineral Resources Engineering, Engineering Campus, Universiti Sains Malaysia, Nibong Tebal, 14300 Penang, Malaysia

Received 4 March 2010; accepted in revised form 13 May 2010

Abstract. Poly(methyl methacrylate) (PMMA)/hydroxyapatite (HA) composite has potential application in denture base materials. The denture base materials should exhibit good mechanical properties and dimensional stability in moist environment. Silane coupling agent [3-methacryloxypropyltrimethoxy silane (γ -MPS)] was used to treat the HA fillers in order to enhance the interfacial interaction between the PMMA and HA. In this research, the kinetics and effects of Simulated Body Fluid (SBF) and water absorption on the flexural properties of PMMA/HA composites were studied for an immersion duration of 2 months. The mathematical treatment used in analyzing the data was the single free phase model of diffusion, which assumed Fickian diffusion and utilized Fick's second law of diffusion. The kinetics of water absorption of the PMMA/HA composites conformed to Fickian law behavior, whereby the initial moisture absorption follows a linear relationship between the percentage gain at any time t and $t^{1/2}$, followed by saturation. It was found that the equilibrium moisture content and the diffusion coefficient are depending on the concentration of γ -MPS in PMMA/5HA composites. The reduction of equilibrium moisture content of PMMA/5HA is due to the hydrophobic behavior of γ -MPS and compatibility of PMMA with HA. The retention ability in flexural modulus and strength of PMMA/HA composites upon subjected to water absorption are considerably good. The reduction of flexural strength of the PMMA/HA composites after water absorption and SBF absorption could be attributed to the plasticizing effect of water molecules.

Keywords: polymer composites, poly(methyl methacrylate), hydroxyapatite, water absorption, mechanical properties

1. Introduction

Poly(methyl methacrylate) (PMMA) has been widely used as a biomaterial in dentistry, orthopedic retainers, bone replacement, and eyeballs [1]. PMMA continues to be used as denture base materials because of its favorable characteristics, ease of processing, stability in the oral environment, ease in repair and superior esthetics [2–3]. However, the primary problem of PMMA is its poor strength characteristics, low impact strength and fatigue resistance [4]. Thus, there is a need to improve the performance of PMMA in denture base application. Several methods have been used to modify the

properties of PMMA denture base materials. Approaches to strengthening the acrylic resin prosthesis have included modifying or reinforcing the resin by using filler and fiber, and graft copolymerization with high-impact resins [2–3]. Some effort has been made to increase the impact strength by the incorporation of a rubber phase in the PMMA, however, such materials have compromised flexural properties [5]. Hydroxyapatite (HA) [$\text{Ca}_{10}(\text{PO}_4)_6(\text{OH})_2$] was used in various biomedical fields such as dental material, bone substitute and hard tissue paste [6]. Hydroxyapatite (HA)-reinforced polymers have many potential clinical appli-

*Corresponding author, e-mail: shyang@eng.usm.my
© BME-PT

cations, e.g. bone cement, dental implants, coating of joint replacement prosthesis etc. [7]. The mechanical properties of PMMA/HA composites could be limited by the incompatibility between the PMMA and HA. Thus modification of PMMA/HA composites is required in order to achieve a high performance denture base materials with better mechanical properties. Polymeric compatibilizer and coupling agent can play a role to improve the interaction and adhesion between the organic PMMA matrix and inorganic HA particles. From our previous work, it was found that the silane coupling agent [3-methacryloxypropyltrimethoxy silane (γ -MPS)] can improve the mechanical and thermal properties of PMMA/HA significantly owing to the better adhesion.

The use of heat-polymerized, permanent, acrylic resin denture bases has certain advantages owing to their strong and rigid behavior, in which, they should provide the retention and stability of the final denture [8]. Water absorption of PMMA/HA composite is an important study for dentistry science. In oral environment, dental restorative materials are exposed to saliva containing water. Sometimes, the dental materials are exposed to exogenous substances such as acids, base, salts, alcohols, oxygen, during drinking or eating. Water absorption caused plasticization, lowering of the glass transition temperature (T_g) and may affect the mechanical properties of the polymeric denture based materials. Hydrolytic degradation of the hygroscopic filler may occur when subjected to water absorption [9]. Excessive water uptake may lead to breakdown of the polymer itself, debonding of filler from matrix substance, chemical composition changes by leaching and lead to the ingress of microorganism [10]. Besides, precipitation and swelling phenomena may produce voids and cracks, leaching the interface results in the loss of strength due to corrosion. All of these processes may lead to nucleation and growth of microcracks [11]. Moreover, due to the low molecular weights and high solubility of residual unreacted monomer such as triethyleneglycol-dimethacrylate (TEGDMA) and 2-hydroxyethyl methacrylate (HEMA), may be released from swollen dental adhesives through dental tubules and elicit adverse biological reactions. Dissolution of components from the adhesive material itself can have a poten-

tial impact on its structural stability and consequently expedite the degradation of the resin-dentin bonds [12]. The uptake of water by an unfilled resin is a free volume and thermodynamics-controlled process [9]. A large number of air voids was observed in the posterior composites and this probably leads to high water absorption. Air voids incorporated in the materials may result in higher water solubility. The presence of polar and hydrophilic functional groups in acrylic resins may increase their polarity and facilitate uptake of bound water to form primary and secondary hydration shells around the polar groups via hydrogen bonding [13].

Simulated Body Fluid (SBF) test, a method that is well recognized to characterize the *in vitro* bioactivity of ceramic materials, consists in their immersion in an aqueous SBF solution which simulates the properties of human plasma for certain period and verifies the formation of the hydroxyapatite (HA) layer on the surface of the samples [14]. The quantity of water molecules and SBF absorbed by the resin matrix of dental resin based composite and the rate of water sorption have been identified as being diffusion controlled. The kinetics of water absorption of the resin based composites conformed to Fickian law behavior in general agreement with the plots of percentage of water uptake [%] against any time $t^{1/2}$ remained linear in the initial stages of water absorption followed by a decrease in the rate of diffusion [15]. Theoretically, the water sorption process is determined by the diffusion coefficient and the boundary conditions at the surface of the material. It is an estimation method of the diffusion coefficient using the solution of Fick's second law [16]. Denture base acrylic resins are subjected to many various types of intraoral and extraoral stresses and water contact, e.g. immersion in water-based solution for cleaning purpose, contact with drinking water (hot and cold) and etc. The mechanical properties of PMMA/HA denture base materials during their service life is important. This paper reports on the effects of water absorption and SBF on the properties of PMMA/HA composites with and without surface treatment by silane coupling agent. The maximum moisture absorption (M_m) and diffusion coefficient (D) of PMMA/5HA composites upon subjected to water absorption and SBF will be determined.

2. Materials and methods

2.1. Materials

The solid components consist of PMMA with typical molecular weight of 996 000 (Product no: 182265, Sigma Aldrich, USA) and 0.5% benzoyl peroxide (BPO) (Product no: 801641, Merck Chemical, Germany). The monomers used consist of methyl methacrylate (MMA) (Product no: M 55909, Sigma Aldrich, USA) stabilized with 10–100 ppm monomethyl ether hydroquinone as inhibitor and ethylene glycol dimethacrylate (EGDMA) (Product no: 335681, Sigma Aldrich, USA). Hydroxyapatite (HA) in powder forms was supplied by Sigma Aldrich (USA) (Product no: 289396) with an average specific surface area (BET) 50 m²/g and average particle diameter of 18 μm. The γ-MPS was supplied by Sigma Aldrich (USA) with 98% purified contents.

2.2. Silanization of hydroxyapatite particles

The HA filler was silanized using 3-methacryloxypropyltrimethoxy silane (γ-MPS) in 90% methanol and 10% distilled water. The γ-MPS was diluted in water-methanol solution, with pH of 4 to 5, which adjusted with acetic acid. The Equation (1) gives the amount of required silane to obtain minimum uniform coverage of the filler particles (X) [17–18]:

$$X = \left(\frac{A}{w} \right) f \quad (1)$$

where A is the surface area of the HA filler (50 m²/g) and f is the amount of HA. It was found that each silane molecule covers 1.11 nm² of filler and so that the surface area coverage per gram of MPS is $w = 2525 \text{ m}^2 \cdot \text{g}^{-1}$. According to Söderholm and Shang [19], each MPS molecule occupied at least 1.11 nm² for pyrogenic colloidal silica (Cab-O-Sil). Karabela and Sideridou [17] reported that for the Aerosil silica nanoparticles (with the specific surface area (BET) in the range of 35–65 m²/g), the silane molecule covers 1.11 nm² of filler and, thus the surface area coverage per gram of MPS is $w = 2525 \text{ m}^2 \cdot \text{g}^{-1}$. Four different concentrations of γ-MPS (i.e. 2, 4, 6 and 8% based on the weight of HA filler) were used to modify HA. Figure 1 shows the possible silanization mechanism of HA by γ-MPS, and the interaction between PMMA, HA and γ-MPS.

2.3. Preparation of PMMA/5HA composites

The powder component was prepared by mixing of PMMA, 5% HA and 0.5% BPO. The liquid component was prepared by mixing MMA monomer and EGDMA with a predetermined ratio of 9:1. The ratio of powder to liquid was set at 10:4 according

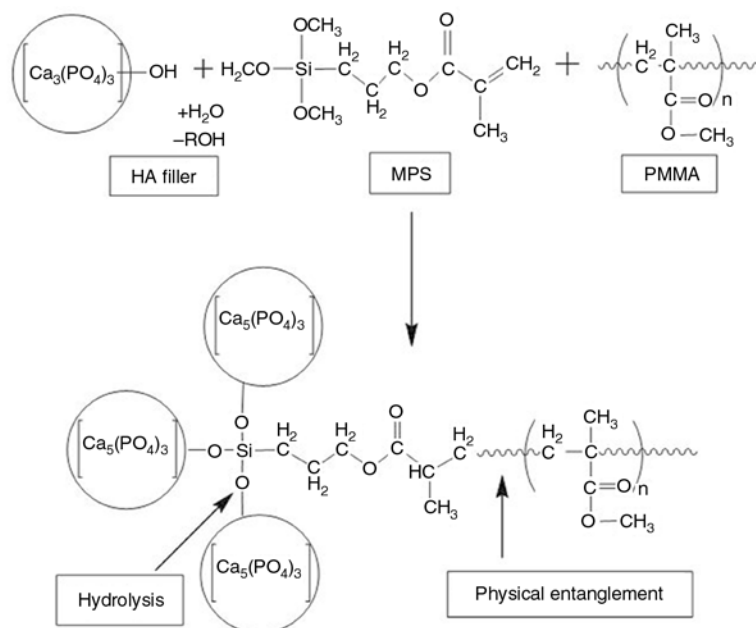


Figure 1. Possible interaction of γ-MPS, HA and PMMA

to the dental laboratory practice. The powder and liquid components were mixed together. After achieving the dough stage, the mixture was packed into a mold with the pressure of 14 MPa using compressor at room temperature for 25 min. The polymerization was carried using a water bath at 78°C and 90 min.

2.4. Characterization of PMMA/5HA composites

2.4.1. Flexural test

Three-point bending tests were performed according to ASTM D790 using an Instron 3366 machine (USA). The support span length was set at 50 mm. The crosshead speed was set at 2 mm/min. At least five samples for each formulation were examined. The flexural modulus and flexural strength were recorded.

2.4.2. Water absorption

The water absorption tests were conducted according to ASTM D 570-98. Specimens as flexural bars were dried in a vacuum oven at 70°C until a constant weight was attained. Specimens (i.e. PMMA, PMMA/5HA composites and PMMA/ γ -MPS treated 5HA composites) were placed in a container of distilled water at temperature of 27°C. The weight gain of the specimens was measured as a function of time after removing the water on their surfaces. The percentage gain at time t , (M_t) as a result of moisture absorption was determined by Equation (2):

$$M_t = \frac{W_w - W_d}{W_d} \cdot 100\% \quad (2)$$

where W_d and W_w denote the initial weight of specimen prior to exposure to the water absorption and weight of specimen after exposure to water absorption, respectively.

$$\frac{M_t}{M_m} = 1 - \frac{8}{\pi^2} \exp\left[-\left(\frac{Dt}{h^2}\right)\pi^2\right] \quad (3)$$

For Equation (3), the maximum moisture absorption (M_m) was calculated as an average value of several consecutive measurements that showed no

appreciable additional absorption, h is the thickness of the specimens and D is the diffusion coefficient. The diffusion coefficient was calculated using Equation (4):

$$D = \frac{\pi h^2 (M_2 - M_1)^2}{16 M_m^2 (t_2^{1/2} - t_1^{1/2})^2} \quad (4)$$

2.4.3. Simulated Body Fluid (SBF) absorption

SBF absorption test was carried out according to ISO specification 1567-2001. The specimens (in flexural bars geometry) were dried in a vacuum oven at 70°C until a constant weight was attained. The specimens were then placed in a container of SBF. The containers were then put in water bath at temperature of 37°C. The SBF was supplied by B-Braun Medical Industries (Penang, Malaysia). The weight gain of the specimens was measured as a function of time after removing the water on their surfaces. The percentage gain at time t , (M_t) as a result of SBF absorption was determined by Equation (2) and diffusion coefficient was calculated using Equation (4).

2.4.4. Field Emission Scanning Electron Microscopy (FESEM)

The morphological studies of flexural bar samples were carried out on FESEM Supra 35VP (Carl Zeiss, Germany) equipped with the Gemini column. The acceleration voltage used was 5 kV. The specimens' surface was coated by Aurum/Palladium alloy in order to prevent electrostatic discharge.

2.5. Statistical analysis

The flexural test data reported in the Table 2 and 3 represent the mean values and standard deviation of replicates. The data were statistically analyzed with a one-way analysis of variance (ANOVA) to determine significant differences was used at a significant level set at $p \leq 0.05$, for analysis of the results. It was followed by the univariate analysis of variance to identify the tests of between-subjects effects.

3. Results and discussions

3.1. Kinetics of water absorption

Figure 2 shows the effect of γ -MPS concentration on the water uptake of PMMA/5HA composites during water absorption at room temperature. It can be seen that the percentage of water uptake of the PMMA/5HA composites is higher than that of PMMA and PMMA/ γ -MPS treated 5HA composites. The maximum moisture absorption (M_m) was reached after 2 months of water absorption. The water sorption, water solubility and associated diffusion coefficient of dental resin-based composite materials are dependent on the chemistry of the monomer resins and the extent of polymerization of the polymer matrix, the present of solubility impurities, filler particles size, filler distribution, and the interfacial properties between filler with resin matrix [10, 15, 20]. According to Harper *et al.* [21], the weight change of the specimens was the combination of increase in weight due to water absorption and loss in weight caused by leaching of the monomer. Table 1 shows the percentage of maximum moisture absorption (M_m) and diffusion coefficient (D) of PMMA, PMMA/5HA composites and PMMA/ γ -MPS treated 5HA composites. The M_m of PMMA/5HA composites is approximately 2.12%, while the M_m of PMMA is about 1.71%. The notable weight gain of PMMA/5HA compos-

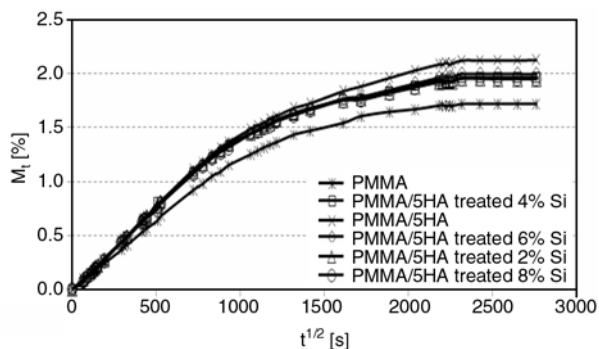


Figure 2. The effects of γ -MPS concentration on the water uptake of PMMA upon subjected to water absorption

ites can be attributed to the presence of the HA filler. The moisture absorption of HA is due to the free and reactive hydroxyl groups on the HA particles which exhibit good affinity to water molecules. Besides, there are micro-voids in between PMMA and HA caused by the difference in the chemical nature of PMMA and HA. This phenomenon is attributed to poorly bonded area and weak interfacial adhesion between the hydrophilic HA filler and the hydrophobic PMMA. Therefore, water molecules could penetrate into these micro-voids or accumulated at the filler-matrix interface. A similar phenomenon was observed by Yang *et al.* [22] in LDPE composites containing 30% lignocellulosic filler. Excessive water uptake can promote breakdown causing a filler-matrix debonding in the presence of porosity and inclusions of filler particle aggregates. This phenomenon would be involved in the water absorption as they appear loosely embedded in the matrix. The amount of water can be accumulated at the interface between these agglomerates and the matrix. However, the presence of the γ -MPS introduced a hydrophobic layer on HA particle surfaces, thus the percentage of water uptake was slightly decreased compared to PMMA/5HA composites. According to Santos *et al.* [23], during the silanization process, multiple layers of silane form a film around the filler particles, which is either physically or chemically attached to the filler particles, and thus limits the water absorption.

Fickian diffusion and Fick’s second law of diffusion was used to determine the diffusivity parameter. From Table 1, it can be seen that the M_m of PMMA/ γ -MPS treated 5HA composite is lower than that of PMMA/5HA composites. Although all the PMMA/5HA composites (with and without silane coupling agents) shows M_m value higher than pure PMMA. However, it is interesting to note that the diffusion coefficient (D) of PMMA/5HA composites is lower than that of PMMA. The mecha-

Table 1. Maximum moisture content (M_m) and diffusion coefficient (D) of PMMA, PMMA/5HA composites and PMMA/ γ -MPS treated 5HA composites after being subjected to water absorption and SBF tests

Material	M_m [%]		D [m^2/s]	
	Water absorption	SBF absorption	Water absorption	SBF absorption
PMMA	1.71	1.96	$1.25 \cdot 10^{-12}$	$1.64 \cdot 10^{-12}$
PMMA/5HA	2.12	2.36	$1.07 \cdot 10^{-12}$	$1.94 \cdot 10^{-12}$
PMMA/5HA treated 2% Si	1.95	2.02	$1.04 \cdot 10^{-12}$	$1.95 \cdot 10^{-12}$
PMMA/5HA treated 4% Si	1.96	2.06	$1.01 \cdot 10^{-12}$	$1.91 \cdot 10^{-12}$
PMMA/5HA treated 6% Si	2.00	2.14	$1.03 \cdot 10^{-12}$	$1.82 \cdot 10^{-12}$
PMMA/5HA treated 8% Si	1.95	2.06	$1.00 \cdot 10^{-12}$	$1.83 \cdot 10^{-12}$

nism through which water diffuses into polymeric materials can be explained as either infiltration into the free space (i.e. micro-voids and other morphological defects) or specific molecular interaction being controlled by the available hydrogen bond at hydrophilic sites [24]. According to Tang *et al.* [25], this may be related to the barrier contribution of filler inclusions to water transportation. Accordingly, when the transportation paths of the water molecules and the water interaction within the composites increase, it will reduce the diffusion coefficient of the composites. The slightly decrease of the diffusion coefficient for PMMA/ γ -MPS treated 5HA composites compared to PMMA/5HA composites may suggest the reduction of microvoids for water accumulation and a hydrophobic behavior due to better interaction of HA filler and PMMA matrix by silanization of HA.

3.2. Effects of water absorption on the flexural properties of PMMA composites

Table 2 shows the flexural properties of the PMMA, its composites in control, wet and redried states after being subjected to water absorption for 1 and 2 months. It can be seen that the flexural modulus of PMMA/ γ -MPS treated HA composites decreased slightly after being subjected to water absorption for 1 month. There is no further significant reduction of the flexural modulus of PMMA composites after being subjected for 2 months to

water absorption for re-dried samples. Table 2 also shows the percentage of recovery of the flexural modulus for the PMMA composites. The recovery of flexural modulus for PMMA composites is excellent. This can be seen from Table 2 that the flexural modulus of re-dried samples is almost comparable to that of the wet sample. According to Matinlinna and Vallittu [26], sometimes the siloxane films of adequate bonding quality can still be formed since the remaining non-hydrolyzed alkoxy groups are assumed to become hydrolyzed in air and thus activated. When these PMMA/ γ -MPS treated HA composites are immersed in water, the inorganic hydroxyl surface of HA may further react with the remaining and available hydrolysable alkoxy groups of γ -MPS. Thus, the increment of flexural modulus and strength for PMMA composites may be associated to the post-chemical reaction during re-drying process. Similar results were reported by Harper *et al.* [21], the increase in strength of poly(ethyl methacrylate) cement after 12 weeks immersion may be due to water being redistributed at that time, which is caused by post curing. Reis *et al.* [27] had reported that denture base acrylic resin after water storage for 30 days, there was an increased in flexural strength. This could be explained by continuous polymerization of polymers. Residual monomer may act as a plasticizer and thus, residual monomer leached from the specimens could also contribute to the increase in flexural strength after water storage.

Table 2. Flexural properties of PMMA, PMMA/5HA composites and PMMA/ γ -MPS treated 5HA composites in wet and re-dried states after being subjected to water absorption for various condition ($n = 3$)

Material	Flexural properties	Control	Duration of immersion			
			1 month		2 months	
			Wet	Redried	Wet	Redried
PMMA	Flexural modulus [GPa]	2.3	2.4 (103.3)	2.6 [113.2]	2.5 (110.3)	2.8 [122.4]
	Flexural strength [MPa]	77.7	90.0 (115.8)	72.2 [92.8]	71.9 (92.6)	73.2 [94.3]
PMMA/5HA	Flexural modulus [GPa]	2.5	2.5 (104.4)	2.8 [110.1]	2.6 (103.5)	3.1 [122.1]
	Flexural strength [MPa]	50.5	57.6 (114.0)	57.3 [113.6]	45.7 (89.4)	63.8 [126.4]
PMMA/5HA treated 2% Si	Flexural modulus [GPa]	2.7	2.6 (96.3)	2.9 [105.5]	2.7 (100.0)	3.0 [110.28]
	Flexural strength [MPa]	56.5	56.1 (99.3)	63.8 [120.8]	49.4 (93.2)	55.3 [97.9]
PMMA/5HA treated 4% Si	Flexural modulus [GPa]	2.8	2.7 (97.4)	2.9 [102.8]	2.7 (91.7)	3.0 [106.8]
	Flexural strength [MPa]	61.4	56.2 (91.5)	58.1 [102.8]	47.7 (84.3)	61.9 [109.4]
PMMA/5HA treated 6% Si	Flexural modulus [GPa]	2.9	2.7 (93.7)	2.9 [100.4]	2.7 (91.7)	3.0 [105.3]
	Flexural strength [MPa]	61.4	55.7 (90.8)	54.6 [89.0]	47.9 (71.3)	60.0 [97.9]
PMMA/5HA treated 8% Si	Flexural modulus [GPa]	2.8	2.7 (96.5)	2.9 [104.9]	2.8 (100.4)	3.1 [111.5]
	Flexural strength [MPa]	52.4	51.7 (98.6)	57.8 [110.4]	52.6 (100.4)	63.0 [120.3]

Remark 1: The values in parentheses () are the percentage retention of the flexural properties after water absorption and the values in brackets [] are the percentage recovery of the flexural properties after re-drying

Remark 2: Statistically analyzed with one-way ANOVA correspond to various immersion condition indicate significant different ($P < 0.05$) in flexural modulus ($R^2 = 0.732$) and flexural strength ($R^2 = 0.826$)

Table 2 shows that the flexural strength of PMMA composites was slightly increased after 1 month of water absorption. After 2 months of water absorption, flexural strength for all specimens was decreased in wet state. Table 2 also shows that the percentage of retention of the flexural strength of all PMMA/5HA composite was decreased after 2 months of water absorption. This is due to the plasticizing effect of water molecules which diffused into the matrix and filler. However, the flexural strength of treated PMMA/5HA composite could recover greatly by considering its properties after 2 months of water absorption in the re-dried state. The moisture diffused predominantly into the matrix resin, resulting in a significant mismatch of the moisture induced volumetric expansion between the matrix and the filler. When the stress exceeds the strength of the interphase region, debonding may take place between the filler and the matrix resulting in an irreversible damage to the dental composite [28]. The flexural strength of the PMMA/5HA composites decreased due to the weak interfacial bonding between PMMA and HA [29]. This will lead to increased micro voids in the composites, and, as a result, increase of water absorption [22]. When HA particles are embedded in the highly entangled polymer chains, there are micro-voids (or free volume voids) in the composite interface and even within the matrix polymer. These micro-spaces are essential for the relaxation of polymer chains and induce transportation of water molecules when soaking in an aqueous environment [25]. Accordingly, the water molecule can act as internal plasticizer. It is interesting to note that PMMA/8% γ -MPS treated 5HA composites still remain of the same strength as the control sample. This indicates that the HA treated with 8% γ -MPS can provide better hydrolytic stability without diminishing the flexural properties of the PMMA composites during water absorption.

3.3. Kinetics of SBF absorption

Figure 3 shows the effect of γ -MPS concentration on the moisture uptake of PMMA and PMMA/5HA composites during SBF absorption at 37°C up to 2 months of immersion. The initial linear region showed a faster rate of SBF uptake for PMMA/5HA composite followed by the PMMA/ γ -MPS treated 5HA composites and unfilled PMMA. All

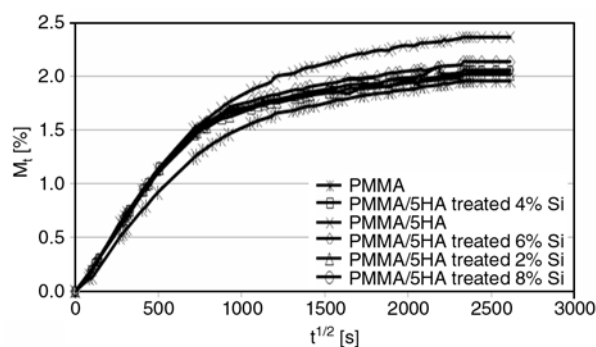


Figure 3. The effects of γ -MPS concentration on the SBF uptake of PMMA upon subjected to SBF absorption

specimens showed an SBF uptake process involving a rapid Fickian process which is linear to $t^{1/2}$ followed by a slower rate of uptake which is indicated as matrix saturation. The SBF and liquid uptake into polymer matrix is governed by either the free volume theory, in which water diffuses through substrates or the interaction theory, in which it is controlled solely by the available hydrogen bond at the polar sites [13]. The equilibrium of SBF absorption (M_m) was achieved after 2 months of immersion. From Table 1, it can be seen that the maximum SBF absorption (M_m) of PMMA and PMMA/5HA composites is approximately 1.96% and 2.36%, respectively. However, the SBF uptake of PMMA/ γ -MPS treated 5HA composite was decreased to 2.02–2.14% as a function of the concentration of γ -MPS. This suggests that a better bonding between the γ -MPS treated HA filler and the PMMA. According to Deb *et al.* [10], the silanization of the mineral phase probably inhibits water uptake due to hydrophobic surface.

Table 1 also shows the diffusion coefficients (D) of PMMA, PMMA/5HA composites and PMMA/ γ -MPS treated 5HA composites after SBF immersion at 37°C for 2 months. The diffusion coefficient (D) of PMMA/5HA composites ($D = 1.94 \cdot 10^{-12} \text{ m}^2/\text{s}$) is somewhat higher than that of PMMA ($D = 1.64 \cdot 10^{-12} \text{ m}^2/\text{s}$). According to Yiu *et al.* [13], the polarity and hydrophilic sites in the composite may lead to trapping sites to stop the water for interaction which will subsequently hinder the water molecule diffusion. It is interesting to note that the γ -MPS treated PMMA/5HA composites (6% γ -MPS and 8% γ -MPS) are slightly lower than untreated PMMA/5HA composite. This is again attributed to the better interfacial between PMMA and HA, which in turn, reduces the transportation path of the

water molecules in the PMMA matrix. According to Drummond [11], the bonding of glass to resin through silane agents (formation of oxane bonds) other than simple chemical reactivity is good in explained by interdiffusion and interpolymer network formation in the interphase region. According to Karabela and Sideridou [17], as the dental composites are placed in the oral environment absorption of water takes place, which may lead to the degradation of the silane coupling agent and reinforcing filler. The debonded interphase is the fastest path for water migration into the interior layer of resin composite. With the unsilanized composite, degradation is the most severe resulting in the deepest degradation depth. However, as the fillers are silanized, the silane film absorbing water before undergoing hydrolysis resists water diffusion into composite. The diffusion coefficients of untreated and treated PMMA/5HA composite are generally higher than that of PMMA. This may be due to the ions in the SBF, i.e. Na⁺, K⁺, Ca²⁺, Cl⁻ and HCO₃⁻. The presence of these ions may leads to the formation of apatite on the HA particles (which are distributed on the surface of the sample) and thus these ion concentrations, especially that of HCO₃⁻ induce increased rate of diffusivity in the sample by interacting with the hydroxyl groups of the specimen. According to Greish and Brown [30], the mechanism of apatite on the surfaces of bioactive glasses, such as calcium, phosphate, and silicate ions are released from the bioactive glass

surfaces, leaving a hydrated silica layer. This layer has been reported to enhance the formation of the apatite nuclei. The dissolution of calcium and phosphate ions increases the the activity of the ionic components of apatite in the surrounding fluid, leading to the precipitation of the apatite nuclei on the hydrated silica layer, which later grow spontaneously. Verestiuc *et al.* [31] reported that for shorter interaction time of SBF with the substrate, the concentration of Ca²⁺ ion and (PO₄)³⁻ increases. After few days, the Ca²⁺ ion and (PO₄)³⁻ variations evolve oppositely due to the diffusion of positive and negative ions having different motilities in SBF. This implies a continuous change of the quality of the chemical growth of calcium phosphates layers on substrates.

3.4. Effects of SBF absorption on the flexural properties of PMMA composites

Table 3 shows the flexural modulus and strength of PMMA and its composites after being subjected to SBF absorption for 1 and 2 months. Table 3 also shows the flexural properties (with their percentage of retention and percentage of recovery) of PMMA and its composites in wet and re-dried states after being subjected to SBF absorption. It can be seen that the flexural modulus and strength in wet states of PMMA/γ-MPS treated 5HA composites was decreased after being subjected to SBF test for 1 month. The reduction of the flexural properties of

Table 3. Flexural properties of PMMA, PMMA/5HA composites and PMMA/γ-MPS treated 5HA composites in wet and redried states after being subjected to SBF tests for various condition (*n* = 3)

Material	Flexural properties	Control	Duration of immersion			
			1 month		2 months	
			Wet	Redried	Wet	Redried
PMMA	Flexural modulus [GPa]	2.3	2.4 (103.6)	2.7 [117.1]	2.4 (105.0)	2.5 [110.8]
	Flexural strength [MPa]	77.7	82.9 (106.7)	90.9 [117.0]	80.8 (103.9)	88.1 [113.4]
PMMA/5HA	Flexural modulus [GPa]	2.5	2.4 (95.9)	2.7 [107.4]	2.5 (98.5)	2.5 [99.3]
	Flexural strength [MPa]	50.5	57.9 (114.8)	73.0 [144.6]	64.0 (126.8)	62.7 [124.2]
PMMA/5HA treated 2% Si	Flexural modulus [GPa]	2.7	2.2 (82.4)	2.5 [89.8]	2.4 (88.3)	2.8 [104.1]
	Flexural strength [MPa]	56.5	42.7 (80.6)	53.9 [102.2]	44.1 (83.6)	57.2 [107.7]
PMMA/5HA treated 4% Si	Flexural modulus [GPa]	2.8	2.3 (82.2)	2.6 [93.6]	2.6 (93.1)	2.6 [95.1]
	Flexural strength [MPa]	61.4	47.8 (84.5)	52.5 [92.8]	50.3 (89.0)	54.0 [95.5]
PMMA/5HA treated 6% Si	Flexural modulus [GPa]	2.9	2.3 (79.9)	2.7 [93.8]	2.6 (89.4)	2.9 [99.3]
	Flexural strength [MPa]	61.4	43.0 (70.0)	54.8 [89.6]	45.8 (74.6)	53.7 [87.6]
PMMA/5HA treated 8% Si	Flexural modulus [GPa]	2.8	2.4 (86.3)	2.6 [94.1]	2.6 (92.5)	2.9 [102.4]
	Flexural strength [MPa]	52.4	46.7 (89.2)	56.5 [107.9]	45.8 (87.4)	59.3 [113.2]

Remark 1: The values in parentheses () are the percentage retention of the flexural properties after SBF absorption and the values in brackets [] are the percentage recovery of the flexural properties after re-drying

Remark 2: Statistically analyzed with one-way ANOVA correspond to various immersion condition indicate significant different (*P* < 0.05) in flexural modulus (*R*² = 0.826). However, the flexural strength (*R*² = 0.925) correspond to various immersion condition indicate no significant different (*P* > 0.05).

these composites is due to the fact that the moisture contents may plasticize the composites, and thus weaken the bonding between HA filler and PMMA matrix due to the volumetric expansion within both phases. According to Sabbagh *et al.* [32], water molecules can lead to plasticizing effect in the matrix and cause degradation of the filler-matrix interface. The slightly reduction of the PMMA/ γ -MPS treated 5HA composites could be due to the undesirable and excessive loading of silane coupling agent. It is believed that the excess concentration of silane coupling agent (i.e. free and unreacted γ -MPS which located at the interface between the PMMA and HA) could contact with water molecule through hydrolytic reaction, and further cause the debonding of filler and matrix. In addition, the ion and water molecules in SBF can be accommodated at the interface between the filler and matrix

through a weak link. This weak link could provide paths of facile water molecule diffusion. According to Reis *et al.* [27], the increase and/or no significant change of flexural properties in denture base acrylic resin could be partially explained by continuous polymerization of the polymers. Residual monomer acts as plasticizer which by leaching out from the specimens could contribute to the increase in flexural properties after water immersion. On the contrary, water molecules absorbed during immersion may influence the mechanical properties of denture base acrylic resins by the plasticizing effect. Table 3 shows that the flexural properties of the redried-PMMA/HA composites are higher than that of the wet-PMMA/HA composites after SBF tests. According to Cattani-Lorente *et al.* [33], water has two approach effects on resin-modified glass ionomer cement: (1) water acts can as a plasticizer

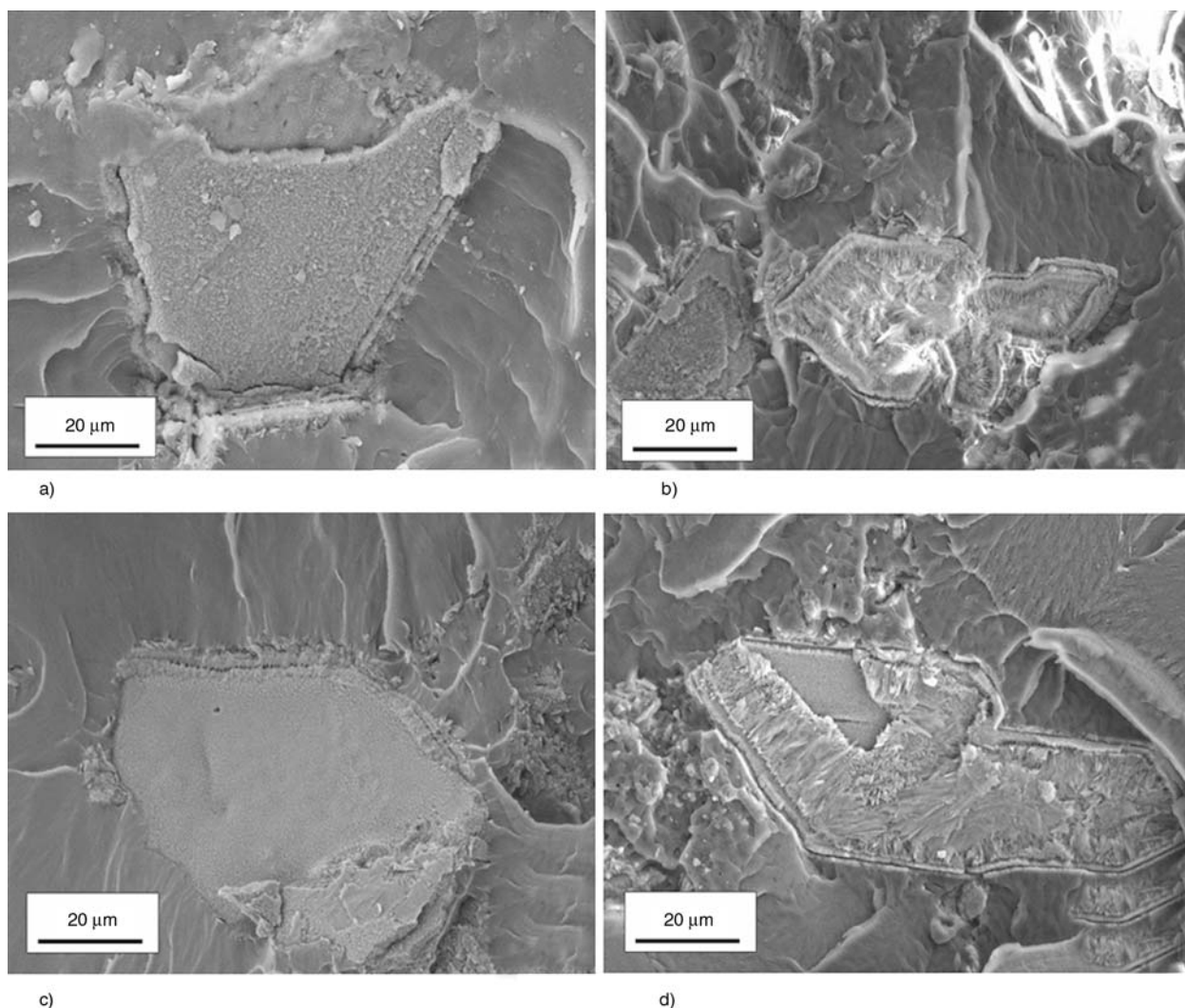


Figure 4. FESEM micrographs taken from the fractured surfaces of (a) PMMA/5HA-control, (b) PMMA/5HA composites after being subjected to water absorption, (c) PMMA/ γ -MPS treated HA-control, and (d) PMMA/ γ -MPS treated HA composites after being subjected to water absorption

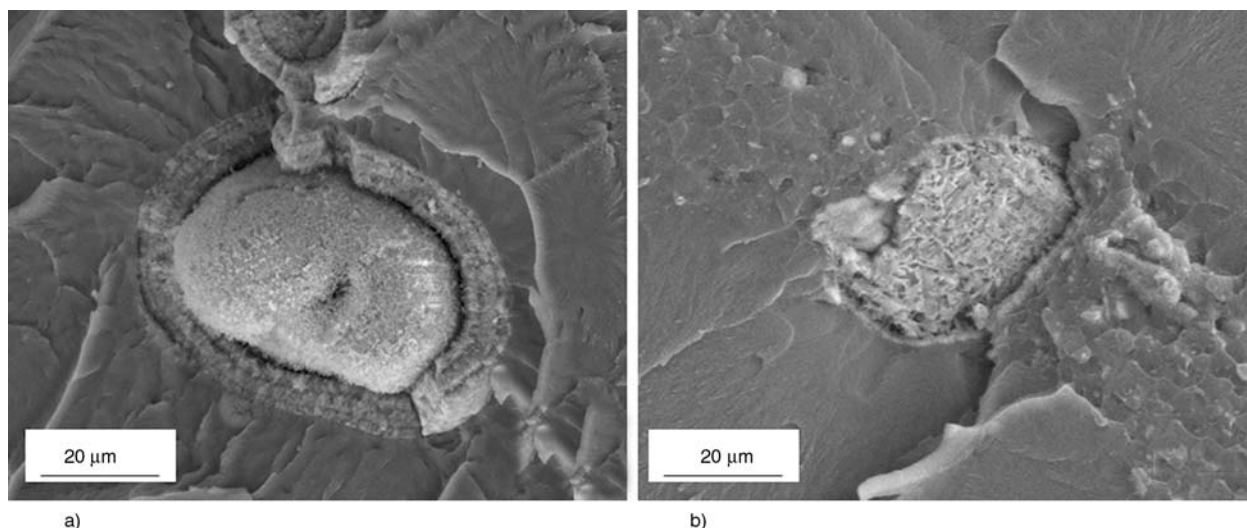


Figure 5. FESEM micrographs taken from the fractured surfaces of (a) PMMA/5HA composites and (b) PMMA/ γ -MPS treated HA composites after being subjected to SBF immersion

and reduce the flexural strength. However, when excess water is removed, flexural strength of the samples almost reverted to initial values; (2) water also partly dissolved the components of the cement, changing the network structure, resulting in a slight but irreversible decrease of their strength. In addition, the presence of salts and proteins in the saliva will minimize the effect of water on the dental restorations.

3.5. Morphological properties

Figure 4 shows the FESEM micrographs taken from the fractured surfaces of PMMA/5HA and PMMA/ γ -MPS treated HA composites in their control state and after being subjected to water absorption. It can be seen that there is noticeable gap between PMMA and HA for the untreated PMMA/5HA composite (c.f. Figure 4a), however, for the PMMA/ γ -MPS treated HA composites, there is a better interfacial interaction between PMMA and HA (c.f. Figure 4c). From Figure 4b and 4d, it can be seen that the fracture morphology of the PMMA/HA and PMMA/ γ -MPS treated HA composites did not change much. This fracture morphology can support the excellent recovery and retention properties of PMMA composites after being subjected to water absorption. Figure 5 shows the FESEM micrographs taken from the fractured surfaces of

PMMA/5HA composites and PMMA/ γ -MPS treated 5HA composites after being subjected to SBF immersion. Little de-bonding of the interfacial interaction between PMMA/5HA composites (with and without coupling agent) can be observed from the fractured surface. This may be related to the ions and water molecules in SBF that can be accommodated at the interface between the filler and matrix as a weak link.

4. Conclusions

The kinetics of water absorption and SBF absorption of PMMA/HA composites conformed to the Fickian Law behavior. It was found that the γ -MPS treated HA could help to reduce the water uptake due to the ability of γ -MPS to react with hydroxyl groups in the HA filler by introducing a hydrophobic layer on HA particles surface. The diffusion coefficient of PMMA/5HA composite (untreated and treated) is lower than that of PMMA. This is due to the present of HA particles which could restrict the diffusivity of water. The excellent retention and recovery of the PMMA/HA composites on mechanical properties could be attributed to the enhanced interfacial interaction between HA filler and PMMA matrix by the treatment of γ -MPS in water absorption.

Acknowledgements

The authors would like to thank MOSTI Malaysia for the Science Fund research grant, Universiti Sains Malaysia for the Research University Grant, Research University Post-graduate Research Grant Scheme and USM Fellowship. The authors would like to express their appreciation to Dr Sivakumar A/L Ramakrishnan (Universiti Sains Malaysia) for providing the technical knowledge in statistical analysis.

References

- [1] Chen T., Kusy R. P.: Effect of methacrylic acid: Methyl methacrylate monomer ratios on polymerization rates and properties of polymethyl methacrylates. *Journal of Biomaterials Materials Research Part A*, **36**, 190–199 (1997).
DOI: [10.1002/\(SICI\)1097-4636\(199708\)36:2<190::AID-JBM7>3.0.CO;2-F](https://doi.org/10.1002/(SICI)1097-4636(199708)36:2<190::AID-JBM7>3.0.CO;2-F)
- [2] John J., Gangadhar S. A., Shah I.: Flexural strength of heat-polymerized polymethyl methacrylate denture resin reinforced with glass, aramid, or nylon fibers. *The Journal of Prosthetic Dentistry*, **86**, 424–427 (2001).
DOI: [10.1067/mpr.2001.118564](https://doi.org/10.1067/mpr.2001.118564)
- [3] Uzun G., Hersek N., Tinçer T.: Effect of five woven fiber reinforcements on the impact and transverse strength of a denture base resin. *The Journal of Prosthetic Dentistry*, **81**, 616–620 (1999).
DOI: [10.1016/S0022-3913\(99\)70218-0](https://doi.org/10.1016/S0022-3913(99)70218-0)
- [4] Kim S-H., Watts D. C.: The effect of reinforcement with woven E-glass fibers on the impact strength of complete dentures fabricated with high-impact acrylic resin. *The Journal of Prosthetic Dentistry*, **91**, 274–280 (2004).
DOI: [10.1016/j.prosdent.2003.12.023](https://doi.org/10.1016/j.prosdent.2003.12.023)
- [5] Jagger D. C., Harrison A., Jandt K. D.: The reinforcement of dentures. *Journal of Oral Rehabilitation*, **26**, 185–194 (1999).
DOI: [10.1046/j.1365-2842.1999.00375.x](https://doi.org/10.1046/j.1365-2842.1999.00375.x)
- [6] Hu Q. L., Li B. Q., Wang M., Shen J. C.: Preparation and characterization of biodegradable chitosan/hydroxyapatite nanocomposite rods via in situ hybridization: A potential material as internal fixation of bone fracture. *Biomaterials*, **25**, 779–785 (2004).
DOI: [10.1016/S0142-9612\(03\)00582-9](https://doi.org/10.1016/S0142-9612(03)00582-9)
- [7] Morita S., Furuya K., Ishihara K., Nakabayashi N.: Performance of adhesive bone cement containing hydroxyapatite particles. *Biomaterials*, **19**, 1601–1606 (1998).
DOI: [10.1016/S0142-9612\(97\)00120-8](https://doi.org/10.1016/S0142-9612(97)00120-8)
- [8] Reeson M. G., Jepson N. J. A.: Achieving an even thickness in heat-polymerized permanent acrylic resin denture bases for complete dentures. *The Journal of Prosthetic Dentistry*, **82**, 359–361 (1999).
DOI: [10.1016/S0022-3913\(99\)70094-6](https://doi.org/10.1016/S0022-3913(99)70094-6)
- [9] Oysad H., Ruyter I. E.: Water sorption and filler characteristics of composites for use in posterior teeth. *Journal of Dental Research*, **65**, 1315–1318 (1986).
DOI: [10.1177/00220345860650110601](https://doi.org/10.1177/00220345860650110601)
- [10] Deb S., Braden M., Bonfield W.: Water absorption characteristics of modified hydroxyapatite bone cements. *Biomaterials*, **16**, 1095–1100 (1995).
DOI: [10.1016/0142-9612\(95\)98906-U](https://doi.org/10.1016/0142-9612(95)98906-U)
- [11] Drummond J. L.: Degradation, fatigue, and failure of resin dental composite materials. *Journal of Dental Research*, **87**, 710–719 (2008).
DOI: [10.1177/154405910808700802](https://doi.org/10.1177/154405910808700802)
- [12] Dhanpal P., Yiu C. K. Y., King N. M., Tay F. R., Hirashi N.: Effect of temperature on water sorption and solubility of dental adhesive resins. *Journal of Dentistry*, **37**, 122–132 (2009).
DOI: [10.1016/j.jdent.2008.10.004](https://doi.org/10.1016/j.jdent.2008.10.004)
- [13] Yiu C. K. Y., King N. M., Carrilho M. R. O., Sauro S., Ruggenberg F. A., Prati C., Carvalho R. M., Pashley D. H., Tay F. R.: Effect of resin hydrophilicity and temperature on water sorption of dental adhesive resin. *Biomaterials*, **27**, 1695–1703 (2006).
DOI: [10.1016/j.biomaterials.2005.09.037](https://doi.org/10.1016/j.biomaterials.2005.09.037)
- [14] Andrade Â. L., Turchetti-Maia R. M. M., Lopes M. T. P., Salas C. E., Domingues R. Z.: *In vitro* bioactivity and cytotoxicity of chemically treated glass fibers. *Materials Research*, **7**, 635–638 (2004).
DOI: [10.1590/S1516-14392004000400019](https://doi.org/10.1590/S1516-14392004000400019)
- [15] Palin W. M., Felming G. J. P., Burke F. J. T., Marquis P. M., Randall R. C.: The influence of short and medium-term water immersion on the hydrolytic stability of novel low-shrink dental composites. *Dental Materials*, **21**, 852–863 (2005).
DOI: [10.1016/j.dental.2005.01.004](https://doi.org/10.1016/j.dental.2005.01.004)
- [16] Asaoka K., Hirano S.: Diffusion coefficient of water through dental composite resin. *Biomaterials*, **24**, 975–979 (2003).
DOI: [10.1016/S0142-9612\(02\)00435-0](https://doi.org/10.1016/S0142-9612(02)00435-0)
- [17] Karabela M. M., Sideridou I. D.: Effect of the structure of silane coupling agent on sorption characteristics of solvents by dental resin-nanocomposites. *Dental Materials*, **24**, 1631–1639 (2008).
DOI: [10.1016/j.dental.2008.02.021](https://doi.org/10.1016/j.dental.2008.02.021)
- [18] Liu Q., Ding J., Chambers D. E., Debnath S., Wunder S. L., Baran G. R.: Filler-coupling agent-matrix interactions in silica/polymethylmethacrylate composites. *Journal of Biomedical Materials Research Part A*, **57**, 384–393 (2001).
DOI: [10.1002/1097-4636\(20011205\)57:3<384::AID-JBM1181>3.0.CO;2-F](https://doi.org/10.1002/1097-4636(20011205)57:3<384::AID-JBM1181>3.0.CO;2-F)
- [19] Söderholm K-J. M., Shang S-W.: Molecular orientation of silane at the surface of colloidal silica. *Journal of Dental Research*, **72**, 1050–1054 (1993).
DOI: [10.1177/00220345930720061001](https://doi.org/10.1177/00220345930720061001)

- [20] Beatty M. W., Swartz M. L., Moore B. K., Philips R. W., Roberts T. A.: Effect of microfiller fraction and silane treatment on resin composite properties. *Journal of Biomedical Materials Research Part A*, **40**, 12–23 (1998).
DOI: [10.1002/\(SICI\)1097-4636\(199804\)40:1<12::AID-JBM2>3.0.CO;2-U](https://doi.org/10.1002/(SICI)1097-4636(199804)40:1<12::AID-JBM2>3.0.CO;2-U)
- [21] Harper E. J., Braden M., Bonfield W.: Mechanical properties of hydroxyapatite reinforced poly(ethylmethacrylate) bone cement after immersion in a physiological solution: Influence of a silane coupling agent. *Journal of Materials Science: Materials in Medicine*, **11**, 491–497 (2000).
DOI: [10.1023/A:1013057724268](https://doi.org/10.1023/A:1013057724268)
- [22] Yang H-S., Kim H-J., Park H-J., Lee B-J., Hwang T-S.: Water absorption behavior and mechanical properties of lignocellulosic filler-polyolefin bio-composites. *Composites Structures*, **72**, 429–437 (2006).
DOI: [10.1016/j.compstruct.2005.01.013](https://doi.org/10.1016/j.compstruct.2005.01.013)
- [23] Santos C., Luklinska Z. B., Clarke R. L., Davy K. W. M.: Hydroxyapatite as a filler for dental composite materials: Mechanical properties and in vitro bioactivity of composites. *Journal of Materials: Materials in Science*, **12**, 565–573 (2001).
DOI: [10.1023/A:1011291723503](https://doi.org/10.1023/A:1011291723503)
- [24] Unemori M., Matsuya Y., Matsuya S., Akashi A., Akamie A.: Water absorption of poly(methyl methacrylate) containing 4-methacryloxyethyl trimellitic anhydride. *Biomaterials*, **24**, 1381–1387 (2003).
DOI: [10.1016/S0142-9612\(02\)00521-5](https://doi.org/10.1016/S0142-9612(02)00521-5)
- [25] Tang Y. C., Chen D. Z., Yue T. M., Chan K. C., Tsui C. P., Peter Yu H. F.: Water absorption and solubility of PHBV/HA nanocomposites. *Composites Science and Technology*, **68**, 1927–1934 (2008).
DOI: [10.1016/j.compscitech.2007.12.003](https://doi.org/10.1016/j.compscitech.2007.12.003)
- [26] Matinlinna J. P., Vallittu P. K.: Silane based concepts on bonding resin composite to metals. *The Journal of Contemporary Dental Practice*, **8**, 1–8 (2007).
- [27] Reis J. M. S. N., Vergani C. E., Pavarina A. C., Giampaolo E. T., Machado A. L.: Effect of relining, water storage and cyclic loading on the flexural strength of a denture base acrylic resin. *Journal of Dentistry*, **34**, 420–426 (2006).
DOI: [10.1016/j.jdent.2005.10.001](https://doi.org/10.1016/j.jdent.2005.10.001)
- [28] Fan J. P., Tsui C. P., Tang C. Y., Chow C. L.: 3D finite element analysis of the damage effects on the dental composite subject to water sorption. *Acta Mechanica Solida Sinica*, **19**, 212–222 (2006).
DOI: [10.1007/s10338-006-0626-4](https://doi.org/10.1007/s10338-006-0626-4)
- [29] Sousa R. A., Reis R. L., Cunha A. M., Bevis M. J.: Coupling of HDPE/hydroxyapatite composites by silane-based methodologies. *Journal of Materials Science: Materials in Medicine*, **14**, 475–487 (2003).
DOI: [10.1023/A:1023471011749](https://doi.org/10.1023/A:1023471011749)
- [30] Greish Y. E., Brown P. W.: Characterization of bioactive glass-reinforced HAp-polymer composites. *Journal of Biomedical Materials Research Part A*, **52**, 687–694 (2000).
DOI: [10.1002/1097-4636\(20001215\)52:4<687::AID-JBM13>3.0.CO;2-K](https://doi.org/10.1002/1097-4636(20001215)52:4<687::AID-JBM13>3.0.CO;2-K)
- [31] Verestiuc L., Morosanu C., Bercu M., Pasuk I., Mihailescu I. N.: Chemical growth of calcium phosphate layers on magnetron sputtered HA films. *Journal of Crystal Growth*, **264**, 483–491 (2004).
DOI: [10.1016/j.jcrysgro.2004.01.015](https://doi.org/10.1016/j.jcrysgro.2004.01.015)
- [32] Sabbagh J., Vreven J., Leloup G.: Dynamic and static moduli of elasticity of resin-based materials. *Dental Materials*, **18**, 64–71 (2002).
DOI: [10.1016/S0109-5641\(01\)00021-5](https://doi.org/10.1016/S0109-5641(01)00021-5)
- [33] Cattani-Lorente M. A., Dupuis V., Payan J., Moya F., Meyer J-M.: Effect of water on the physical properties of resin-modified glass ionomer cement. *Dental Materials*, **15**, 71–78 (1999).
DOI: [10.1016/S0109-5641\(99\)00016-0](https://doi.org/10.1016/S0109-5641(99)00016-0)

Reinforcement of nitrile rubber by *in situ* formed zinc disorbate

B. C. Guo^{1,2*}, F. Chen¹, W. W. Chen¹, Y. D. Lei¹, D. M. Jia¹

¹Department of Polymer Materials and Engineering, South China University of Technology, Guangzhou 510640, China

²State Key Laboratory of Pulp and Paper Engineering, South China University of Technology, Guangzhou 510640, China

Received 2 April 2010; accepted in revised form 16 May 2010

Abstract. Zinc disorbate (ZDS) was *in situ* formed by the reaction between sorbic acid (SA) and zinc oxide (ZnO) in nitrile rubber (NBR). The effects of SA amount on the curing characteristics, crosslink density and mechanical properties of peroxide-cured NBR were studied. The results showed that ZDS was generated mainly during the rubber vulcanization, rather than the open mill compounding phase. The results from the crosslink density determinations showed that the formation of ZDS significantly increased the ionic bond content in the vulcanizates. In addition, the formation of ZDS greatly enhanced the mechanical properties of NBR vulcanizates. The modulus, tensile strength, tear strength and hardness were found to be increased with the loading of ZDS. Preheating the compounds before compression moulding was beneficial to the formation of ZDS, and consequently the increases in mechanical properties. At 40 parts per hundred rubber (phr) of SA and 16 phr ZnO, five to six folds of tensile strength and tear strength of the neat NBR vulcanizate were achieved. Transmission electron microscopy (TEM) results confirmed the nano-dispersion structure of the polymerized ZDS in the NBR matrix.

Keywords: reinforcements, nitrile rubber, sorbic acid, zinc oxide

1. Introduction

Carbon black, silica and clay have already been used as effective reinforcements of rubbers for different purposes [1–4]. Ionic clusters have also been proved to be reinforcing towards rubbers [5, 6]. Since highly filled zinc dimethacrylate (ZDMA) reinforced hydrogenated nitrile rubber (HNBR) with high tensile and excellent abrasion resistance was developed by Zeon Chemicals, reactive metal carboxylates have been tried as novel rubber reinforcements for their good dispersion properties and reinforcing effect [7–18]. Zhang and coworkers [11–14] investigated the *in situ* formation of ZDMA and magnesium dimethacrylate (MDMA) by the reaction of zinc oxide (ZnO), magnesium oxide (MgO) with methacrylic acid (MAA), and discussed the reinforcing effect of the resultants on the rubbers. Lu *et al.* [16] investigated the morpholo-

gies of ZDMA particles in various elastomers before and after vulcanization by scanning electron microscopy (SEM) and transmission electron microscopy (TEM). During compounding, the size of ZDMA particle was reduced and could even form nano-scale structures, depending on the shear stress during mixing. The authors observed two structures in the vulcanizates: a micron-scale dispersion of residual ZDMA particles and a nano-scale dispersion of poly-ZDMA aggregates. Multiple mechanisms for the reinforcement of rubbers by reactive metal carboxylates were involved in the systems [11, 14, 17]. First, during the rubber vulcanization, the unsaturated metal carboxylates could be polymerized (crosslinking) to form the reinforcing nanoparticles via free radical mechanism. Furthermore, the unsaturated salts could be grafted onto rubber chains during rubber vulcaniza-

*Corresponding author, e-mail: psbcguo@scut.edu.cn
© BME-PT

tion. Therefore reinforced rubber network with very tight interfacial bonding was formed in these systems. As a consequence, the mechanical properties of these rubber compounds were extraordinarily higher than those filled with traditional fillers such as carbon black or silica.

In view of the high cost of metal (meth)acrylates and the corrosive nature of (meth)acrylic acid, exploring alternative reactive metal carboxylates was still necessary. Recently, we demonstrated that sorbic acid (SA), a common food preservative, was very effective in promoting the interfacial properties of silica or halloysite reinforced rubber and it is revealed that zinc disorbate (ZDS) was *in situ* formed in those systems [19–21]. In the present work, we attempted to use the *in situ* formed ZDS as the sole reinforcing agent for nitrile rubber (NBR). The formation regularity of ZDS, curing characteristics and reinforceability of the formed ZDS, were investigated.

2. Experimental

2.1. Materials

NBR with acrylonitrile content 40%, was manufactured by Jilin Chemical Industry Company, Jilin, China. SA with purity of 98% was obtained from Ningbo Wanglong Group Co., Ltd, Zhejiang, China. ZnO was analytical grade from Tianjin Fuchen Chemical Reagent Co., Ltd, Tianjin, China. Stearic acid was chemical grade from Shanghai Lingfeng Chemical Reagent Co., Ltd, Shanghai, China. 2-mercaptobenzimidazole (MB) was chemical grade from Guangzhou Chuangsheng Chemical Material Co., Ltd, Guangdong, China. Dicumyl peroxide (DCP) was chemical grade from Sinopharm Chemical Reagent Co., Ltd, Shanghai, China. Acetone was analytic grade from Guangzhou Dongfanghong Chemical Plant, Guangdong, China.

2.2. Preparation of NBR/ ZDS composites

The compositions of the rubber compounds were tabulated in Table 1. The molar ratio of ZnO/SA was kept at 1/1.8 in all samples except for the control sample. ZnO was slightly excessive as stearic acid will react with zinc oxide to form zinc stearate. NBR and SA were compounded with rubber additives with a two-roll mill at room temperature. For comparison, a group of the compounds excluding

Table 1. Compositions of NBR/ZDS nanocomposites^a

Sample code	1	2	3	4	5	6
NBR	100	100	100	100	100	100
Stearic acid	1	1	1	1	1	1
MB	1.5	1.5	1.61	1.76	1.9	2.05
ZnO	1	1	4	8	12	16
SA	0	2.5	10	20	30	40
DCP	1	1	1.07	1.17	1.27	1.37

^a NBR: nitrile rubber; ZnO: zinc oxide; MB: 2-mercaptobenzimidazole; SA: sorbic acid; DCP: dicumyl peroxide

DCP were placed in an oven at 120°C, and then evacuated to eliminate possible oxidation of the compounds. All the compounds were heat treated for 15 min in the vacuum oven before vulcanization. DCP was then included into the heat treated samples by re-compounding the samples. Then all the compounds were press-cured to a 1 mm thickness sheet at 170°C vulcanization time and then cut into specimens for measurements. The vulcanization time was determined at 170°C by U-CAN UR-2030 vulcameter, Taipei, Taiwan.

3. Characterizations

3.1. Differential scanning calorimetry (DSC)

To explore the reaction between ZnO and SA during simple heating, the mixture of ZnO/SA (molar ratio of 1/2) was prepared by vigorous mixing. The reaction of the mixture under heating was studied by DSC. The mixture was sealed in DSC pan and the heat flow during heating was recorded. The heat flow of the sample was shown in Figure 1, which indicated that there were several stages for the reaction between ZnO and SA. We chose three upper temperatures at 60, 90 and 120°C for preparing three treated samples at different degrees of con-

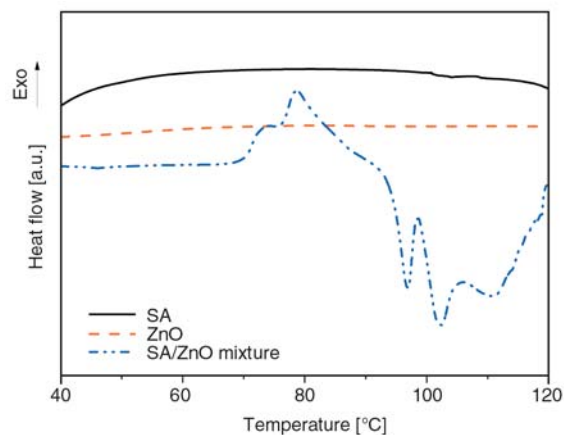


Figure 1. DSC graph of the SA, ZnO, and SA/ZnO mixture

version. When the temperature was heated to the upper temperature, the sample was quenched to stop the reaction. The three samples with upper treating temperatures at 60, 90 and 120°C were labeled as A, B and C, respectively. All the DSC runs were conducted with a TA Q20 (New Castle, America) at a ramping rate of 2°C/min and using nitrogen as purging gas.

3.2. X-ray diffraction (XRD)

The XRD of the rubber compounds, vulcanizates and the above mentioned samples of A, B and C were recorded at ambient temperature on a Rigaku Dmax/III diffractometer (Rigaku Corporation, Tokyo, Japan) using a $\text{CuK}\alpha$ radiation ($\lambda = 1.54 \text{ \AA}$). All the samples were scanned from 2 to 50° with a step length of 0.02°.

3.3. Determination of crosslink density

Crosslink density was determined by the equilibrium swelling method [10, 11, 17, 22, 23]. The value was classified into three types, that is, covalent crosslink density (V_{e1}), ionic crosslink density (V_{e2}) and total crosslink density ($V_e = V_{e1} + V_{e2}$). To measure V_e , samples were swollen in acetone ($\rho_s = 0.788 \text{ g/ml}$) at room temperature for 72 h and then removed from the solvent and the surface acetone was blotted off quickly with tissue paper. The samples were immediately weighed on an analytical balance and then dried in a vacuum oven for 36 h at 70°C to remove all the solvent and reweighed. The volume fraction of NBR in the swollen gel, V_r , was calculated by Equation (1) [22]:

$$V_r = \frac{m_0 \phi \frac{1-\alpha}{\rho_r}}{m_0 \phi \frac{1-\alpha}{\rho_r} + \frac{m_1 - m_2}{\rho_s}} \quad (1)$$

where m_0 is the sample mass before swelling, m_1 and m_2 are sample masses before and after drying, ϕ is the mass fraction of rubber in the vulcanizate, α is the mass loss of the gum NBR vulcanizate during swelling, and ρ_r and ρ_s are the rubber and solvent density, respectively.

The elastically active network chain density, V_e , which was used to represent the whole crosslink

density, was then calculated by the well-known Flory-Rehner equation (Equation (2)) [23]:

$$V_e = \frac{\ln(1-V_r) + V_r + \chi V_r^2}{V_s \left(\frac{1}{V_r^3} - \frac{V_r}{2} \right)} \quad (2)$$

where V_r is the volume fraction of the polymer in the vulcanizate swollen to equilibrium and V_s is the solvent molar volume (73.4 ml/mol for acetone at room temperature). χ is the NBR-acetone interaction parameter and is taken as 0.349 calculated according to reference [24, 25].

As mentioned above, the vulcanizates contained both covalent and ionic crosslinks, so it was significant to distinguish ionic crosslink density from covalent crosslink density. It was documented that rubber swollen in an acidic solution can destroy the ionic crosslinks [10, 11, 17]. To determine covalent crosslink density, samples were swollen again in the mixture of acetone and dichloroacetic acid for 120 h to destroy ionic crosslinks, then swollen in pure acetone for 72 h and weighed, and then vacuum dried and reweighed. V_{r1} calculated by Equation (1) represents the extent of swelling after destroying ionic crosslinks. V_{e1} calculated by Equation (2) represented the covalent crosslink density. V_{e2} calculated by subtracting V_{e1} from V_e .

3.4. Morphological observations

The specimens were ultramicrotomed into thin pieces of about 120 nm thickness with a Leica EM UC6 (Wetzlar, Germany). Then the TEM observations were done using a Philips Tecnai 12 TEM (Amsterdam, Netherlands) at an accelerating voltage of 30 kV.

3.5. Mechanical properties

Tensile tests including 100% modulus, tensile strength, elongation at break and permanent set were performed following ASTM D412 using U-CAN UT-2060 (Taipei, Taiwan) instrument, and the cross head speed was 500 mm/min. Shore A hardness was performed following DIN 53505 using a XY sclerometer (Shanghai, China).

4. Results and discussion

4.1. Formation of ZDS during rubber vulcanization

The DSC graph of ZnO, SA and the model ZnO/SA mixture is shown in Figure 1. It is clear that for ZnO and SA, there is no exothermic or endothermic peak appears during the process, indicating there is no reaction or phase change occurring in them in the tested temperature range. For the model ZnO/SA mixture, however, there is an exothermic peak around 80°C and endothermic peaks between 90 and 120°C. The exothermic peak and the endothermic regions indicate a complicated reaction process between ZnO and SA takes place during simple heating of the mixture. The XRD patterns of ZnO, SA and the model samples with different upper heat treating temperature were recorded. One can see in Figure 3 the characteristic diffraction peaks of SA at 13.5, 15.1, 26.9, 28.9 and 31.8° and the characteristic diffraction peaks of ZnO at 37.1, 39.8 and 41.6°. For sample A, the XRD pattern is the overlay of XRD patterns for ZnO and SA, suggesting that no reaction takes place between ZnO and SA below 60°C. For sample B, although the diffractions for SA are still present, the diffraction peaks of ZnO disappear. In addition, a new peak appears around 7.8°, which is, however, not identical to the diffraction of ZDS which evolved from basic zinc carbonate and SA [19]. In the XRD pattern of sample C, it can be seen that the diffractions for SA and ZnO completely disappear. New diffraction peak is observed at 6.8°, being close to that of ZDS, indicating the complete formation of ZDS. According to the report of Dolgoplosk *et al.* [26], a basic salt is first formed by the reaction of SA and ZnO. Then, the neutral salt is formed when the SA is excess. These two reactions could be described by Figure 2.

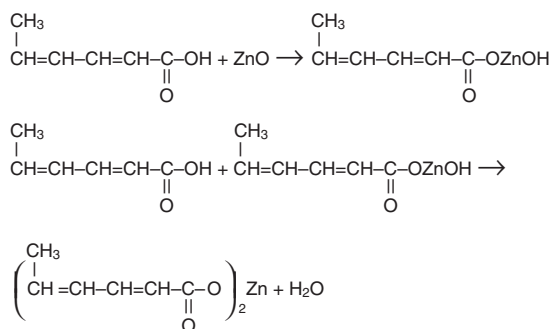


Figure 2. Reaction of SA and ZnO

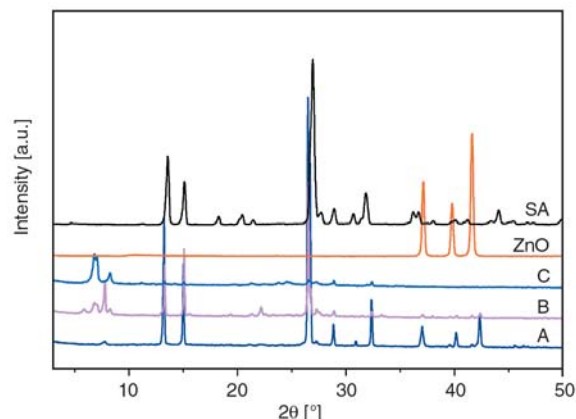


Figure 3. XRD patterns of SA, ZnO and the three samples A, B, C

It can be concluded that below 90°C, only intermediate product showing a diffraction peak around 7.8° is formed, and further heating to 120°C is necessary to obtain the ZDS completely. As a consequence, in the section below, we treated the rubber compounds at 120°C before the compression moulding and the results were compared with those without heat treatment.

The formation of ZDS during rubber vulcanization has been confirmed in our previous paper [19]. The same result was achieved in the present system. Figure 4 represents the XRD patterns of uncured rubber compounds with varying SA contents. It is shown that the intensities of the peaks at 22.76 and 27.66°, characterizing SA crystal, and the (100) and (101) diffractions of ZnO at 31.6 and 36.1° are consistently increased with SA and ZnO loading. Except for these observations, there are no other changes in Figure 4, and the diffraction of ZDS is not observed, indicating that almost no ZDS is formed during the open mill compounding. How-

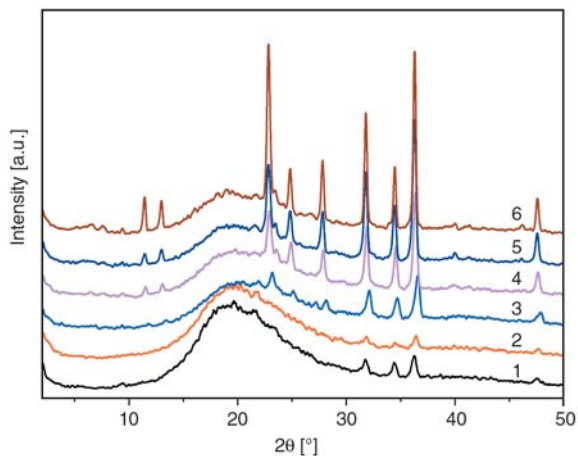


Figure 4. XRD patterns of uncured rubber compounds

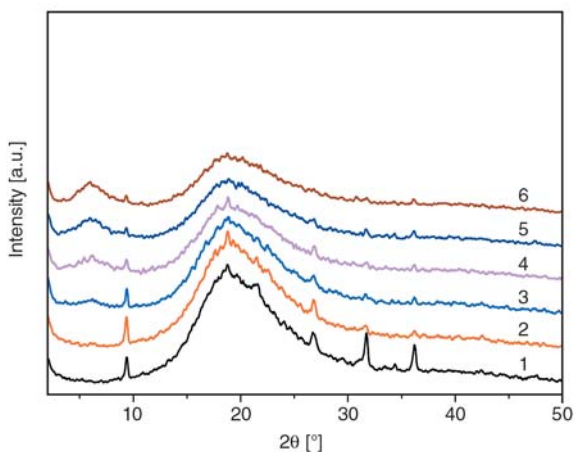


Figure 5. XRD patterns of rubber vulcanizates

ever, the reaction between SA and ZnO may take place during the vulcanization. As shown in Figure 5, which represents the XRD patterns of vulcanizates, the diffractions of SA and ZnO disappeared except for the control sample without SA. The reason is that ZnO reacted with SA during vulcanization. Consequently, it is believed that the compounding at ambient temperature is insufficient for the formation of ZDS and ZDS is predominately formed during vulcanization. The *in situ* formed ZDS could not survive as it undergoes polymerization under heating, therefore the diffractions for ZDS are not observed in the vulcanizates. We studied the polymerization of ZDS initiated by the free radical generated by the decomposition of DCP through DSC. We mixed the model compound C with DCP, then sealed the mixture in DSC pan and heated to 200°C at 10°C/min, and the heat flow during heating was recorded, as can be seen in Figure 6. It is clear that there is a exothermic peak between 133 and 193°C. It is believed that the

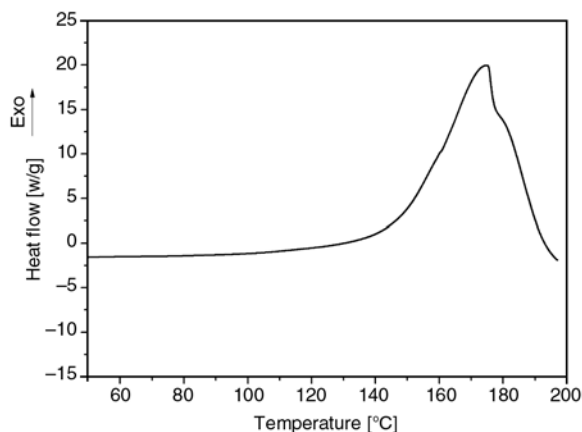


Figure 6. DSC graph of the ZDS/DCP mixture

exothermic peak is due to the polymerization of ZDS and the enthalpy for the polymerization of ZDS is approximately 477.4 J/g.

Since SA is also reactive to rubber chains during vulcanization, the grafting of SA onto rubber chains is a competitive reaction to the formation of ZDS [27, 28]. To optimize the formation of ZDS in the rubber compounds, the open mill compounded rubber compounds excluding DCP were heat treated at 120°C for 15 min. The XRD patterns of the heat treated rubber compounds are revealed in Figure 7. It is obvious that a new diffraction peak appears around 7.8° when SA content is higher than 10 parts [phr]. The intensity of this peak is increased with the content of SA. The new diffraction can be assigned to the intermediate substance formed by the reaction of ZnO and SA as indicated above. This intermediate substance could be readily converted to ZDS upon further heating. The XRD patterns of the heat treated rubber vulcanizates are revealed in Figure 8. It is clear that after vulcaniza-

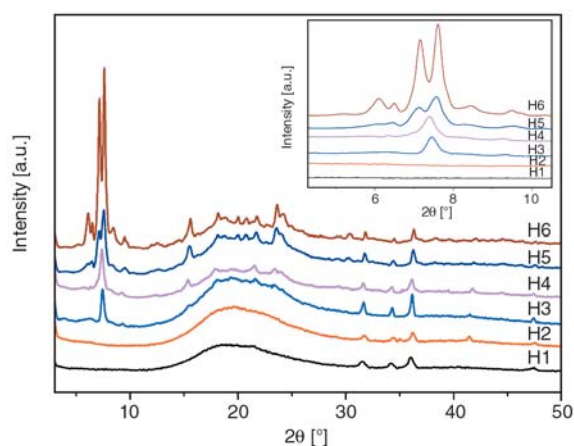


Figure 7. XRD patterns of the heat treated rubber compounds

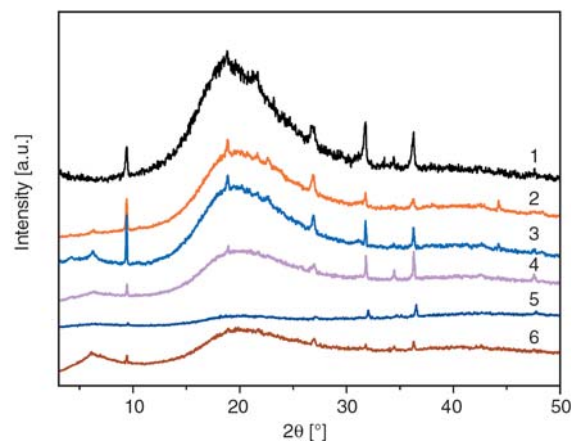


Figure 8. XRD patterns of the heat treated vulcanizates

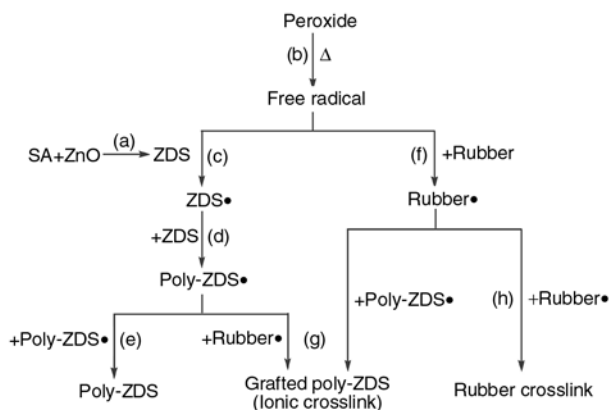


Figure 9. Possible reactions for NBR/SA/ZnO/DCP system

tion, the diffraction peaks of the intermediate substance are disappeared. However, the diffraction of ZDS could hardly be observed. It could be explained that during vulcanization, the intermediate substance is converted to ZDS, and the formed ZDS undergoes polymerization at the initiation of the free radical. The possible reaction pathways for the present system are illustrated in Figure 9. Reaction (a) represents the *in situ* formation of ZDS, including the formation of intermediate substance and its conversion to ZDS. Reaction (b) represents the generation of free radical by the decomposition of DCP. Reactions (c) and (d) represent the initiation of ZDS and chain growth of poly-ZDS. Reaction (e) represents the homopolymerization of ZDS by radical addition and termination by radical coupling. Reaction (f) represents the initiation of rubber chains. Reaction (g) represents the copolymerization of poly-ZDS and rubber chains, and the Reaction (g) will form ionic crosslink in the system. Reaction (h) represents the crosslink of the rubber chains.

4.2. Curing characteristics of rubber compounds

Figure 10 shows the vulcanization curves of the rubber compounds with different SA loading. As can be seen, the inclusion of SA leads to significant increase in the torque of compounds. The maximum torque of the compounds is consistently increased with the loading of SA. This may be due to reinforcement of ZDS particles and the strengthened interfacial interaction through the grafting of ZDS onto the rubber chains [19, 20]. As also seen from

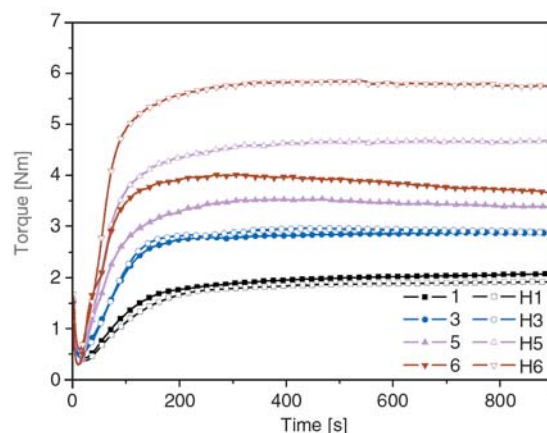


Figure 10. Comparison of the vulcanization curves of NBR/ZDS compounds with or without heat treatment

Figure 10, the increase of maximum torque with increasing SA content is also observed in the heat treated rubber compounds. When the SA content is lower than 10 phr, the difference between the torques of the rubber compounds with and without heat treatment is negligible. However, when the SA content is further increased, the torque of the compound with heat treatment is remarkably higher than that without heat treatment. This could be explained by the effectively increased ZDS content in the heat treated samples. When the open mill compounded sample is subjected to compression moulding, part of SA could not survive due to the radical polymerization and, as a consequence, the ZDS content is considerably lower than that with preheating before the compression moulding. The reinforcement of the rubber compounds is primarily contributed by the crosslinked ZDS particles, consequently the preheat compounds which possesses higher ZDS content show higher torque.

Figure 11 summarizes the scorch time (T_{s2}) and vulcanization time (T_{c90}) of the rubber compounds with different SA loading. As shown, the T_{s2} exhibits a slight decrease with increasing SA content. T_{c90} of the compound with SA is also lower than the control sample although its trend is not consistently decreasing with SA loading. It is noticeable that there are little changes in T_{s2} and T_{c90} after the preheating, suggesting the limited effect of the preheating on the scorch or curing time of the rubber compounds. The curing rate index (CRI), which indicates the rate of cure of the compounds, defined as $(MH-ML)/(T_{c90}-T_{s2})$, is summarized in Figure 12. ML and MH represent the

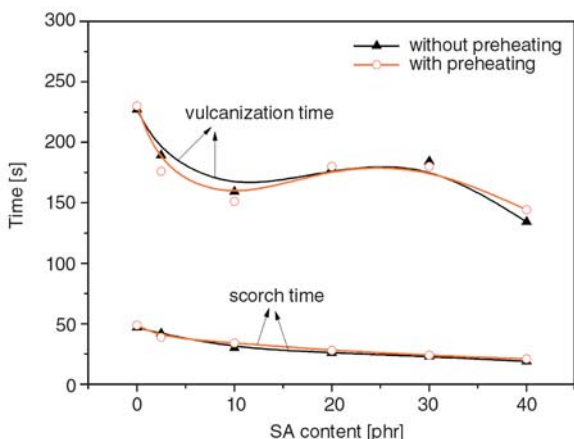


Figure 11. Vulcanization characteristics of NBR/ZDS compounds

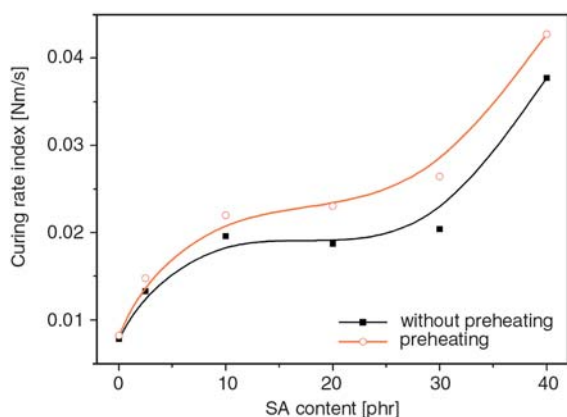


Figure 12. Curing rate index of NBR/ZDS compounds

minimum and maximum torque, respectively. A higher value of CRI means a higher rate of vulcanization. It can be seen that the value of CRI increases with the increasing of SA loading, indicating the acceleration of vulcanization by SA. And the heat treatment can further improve the curing rate. The CRI is mainly dependent on the crosslinking reactivity of the compound. The compound with higher ZDS content should have higher crosslinking reactivity as it can undergo crosslinking itself and the SA can only be linearly polymerized. Higher SA content or preheating on the uncured compounds are all beneficial to the formation of ZDS, consequently those samples show higher CRI values.

4.3. Structure, morphology and mechanical properties of NBR vulcanizates with variable SA content

Table 2 summarizes the crosslink density of NBR vulcanizates with varying SA contents. The incre-

Table 2. Crosslink density of NBR vulcanizates with variable SA content (the data in the parenthesis is for the sample with preheating)

	$V_e \cdot 10^{-4}$ [mol·cm ⁻³]	$V_{e1} \cdot 10^{-4}$ [mol·cm ⁻³]	$V_{e2} \cdot 10^{-4}$ [mol·cm ⁻³]
1 (H1)	4.65 (4.51)	4.49 (4.23)	0.16 (0.28)
2 (H2)	4.91 (4.83)	3.79 (3.58)	1.12 (1.25)
3 (H3)	5.37 (5.66)	2.31 (2.42)	3.06 (3.24)
4 (H4)	6.46 (7.25)	1.77 (1.83)	4.69 (5.42)
5 (H5)	7.61 (9.01)	1.39 (1.54)	6.22 (7.47)
6 (H6)	8.74 (10.09)	0.83 (1.05)	7.91 (9.04)

ment in ionic crosslink density is indicative of the polymerization of ZDS during the vulcanization. From Table 2, it can be concluded that the total crosslink density (V_e) and ion crosslink density (V_{e2}) are increased with SA, while the covalent crosslink density (V_{e1}) has the reverse trend.

The effect of preheating on the crosslink density of the vulcanization is also shown in Table 2. It is noticeable that the values of the V_e and V_{e2} of the heat treated samples are higher than those of the vulcanizates without heat treated. The increase in the V_{e2} indicates more ZDS is formed in the pre-heated samples. Also, it is noticed that when SA content is more than 20 phr, 75–90% of the crosslink is due to ionic crosslinks. The high content of ionic crosslinks is an indication of higher content of crosslinked ZDS, which is important for the reinforcement of the present systems.

TEM is used to study the morphology of the *in situ* formed and polymerized ZDS in NBR vulcanizates. Figure 13 shows the morphologies of the NBR/ZDS composites with and without heat treatment. It clearly indicates that there are significant amount of nano-level dispersion, the darker phase, in TEM photographs of the ZDS/NBR composites with 8 phr of ZnO and 20 phr of SA investigated in this

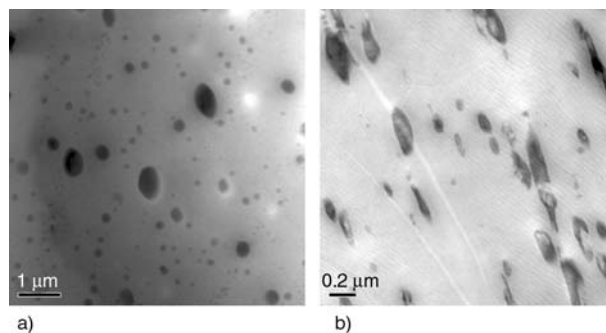


Figure 13. Morphology of the NBR/ZDS composites (20 phr of SA and 8 phr of ZnO were included for both samples. left, without heat treatment; right, with heat treatment)

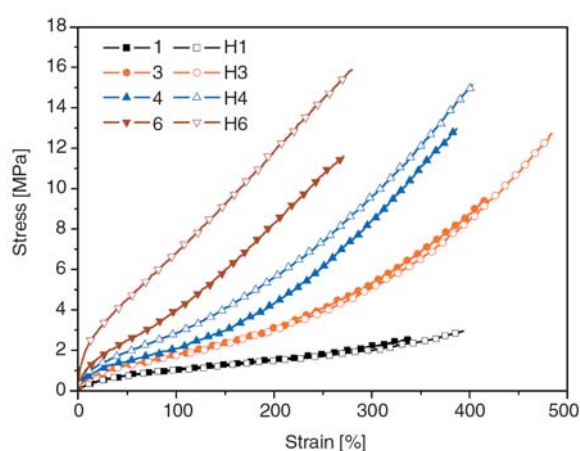
Table 3. Mechanical properties of NBR vulcanizates with variable SA content (the data in the parenthesis is standard deviation)

Sample code	100% modulus [MPa]	Tensile strength [MPa]	Shore A hardness	Tear strength [kN·m ⁻¹]	Elongation at break [%]	Permanent set [%]
1	1.06 (±0.08)	2.78 (±0.31)	47	12.79 (±1.47)	378.3 (±23.2)	3
H1	1.04 (±0.02)	2.82 (±0.21)	47	12.94 (±1.16)	392.5 (±10.7)	3
2	1.14 (±0.07)	4.94 (±0.38)	48	12.72 (±1.33)	435.6 (±24.4)	4
H2	1.07 (±0.03)	5.95 (±0.56)	48	18.53 (±1.04)	499.1 (±25.7)	6
3	1.51 (±0.06)	9.44 (±1.11)	53	28.41 (±0.82)	423.3 (±8.5)	7
H3	1.75 (±0.07)	11.89 (±1.11)	54	32.56 (±2.12)	461.5 (±25.2)	8
4	2.01 (±0.14)	12.70 (±0.96)	61	33.68 (±1.01)	380.5 (±16.5)	4
H4	2.92 (±0.06)	16.08 (±1.21)	66	42.75 (±1.02)	403.3 (±12.3)	6
5	3.25 (±0.14)	11.31 (±0.94)	64	39.66 (±1.09)	271.2 (±18.8)	4
H5	4.81 (±0.18)	15.73 (±1.51)	75	45.41 (±1.66)	324.1 (±21.9)	6
6	4.16 (±0.28)	11.81 (±1.01)	76	52.61 (±4.41)	274.0 (±26.6)	4
H6	3.76 (±0.08)	15.64 (±0.93)	83	66.18 (±0.59)	276.0 (±13.3)	4

work. It can be judged that the small dark domains in the TEM photographs could represent the Zn-rich regions, that is, the aggregates of poly-ZDS in the present system. The detailed mechanism of the formation of such inclusions in the rubber matrix, however, is still under investigation.

The reinforcing effect of *in situ* formed ZDS on NBR was summarized in Table 3. It is revealed that the 100% modulus, tensile strength, tear strength and shore A hardness are increased with SA content. For the SA included samples, the elongation at break is decreased with SA content. The incorporation of SA has little influence on the permanent set of NBR, and the value keeps at a low level for all the samples (below 10%). What is more, the pre-heated samples have improved mechanical properties than those without preheating, and the more SA is added, the greater discrepancy in mechanical properties. Five to six fold increases in 100% modulus, tensile strength and tear strength are achieved compared with those of the control sample. It can be concluded that *in situ* formed ZDS shows promising reinforceability towards NBR. Typical stress-strain curves are presented in Figure 14. One can see that low SA loading is beneficial to the increase in the elongation at break while higher loading SA is beneficial to improving the modulus and the strength of the NBR vulcanizate effectively.

The largely enhanced mechanical properties can mainly be explained as follows. When SA is incorporated, ZDS can be formed and crosslinked during rubber vulcanization. ZDS could also be grafted onto NBR chains and the interfacial bonding is enhanced. When low loading of SA is added, little

**Figure 14.** Typical stress-strain curves of NBR/ZDS vulcanizates

ZDS is formed and so the reinforcing effect is limited. At such a situation, the linear poly(sorbic acid) leads to the higher of the elongation at break and the increased permanent set. When large amount of SA is incorporated, most of SA could be converted to ZDS and therefore a crosslinked ZDS particle reinforced rubber network with excellent interfacial bonding is resulted. More ZDS is formed, higher reinforcement is observed in the systems. It is well documented that *in situ* formed zinc dimethacrylate acid has a significant reinforcement on rubbers [9–13, 17]. Compared with the reported systems reinforced by the unsaturated metal carboxylates, although the increases in the mechanical performance do not surpass the previously reported ones, the present systems possess several advantages such as SA is a solid and edible substance with versatile reactivity and it is much cheaper than (meth)acrylic acid.

5. Conclusions

The NBR compounds could be effectively reinforced by *in situ* formed ZDS through the reaction between SA and ZnO during rubber compounding. Limited ZDS was formed during open mill compounding and most of ZDS was formed during the vulcanization. Preheating on the uncured compounds prior to the vulcanization was effective in increasing the ZDS content. Incorporation of ZDS led to higher curing rate although the scorch time and vulcanization time were practically independent of the ZDS content. Inclusion of ZDS significantly increased the ionic bond content in the vulcanizates. The *in situ* formed ZDS showed promising reinforceability towards the NBR compounds. The modulus, tensile strength, tear strength and hardness were found to be increased consistently with the content of ZDS. Preheating of the compounds before the compression moulding was beneficial to the formation of ZDS, and consequently the increases in mechanical properties. At 40 phr of SA and 16 phr ZnO, five to six fold increase of tensile strength and tear strength of the neat NBR vulcanizate were achieved. The TEM results confirmed the nano-dispersion structure of the polymerized ZDS in the NBR matrix.

Acknowledgements

The authors thank the financial supports from the National Natural Science Foundation of China (50873035, 50933005), Guangdong Natural Science Foundation (151008901000137), Fundamental Research for the Central Universities (200922007) and National High-tech R&D Program (863 Program, 2009AA03Z338).

References

- [1] Payne A. R., Whittaker R. E.: Reinforcement of rubber with carbon black. *Composites*, **1**, 203–214 (1970). DOI: [10.1016/0010-4361\(70\)90005-4](https://doi.org/10.1016/0010-4361(70)90005-4)
- [2] Wagner M. P.: Reinforcing silicas and silicates. *Rubber Chemistry and Technology*, **49**, 703–774 (1976).
- [3] Bandyopadhyay A., Maiti M., Bhowmick A. K.: Synthesis, characterisation and properties of clay and silica based rubber nanocomposites. *Materials Science and Technology*, **22**, 818–828 (2006). DOI: [10.1179/174328406X101265](https://doi.org/10.1179/174328406X101265)
- [4] Sadhu S., Bhowmick A. K.: Preparation and characterization of styrene butadiene rubber based nanocomposites and study of their mechanical properties. *Advanced Engineering Materials*, **6**, 738–742 (2004). DOI: [10.1002/adem.200400066](https://doi.org/10.1002/adem.200400066)
- [5] Sato K.: Ionic crosslink of carboxylate SBR. *Rubber Chemistry and Technology*, **56**, 942–958 (1983).
- [6] Przybyszewska M., Zaborski M.: The effect of zinc oxide nanoparticle morphology on activity in crosslinking of carboxylated nitrile elastomer. *Express Polymer Letters*, **3**, 542–552 (2009). DOI: [10.3144/expresspolymlett.2009.68](https://doi.org/10.3144/expresspolymlett.2009.68)
- [7] Costin R., Nagel W., Ekwall R.: New metallic coagents for curing elastomers. *Rubber Chemistry and Technology*, **64**, 152–161 (1991).
- [8] Costin R., Ekwall R., Nagel W.: Metallic coagent for curing elastomers. *Rubber World*, **206**, 27–30 (1992).
- [9] Nagata N., Sato T., Fujii T., Saito Y.: Structure and mechanical properties of hydrogenated NBR/zinc dimethacrylate vulcanizates. *Journal of Applied Polymer Science: Applied Polymer Symposium*, **53**, 103–120 (1994).
- [10] Yuan X. H., Peng Z. L., Zhang Y., Zhang Y. X.: The properties and structures of peroxide-cured NBR containing magnesium methacrylate. *Polymers and Polymer Composites*, **7**, 431–436 (1999).
- [11] Yuan X. H., Peng Z. L., Zhang Y., Zhang Y. X.: *In situ* preparation of zinc salts of unsaturated carboxylic acids to reinforce NBR. *Journal of Applied Polymer Science*, **77**, 2740–2748 (2000). DOI: [10.1002/1097-4628\(20000919\)77:12<2740::AID-APP220>3.0.CO;2-X](https://doi.org/10.1002/1097-4628(20000919)77:12<2740::AID-APP220>3.0.CO;2-X)
- [12] Peng Z. L., Liang X., Zhang Y. X., Zhang Y.: Reinforcement of EPDM by *in situ* prepared zinc dimethacrylate. *Journal of Applied Polymer Science*, **84**, 1339–1345 (2002). DOI: [10.1002/app.10112](https://doi.org/10.1002/app.10112)
- [13] Yin D. H., Zhang Y., Zhang Y. X., Peng Z. L., Fan Y. Z., Sun K.: Reinforcement of peroxide-cured styrene-butadiene rubber vulcanizates by methacrylic acid and magnesium oxide. *Journal of Applied Polymer Science*, **85**, 2667–2676 (2002). DOI: [10.1002/app.10641](https://doi.org/10.1002/app.10641)
- [14] Yin D. H., Zhang Y., Peng Z. L., Zhang Y. X.: A comparison between the SBR vulcanizates reinforced by magnesium methacrylate added directly or prepared *in situ*. *European Polymer Journal*, **39**, 99–105 (2003). DOI: [10.1016/s0014-3057\(02\)00171-4](https://doi.org/10.1016/s0014-3057(02)00171-4)
- [15] Sato T., Fujino A., Hayashi S., Oyama M., Ono K.: Simulation of crosslink and graft mechanism of hydrogenated-NBR/zinc di-methacrylate composites by moving die rheometer. *Rubber Chemistry and Technology*, **75**, 943–954 (2002).

- [16] Lu Y. L., Liu L., Yang C., Tian M., Zhang L. Q.: The morphology of zinc dimethacrylate reinforced elastomers investigated by SEM and TEM. *European Polymer Journal*, **41**, 577–588 (2005).
DOI: [10.1016/j.eurpolymj.2004.10.019](https://doi.org/10.1016/j.eurpolymj.2004.10.019)
- [17] Lu Y. L., Liu L., Tian M., Geng H. P., Zhang L. Q.: Study on mechanical properties of elastomers reinforced by zinc dimethacrylate. *European Polymer Journal*, **41**, 589–598 (2005).
DOI: [10.1016/j.eurpolymj.2004.10.012](https://doi.org/10.1016/j.eurpolymj.2004.10.012)
- [18] Kaang S., Jin W., Kader M. A., Nah C.: Effects of blend composition and mixing method on mechanical and morphological properties of zinc dimethacrylate-reinforced acrylonitrile-butadiene copolymer nanocomposites. *Polymer-Plastics Technology and Engineering*, **43**, 1517–1538 (2004).
DOI: [10.1081/PPT-200030263](https://doi.org/10.1081/PPT-200030263)
- [19] Guo B. C., Chen F., Lei Y. D., Liu X. L., Wan J. J., Jia D. M.: Styrene-butadiene rubber/halloysite nanotubes nanocomposites modified by sorbic acid. *Applied Surface Science*, **255**, 7329–7336 (2009).
DOI: [10.1016/j.apsusc.2009.03.092](https://doi.org/10.1016/j.apsusc.2009.03.092)
- [20] Guo B. C., Chen F., Lei Y. D., Jia D. M.: Tubular clay composites with high strength and transparency. *Journal of Macromolecular Science Part B: Physics*, **49**, 111–121 (2010).
DOI: [10.1080/00222340903346239](https://doi.org/10.1080/00222340903346239)
- [21] Guo B. C., Chen F., Lei Y. D., Chen W. W., Jia D. M.: Significantly improved performance of rubber/silica composites by addition of sorbic acid. *Polymer Journal*, **42**, 319–326 (2010).
DOI: [10.1038/pj.2010.4](https://doi.org/10.1038/pj.2010.4)
- [22] Flory P. J., Rehner J. J.: Statistical mechanics of cross-linked polymer networks. II. swelling. *Journal of Chemical Physics*, **11**, 521–526 (1943).
DOI: [10.1063/1.1723792](https://doi.org/10.1063/1.1723792)
- [23] Flory P. J.: Statistical mechanics of swelling of network structures. *Journal of Chemical Physics*, **18**, 108–111 (1950).
DOI: [10.1063/1.1747424](https://doi.org/10.1063/1.1747424)
- [24] Shvarts A. G.: Evaluation of rubber-solvent interaction. *Rubber Chemistry and Technology*, **31**, 691–698 (1958).
- [25] Sheehan C. J., Bisio A. L.: Polymer-solvent interaction parameters. *Rubber Chemistry and Technology*, **39**, 149–192 (1966).
- [26] Dolgoplosk B. A., Tinyakova E. I., Reikh V. N., Zhuravleva T. G., Belonovskaya G. P.: Carboxylic rubbers. I. Synthesis and structures. *Rubber Chemistry and Technology*, **32**, 321–327 (1959).
- [27] Kataoka S., Ando T.: Asymmetric induction in radical polymerization of sorbic acid in the presence of chitosan (in Japanese). *Kobunshi Ronbunshu*, **37**, 375–382 (1980).
- [28] Matsumoto A., Oshita S., Fujioka D. A.: A novel organic intercalation system with layered polymer crystals as the host compounds derived from 1,3-diene carboxylic acids. *Journal of the American Chemical Society*, **124**, 13749–13756 (2002).
DOI: [10.1021/ja020869c](https://doi.org/10.1021/ja020869c)

Thermal properties and flame retardancy of an ether-type UV-cured polyurethane coating

L. J. Chen^{1,2}, Q. L. Tai^{1,3}, L. Song¹, W. Y. Xing¹, G. X. Jie⁴, Y. Hu^{1,4*}

¹State Key Laboratory of Fire Science, University of Science and Technology of China, 96 Jinzhai Road, Hefei, Anhui 230026, P.R. China

²Department of Polymer Science and Engineering, University of Science and Technology of China, 96 Jinzhai Road, Hefei, Anhui 230026, P.R. China

³Suzhou Institute for Advanced Study, University of Science and Technology of China, 166 Ren'ai Road, Suzhou, Jiangsu 215123, P.R. China

⁴State Key Laboratory of Environmental Adaptability for Industrial Products, China National Electric Apparatus Research Institute, Guangzhou, 510300, P.R. China

Received 28 March 2010; accepted in revised form 19 May 2010

Abstract. A new UV-reactive monomer piperazine-N,N'-bis(acryloxyethylaryl-phosphoramidate) (N-PBAAP) containing phosphorus and nitrogen was synthesized and used as flame retardant for an ether-type UV-cured polyurethane acrylate (PUA) coating. The thermal properties of the PUA films were investigated by thermogravimetric analysis (TGA) in air and nitrogen atmosphere. The TGA results showed that the incorporation of N-PBAAP can obviously enhance the char residue of the PUA coatings. From the TGA and real time Fourier transformed infrared spectroscopy (RT-FTIR) results, different degradation behaviors were observed in the PUA coatings with different N-PBAAP content. The combustibility of the PUA coatings was evaluated by microscale combustion calorimeter (MCC). The MCC results revealed that the addition of N-PBAAP in the coatings can significantly reduce the peak Heat Release Rate (pHRR), Heat Release Capacity (HRC) and the Total Heat Release (THR) of the samples. Furthermore, dynamical mechanical thermal analysis (DMA) was employed to examine the viscoelastic properties of the PUA films. It was found that the incorporation of N-PBAAP in the formulation can bring in more functional groups to the coatings, which results in an increase of the glass transition temperature (T_g) and cross linking density (XLD) of the films.

Keywords: coatings, flame retardancy, polyurethane acrylate, thermal properties

1. Introduction

It is well known that the conventional solvent-based coatings will cause environmental pollution during their thermal curing processes by emitting a large amount of volatile organic compounds (VOC) and other hazardous air pollutants (HAP). The radiation curing process has been found to be an effective alternative to solvent borne technology in the coating industry [1]. Radiation curing technology, mostly UV curing, offers many advantages during the curing process, in relation to the ecology or

environment, energy conservation, economics and in the excellent performance of products [2–4]. The most commonly used UV-curable formulations involve unsaturated acrylic oligomers, including epoxy acrylates, polyester acrylates, polyether acrylates, urethane acrylates and silicone acrylates [5–8]. Among the oligomers used for UV-curable coatings, urethane acrylate oligomers offer a wide range of excellent application properties, such as high impact and tensile strength, abrasion resistance and toughness etc. As a result, UV-curable

*Corresponding author, e-mail: yuanhu@ustc.edu.cn

© BME-PT

urethane coatings have found a large number of applications on various substrates such as wood, plastics, metal, glass and ceramics [9–11].

In addition, PU coatings are often used as ‘passive fireproofing materials’, which refers to insulating systems designed to decrease heat transfer from a fire to the structure being protected. These are usually known as ‘intumescent coatings’, and can be described as follows: When the temperature of the coating surface reaches a critical temperature under the heat of the fire, the surface begins to decompose and is converted into a highly viscous liquid. At the same time, reactions are initiated that result in the release of inert gases with low thermal conductivity. These gases are trapped inside the viscous fluid leading to the formation of bubbles. The result is the expansion or foaming of the coating, sometimes up to several times its original thickness, to form a protective carbonaceous char that serves as an insulating barrier between the fire and the substrate. In fact, phosphorus-nitrogen (P-N) synergism, i.e. intumescent flame-retardant system, is recognized in many literatures [12–18]. In the P-N system, the phosphorus-containing parts act as an acid source, they usually break down at low temperature and take part in the formation process of the carbonaceous char. On the other hand, nitrogen-containing parts are usually used as gas source, they produce incombustible gases without toxic smoke and fog during heating. The evolving gases can dilute the concentration of the oxygen near the flame and cause the char to swell and hence provide an insulating multi-cellular protective layer. This shield limits at the same time the heat transfer from the heat source to the substrate and the mass transfer from the substrate to the heat source resulting in a conservation of the underlying material.

In this work, a new UV-curable intumescent flame retardant piperazine-*N,N'*-bis(acryloxyethylarylphosphoramidate) (N-PBAAP) with high phosphorus content (10.4 wt%) was synthesized combining phosphorus and nitrogen element into one molecule. N-PBAAP was then used as a UV-reactive monomer blending with urethane acrylate oligomer (UA) in different ratios. The thermal and combustion properties of the PUA films were investigated by TG and MCC, respectively. RT-FTIR was employed to investigate the changes of chemical structures of these samples during their thermal

degradation, in an attempt to elucidate the degradation mechanism. Furthermore, dynamical mechanical thermal properties were also investigated.

2. Experimental section

2.1. Materials

Phenyl dichlorophosphate (PDCP) was purchased from Deheng Chemical Co. (Shijiazhuang, China), and was freshly distilled before use. Triethylamine (TEA) and hydroxyethyl acrylate (HEA) were offered by China Medicine (Group) Shanghai Chemical Reagent Co. (Shanghai, China), and they were purified by distillation. Piperazine anhydrous was purchased from Sinopharm Chemical Reagent Co. Ltd. 2-Hydroxy-2-methyl-1-phenyl-1-propanone (Darocur 1173), kindly supplied by Ciba-Geigy, Switzerland, was used as a photoinitiator. UA, which is an ether-type urethane diacrylate oligomer with 15% TPGDA (Tripropylene glycol diacrylate) as dilute monomer, was supplied by Wuxi Tianjiao-saite Co. Tetrahydrofuran (THF) using as solvent was refluxed with sodium, and was then distilled before use.

2.2. Synthesis of N-PBAAP

PDCP (0.1 mol, 21.1 g) was placed into a three-necked flask in an ice-bath equipped with a mechanical stirrer and a dropping funnel. Triethylamine (0.21 mol, 21.2 g) was added by the funnel under stirring. HEA (0.1 mol, 11.6 g) was diluted with THF (20 ml) and was slowly dropped into the above reaction vessel within 2 hours. The mixture was then kept stirring for 4 hours. After that piperazine anhydrous (0.05 mol, 4.307 g) dissolved in dry THF (90 ml) was added dropwise over a period of 2 hours. Removal of precipitated triethylamine hydrochloride by filtering and evaporation of filtrate under a reduced pressure gave the crude product. The product was purified further by washing it with hydrochloric acid, aqueous solutions of 5 wt% sodium bicarbonate and saturated sodium chloride, respectively. Finally, a salmon pink viscous liquid was obtained (79.2% yield). The success of synthesis was confirmed by ¹H NMR and ³¹P NMR analysis.

¹H NMR (CDCl₃): δ (ppm) = 7.16–7.32 (aromatic H), 5.84–5.87 (CH=CH₂,trans), 6.08–6.15

(CH=CH₂, cis), 6.41~6.46 (CH=CH₂), 4.27~4.39 (–OCH₂CH₂O–), 3.13~3.15 (N(CH₂)₂); ³¹P NMR (CDCl₃): δ (ppm) = 4.38.

FTIR (KBr, cm⁻¹): 1263 (–P=O), 1165, 979 (–P–O–C), 1726 (–C=O), 1640, 1410, 812 (–C=C–), 930, 769 (–P–N–C).

2.3. Sample preparation

The mixtures of UA with N-PBAAP in different ratios were stirred thoroughly to get various homogeneous blends. UA, and UA/N-PBAAP blends were then poured into a mold sized 25×25 mm², and the thickness of the cured film is about 1 mm. Later the resin blends with 3 wt% Darocur 1173 were exposed to a UV irradiation equipment (80 mW·cm⁻², made by Lantian Co., China), which emits light in the near UV (characterized wavelength, 340~360 nm) in air atmosphere. The distance between the sample and UV lamp is 10 cm, and the exposure time is about 15 s. The structures of N-PBAAP, UA oligomer and the sample preparation process were shown in Figure 1.

2.4. Characterization and analysis

2.4.1. FTIR analysis

The FTIR spectra were recorded with MAGNA-IR 750 spectrometer (Nicolet Instrument Company, USA, part of Thermo Fisher Scientific) using KBr pellet. The transmission mode was used and the wavenumber range was set from 4000 to 400 cm⁻¹. Real time Fourier transform infrared (RT-FTIR) method was employed to study the thermo-oxidative degradation of the N-PBAAP/PUA cured films. Granule of the cured sample was mixed with

KBr powder, and the mixture was pressed into a tablet, which was then placed into the oven. The temperature of the oven was raised at a heating rate of about 10°C/min. RT-FTIR spectra were collected during the thermo-oxidative degradation of the cured samples.

2.4.2. ¹H NMR and ³¹P NMR analysis

¹H NMR and ³¹P NMR was performed on a AVANCE 400 Bruker spectrometer (Bruker Corporation, Billerica, MA, USA) at room temperature using chloroform-D as a solvent.

2.4.3. Thermogravimetric analysis (TGA)

The thermogravimetric analysis was carried out on a TGA Q5000 IR thermalgravimetric analyzer (TA Instruments, New Castle, Delaware, USA). About 5 mg of cured samples were put in ceramic crucibles and heated from 30 to 700°C at a heating rate of 20°C·min⁻¹ under air and nitrogen purge, respectively (flow rate of 100 ml/min).

2.4.4. Microscale combustion calorimeter (MCC)

The MCC tests were carried out on a Govmark MCC-2 Microscale Combustion Calorimeter (Govmark, Farmingdale, NY, USA), which is a pyrolysis-combustion flow calorimeter. In the test, 4–6 mg powdery cured samples were heated to 650°C at a heating rate of 1 K/s in an inert gas stream (nitrogen, 80 ml·min⁻¹). Then the volatile was mixed with oxygen (20 ml·min⁻¹) prior to entering a 900°C combustion furnace and the heat of com-

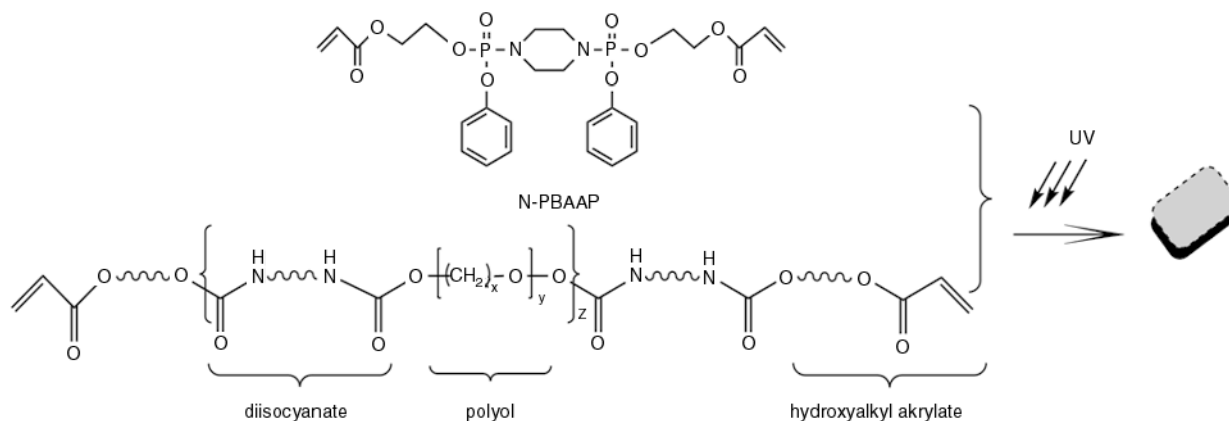


Figure 1. Preparation of PUA/N-PBAAP films

bustion of the pyrolysis products was measured by oxygen consumption principle.

2.4.5. DMA test

The tensile storage modulus (E') and tensile loss factors ($\tan\delta$) of the cured films were measured by a dynamic mechanical thermal analyzer (Diamond DMA, PerkinElmer Co., Waltham, MA, USA) at a frequency of 10 Hz and a heating rate of $10^\circ\text{C}\cdot\text{min}^{-1}$ in the range of -75 to 125°C with $25\times 5\times 1\text{ mm}^3$ specimens. The crosslink density (XLD) as the molar number of elastically effective network chain per cube centimeter of the film, was calculated from the storage modulus in the rubbery plateau region according to Equation (1):

$$XLD = \frac{E'}{3RT} \quad (1)$$

where E' is the elastic storage modulus, R is the ideal gas constant, and T is the temperature in K.

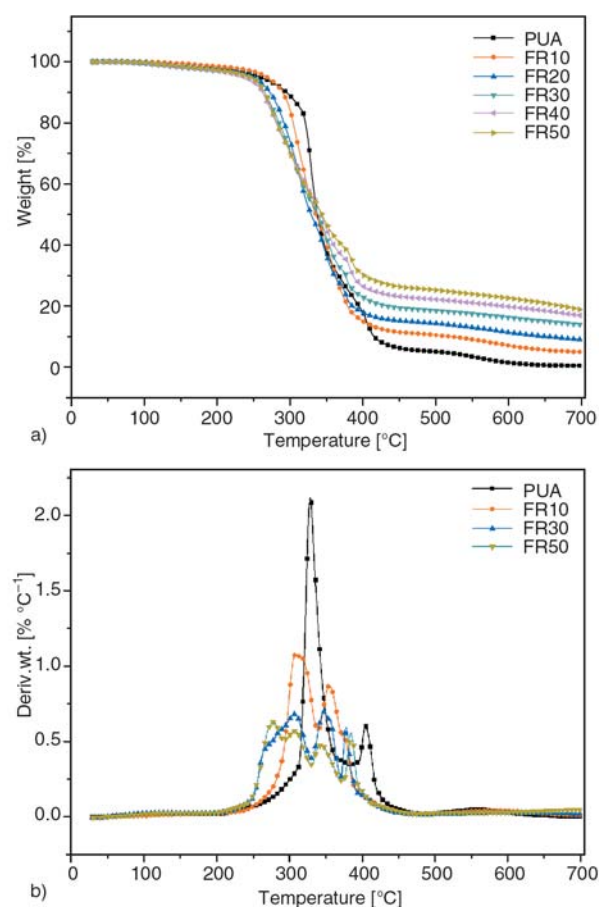


Figure 2. (a) TG curves (b) DTG curves of PUA and PUA/N-PBAAP cured films in air

3. Results and discussion

3.1. Thermogravimetric analysis

Thermogravimetric analysis (TGA) was used to investigate the effect of N-PBAAP on the thermal stability of the PUA coatings. Figure 2a and Figure 3a show the TG curves of PUA and PUA/N-PBAAP cured films in air and nitrogen atmosphere; Figure 2b and Figure 3b show the DTG curves of PUA and PUA films with 10, 30, 50 wt% N-PBAAP loadings. The details of the TGA data for the coating compositions in air and nitrogen are presented in Tables 1 and 2, respectively, showing the temperatures for different percentage weight losses and the percentage char residues at different temperatures of the coatings.

From Figure 2a, it can be seen that, in air atmosphere, all the PUA/N-PBAAP films have more char residues than the pure PUA film at high temperature regions. As can be seen from Figure b, the pure PUA film undergoes a major weight loss in the temperature range of 250 – 360°C due to thermal

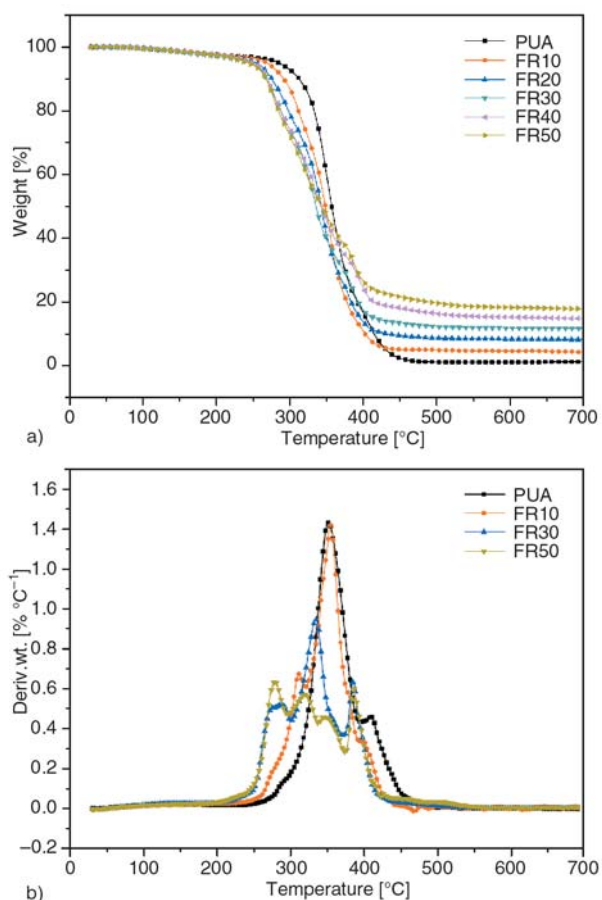


Figure 3. (a) TG curves (b) DTG curves of PUA and PUA/N-PBAAP cured films in nitrogen

Table 1. Details of the TGA data for the coating compositions in air

Sample name	PUA [wt%]	N-PBAAP [wt%]	Temperature [°C]/wt. loss			Char residue [wt%]/°C		
			10%	30%	50%	500	600	700
PUA	100	0	295	327	338	5.0	1.4	0.5
FR10	90	10	290	314	336	10.5	7.0	4.9
FR20	80	20	272	305	329	14.3	11.4	9.1
FR30	70	30	265	302	339	18.6	16.3	14.0
FR40	60	40	262	301	343	22.2	19.8	16.9
FR50	50	50	265	301	344	25.2	22.6	18.8

Table 2. Details of the TGA data for the coating compositions in nitrogen

Sample name	PUA [wt%]	N-PBAAP [wt%]	Temperature [°C]/wt. loss			Char residue [wt%]/°C		
			10%	30%	50%	500	600	700
PUA	100	0	313	343	357	1.1	1.0	1.0
FR10	90	10	292	328	349	4.9	4.6	4.3
FR20	80	20	276	319	343	8.7	8.3	8.2
FR30	70	30	268	309	336	12.3	11.8	11.6
FR40	60	40	270	310	342	16.4	15.2	14.7
FR50	50	50	268	305	344	19.6	18.3	17.8

decomposition of the organic coating and then a minor degradation step in the temperature range of 400–430°C due to the oxidation of the residue formed on thermal decomposition of the coating. The char residue of pure PUA cured film is 0.5% at 700°C as shown in Table 1, indicating the complete decomposition of PUA film. However, the PUA/N-PBAAP coatings reveal different trends of thermal degradation. The initial degradation temperatures of the blends are lowered by the addition of N-PBAAP, and the DTG curves show broader peaks with weaker intensity and more degradation steps as the N-PBAAP loading increases in the blends. As presented in Figure 2b, FR50 (PUA film with 50 wt% N-PBAAP loading) shows a four-step thermal degradation process. The first region can be assigned to the decomposition of the phosphate, whereas the second is due to the thermal pyrolysis of side chains of the acrylate and the formation of char. The third region is attributed to the decomposition of the unstable structures in the char, and the last step may result from the oxidation of the exposed matrix as well as the further oxidation of the char residue formed before [12].

Comparing the DTG curves shown in Figure 2b and Figure 3b, it can be seen that the pure PUA film exhibits similar thermal degradation behavior in nitrogen and in air, i.e. a major decomposition of the coating before 400°C. But in the case of FR10 (PUA film with 10 wt% N-PBAAP loading), different degradation behaviors of the films are observed under different circumstances. We can

see that, in air, sample FR10 shows obvious two-step degradation process, implying that the incorporation of N-PBAAP in the coating can slow down the rapid decomposition of the PUA matrix. While in nitrogen FR10 represents a major one-step degradation which is similar to that of the pure PUA film. This suggests that, in an inert atmosphere, the thermal degradation of the PUA film cannot be significantly influenced when the loading of N-PBAAP is low, which is different from that in air. However, as the loadings of N-PBAAP in the coatings increase, the cured flame retardant samples tend to degrade in the same way during heating both in air and nitrogen. Take FR50 for example, it shows a four-step degradation process in nitrogen as the same as that in air.

According to the above analysis and the data obtained from TGA, it can be concluded that the incorporation of N-PBAAP in the PUA films can obviously enhance the flame retardancy and the char residues of the coatings both in air and in nitrogen.

3.2. Combustion properties of PUA/N-PBAAP cured films

The Microscale Combustion Calorimeter (MCC) is one of the most effective methods for investigating the combustion properties of polymer materials. The test improves upon previous methods by directly measuring the heat of combustion of the gases evolved during controlled heating of the sam-

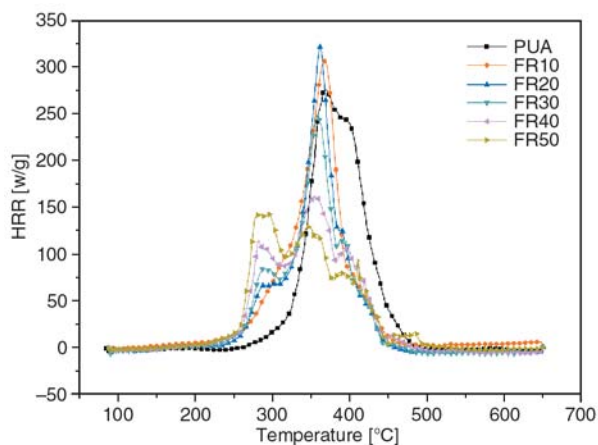


Figure 4. The heat release rate (HRR) curves of PUA, and PUA/N-PBAAP cured films

ples. As a result, the flammability parameters determined by MCC correlate with the intrinsic flammability properties of polymers and it offers a convenient methodology for estimating the fire hazard potential of a material from just a few milligrams of samples [19].

Figure 4 shows the heat release rate (HRR) curves of PUA, and PUA/N-PBAAP cured films blended in different ratios and the corresponding combustion data are presented in Table 3. It is found that the peak HRR (pHRR) of PUA blends decreases with the increase of N-PBAAP content. Compared with the pure PUA film, the pHRR of the sample containing 50 wt% N-PBAAP decreased from 275.3 to 142.5 W/g. On the other hand, it is observed that the films with low content of N-PBAAP (FR10 and FR20) exhibit higher pHRR than that of the pure PUA film. This may be caused by the decomposition of the weak P–O–C structure in the phosphate at low temperature, which may release combustible low-molecule-weight segments during degradation due to no oxidation in an inert atmosphere. Attributed to the same reason, the temperature at maximum pyrolysis rate (T_{max}) also decreases with the increasing N-PBAAP content. However, in view of the total heat release (THR), all blends

Table 3. Corresponding combustion data from MCC

Sample name	HRC [J/g·K]	pHRR [W/g]	THR [kJ/g]	T_{max} [°C]
PUA	279	275.3	23.0	368.5
FR10	300	303.5	21.0	366.9
FR20	318	321.6	19.1	361.8
FR30	247	249.3	18.7	358.2
FR40	164	161.7	18.5	354.7
FR50	142	142.5	18.6	294.4

have lower THR than pure PUA film. The heat release capacity (HRC), which is obtained by dividing the maximum value of the specific heat release rate (SHRR) with the heating rate in the test, is a material property. HRC appears to be a good predictor of flammability and propensity for ignition, and it is related to the decomposition kinetics and combustion parameters of the sample [20]. It can be seen from Table 3 that HRC shows the similar variation of pHRR, indicating the incorporation of N-PBAAP can effectively decrease the combustion potential of PUA. All the results above show that N-PBAAP is an effective flame retardant for PUA coatings.

3.3. Thermal degradation mechanism

With the purpose of elucidating the thermal degradation processes of the pure PUA and the flame retardant PUA films, three samples were selected (PUA, FR10 and FR50), and the characterization of these samples was conducted using RT-FTIR spectroscopy.

The real time FTIR observed for PUA, FR10 and FR50 at selected temperatures between RT (room temperature) and 450°C are shown respectively in Figure 5, Figure 6 and Figure 7. The assignments of the major bands observed at RT are summarized in Table 4 on the basis of recent IR studies of various types of polyurethanes and phosphates. The thermal degradation of polyurethanes has been reported in several studies [21, 22], it is considered that the degradation of an ether-type polyurethane begins with the dissociation and thermal decompo-

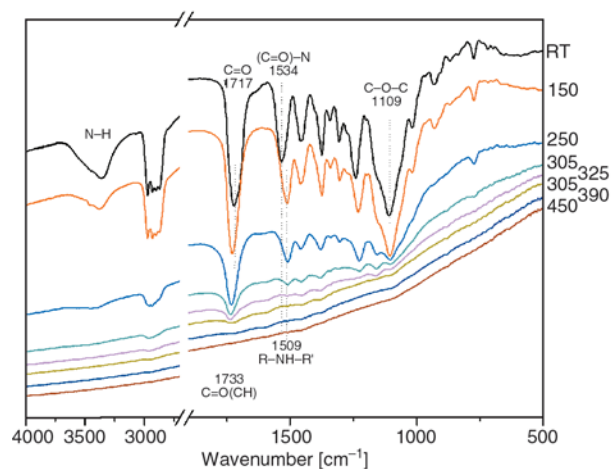


Figure 5. The real time FTIR spectra for PUA film at selected temperatures

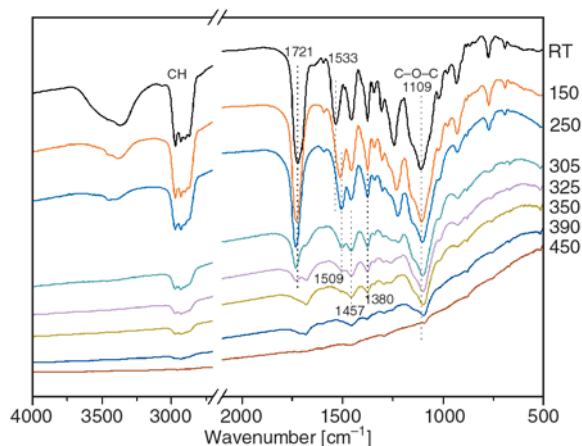


Figure 6. The real time FTIR spectra for sample FR10 at selected temperatures

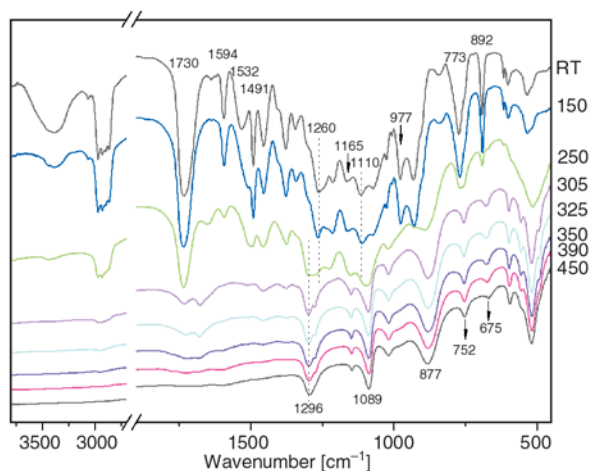


Figure 7. The real time FTIR spectra for sample FR50 at selected temperatures

Table 4. Assignments of peaks in real time FTIR of PUA, FR10 and FR50

Frequency [cm ⁻¹]	Assignment ^a
3480	(vs) free urethane N–H stretching
3400	(vs)N–H hydrogen-bonded to urethane >C=O
3310	(vs)N–H hydrogen-bonded to ether oxygen
2949, 2865	(as) CH ₂ and (s) CH ₂
1733	(vs) free C=O
1717	(vs) urethane C=O hydrogen-bonded to N–H
1594, 1491	(vs) skeleton benzene ring C–C
1534	(vs) C–N and (vb) N–H of urethane
1509	(vb) N–H of polyamine
1457, 1380	(vb)CH ₂ and CH ₃
1260	(vs) P=O
1165, 977	(vs) aromatic P–O–C
1110	(as) C–O–C
773, 692	(vb) aromatic C–H, out of plane bend

^a(vs): stretching vibration; (as): asymmetric stretching mode; (s): symmetric stretching mode; (vb): bending vibration

sition of the urethane hard segment. As shown in Figure 5, the intensities of the bands (around

3350 cm⁻¹) assigned to N–H decrease intensively with increasing temperature, and almost disappear at 250°C. At 150°C, the peak at 1717 cm⁻¹, which is attributed to the stretching mode of a C=O group hydrogen-bonded to urethane N–H, is shifted to higher wave number at 1733 cm⁻¹ (free C=O group) [23]. These mean that the hydrogen-bond dissociation and thermal decomposition of the urethane linkage have occurred at as low temperature as 150°C. However, as to the soft segment with ether structures, things are different. When temperature reaches 150°C, no significant changes are observed with the characteristic bands (1109 cm⁻¹ for C–O–C, 2850~2980 cm⁻¹ for C–H) of the ether structures, indicating that the thermal stability of the ether bonds is much higher than that of the urethane linkage. As temperature increases to 250°C, there is a large decrease in absorbance of the characteristic bands for ether structures, implying the rapid decomposition of the soft segment. But these bands are still detectable even above 325°C. Another peak that should be noticed is the absorbance at 1534 cm⁻¹, which is assigned to the C–N stretching and N–H deformation vibrations of the urethane group [8]. As can be seen at 150°C, this peak shifts to lower wave number at 1509 cm⁻¹, attributed to the N–H deformation of polyamine [5]. It can be speculated that the original urethane linkage has converted into various polyamines during the degradation. All above give evidences for the thermal degradation of the ether-type PUA film in air atmosphere. Undoubtedly, the degradation process is initiated by the decomposition of the urethane group at low temperature. This step probably leads to the formation of various polyamines, which decompose later, and the release of CO₂, as shown by Equation (2). Then the ether structures of the soft segment degrade intensively, releasing large amount of low-molecule-weight combustible fragments. All the bands can barely be examined at 350°C, suggesting the full decomposition of PUA film.



The spectral region for N–H from 3200 to 3600 cm⁻¹ mainly involves the bands of urethane N–H hydrogen-bonded to ether oxygen (3310 cm⁻¹), of urethane N–H hydrogen-bonded to urethane >C=O (3400 cm⁻¹), and free urethane N–H without hydrogen bonding (3480 cm⁻¹) [23]. For FR10, as

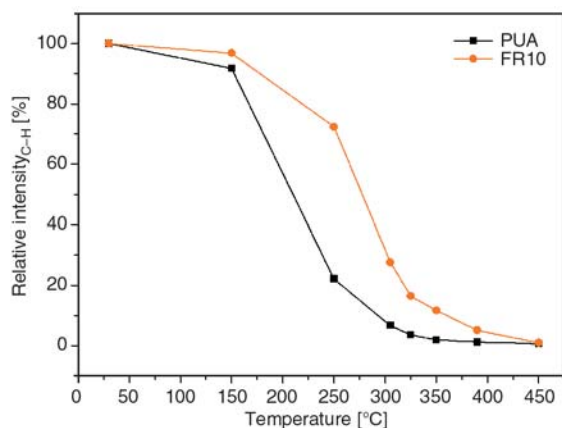


Figure 8. Relative peak intensity between 2800 and 3037 cm^{-1} for C–H bond in the FTIR spectrum of UV cured PUA and FR10 films at various temperatures

shown in Figure 6, the intensities of these peaks for N–H bond decrease rapidly as temperature increases, but they are still detected at 250°C. Simultaneously, it is obvious that the main peak shifts to higher wave number. These indicate the hydrogen bond formed by urethane N–H is gradually dissociated and the degradation of urethane linkage has been postponed. In view of the ether structures, peaks at 1109, 1380, 1457 cm^{-1} and peak region from 2850 to 2980 cm^{-1} (assigned to the vibration of soft segment shown in Table 4) are noted. Although the intensities of these peaks gradually decrease, they all remain as the temperature increases to even 390°C. Figure 8 shows the relative intensity of the peak region between 2800 and 3037 cm^{-1} in the FTIR spectra of cured PUA and FR10 films for C–H bond in CH_2 and CH_3 groups with temperature raising from 30 (RT) to 470°C. It is very clear that the C–H bond of pure PUA film decreases rapidly with increasing temperature from 150 to 250°C, whereas the absorbance between 2800 and 3057 cm^{-1} for FR10 film decreases slowly at this temperature region. According to the above, it can be concluded that the degradation of the soft segment is significantly postponed by the addition of N-PBAAP with 10 wt% content. In other words, the addition of N-PBAAP in the coatings can delay the decomposition of the PUA matrix, and thus improve the flame retardancy of the coating.

The probable reason for the improvement of flame retardancy of the sample containing 10 wt% N-PBAAP can be explained as follows. We have known that the ether bond exhibits excellent ther-

mal stability under an inert atmosphere [23], and the absorbance of stretching mode of C–O–C bond at 1109 cm^{-1} is much higher than that of other vibrational bands. During heating process, the degradation always begins with the breakage of the urethane group, releasing a lot of CO_2 , as has been proved above. Meanwhile, the N-PBAAP contained in the sample decomposes at a relatively low temperature around 200°C, as is common for a phosphorus-containing flame retardant, due to the scissions of the unstable P–O–C structures. The thermal degradation of N-PBAAP, in air, leads to the formation of phosphorus-rich compounds and also the release of various kinds of incombustible gases (carbon oxide, nitrogen, and low molecular weight PO_x etc.) [24]. These incombustible gases will provide a relatively inert environment for the remains of the sample, thus resulting in a delayed degradation of the matrix. However, it is difficult to confirm the formation of phosphorus-rich compounds by FTIR because of the masking effect of the broad and strong peak at 1109 cm^{-1} assigned to ether structure and the low content of N-PBAAP loading.

When the loading of N-PBAAP increases to 50 wt% in the coating, as shown in Figure 7, different thermal degradation behavior of the film is observed. The assignments of the main peaks for N-PBAAP are listed in Table 4. From Figure 7, it can be seen that the absorbance of peaks at 1165, 977 cm^{-1} [25, 26] and the broad peak at 3390 cm^{-1} , which are attributed to the stretching bands of P–O–C and N–H structures respectively, almost disappear at 250°C. These offer information that the initial degradation of FR50 involves the scission of the urethane linkage as well as the decomposition of a large amount of P–O–C structures of N-PBAAP. Meanwhile, the changes of several peaks are examined with increasing temperature. The peak for the P=O bond (1263 cm^{-1}) is shifted to higher wave number at 1294 cm^{-1} , which is assigned to the P=O stretching vibration of P–O– Φ structure, where Φ represents the graphite-like polynuclear aromatic structure [16, 27]. As the temperature elevates to 305°C, the bands of 773 and 692 cm^{-1} are shifted to lower wave numbers at 752 and 675 cm^{-1} , attributed to out-of-plane bending vibrations of aromatic C–H for P–O– Φ complex structures [16, 28]. In addition, new peaks at 1089 and 877 cm^{-1} assigned to symmetrical and

asymmetrical stretching vibrations of P–O–P structure also appear at elevated temperatures [29]. All these changes of the peaks in the spectra give significant evidences that the original phosphate structure of N-PBAAP has been converted into various kinds of P–O–P and P–O– Φ complex structures when temperature elevates to 305°C. However, the characteristic peaks for the ether structures are barely detected at 305°C. According to the above analysis, it can be concluded that a phosphorus-rich layer is formed on the surface of the PUA matrix due to the decomposition of N-PBAAP at low temperature. Combining with the gases released, it is believed that the intumescent char layer covering the surface of the matrix can serve as a heat barrier and protect the matrix from the heat and fire, thus resulting in an enhancement of the flame retardancy and a high char yield of the coatings.

In conclusion, according to the results obtained from the RT-FTIR, we have proposed different degradation mechanisms for the selected samples. The pure PUA film first decomposes from the urethane linkage, probably with the formation of various polyamines, and then the film degrades intensively between 150 to 305°C. For the sample FR10, the degradation of the coating is significantly delayed, and it is believed that a gas phase flame retardant mechanism is the dominant effect as the coating is burning. But for FR50, it is concluded that an intumescent phosphorus-rich char layer leads to the improved fire resistance of the film.

3.4. Dynamic mechanical thermal behavior

Dynamic mechanical thermal analysis (DMTA) was utilized to investigate the viscoelastic properties of the cured films in an effort to examine the microstructures of the polymer blends. The storage modulus reflects the elastic modulus of the coatings. The loss factor modulus is related to the energy lost due to the friction associated with the motion of polymer chains. The storage modulus (E') and loss factor ($\tan\delta$) curves of the pure PUA and its corresponding blends with N-PBAAP addition are shown in Figures 9a and 9b. The glass transition temperature (T_g) is defined as the peak temperature of $\tan\delta$ curve. T_s is the softening point defined as the extrapolated onset of the drop of storage modulus. Table 5 shows the data obtained from DMTA tests for all samples.

At the rubbery plateau ($T_g + 40^\circ\text{C}$), the E' values for FR30 is measured to be 13.2 MPa, compared with 9.5 MPa for that of pure PUA, almost an increase of 40% in storage modulus. However, as listed in Table 5, a decrease of E' values is observed with N-PBAAP content further increasing. The

Table 5. Rubbery storage modulus, T_s , T_g and crosslink density (XLD) from DMTA

Sample name	E' [MPa]	T_s [°C]	T_g [°C]	T_s/T_g	XLD [mmol·cm ⁻³]
PUA	9.5	-45.3	19.7	0.78	1.145
FR10	11.1	-50.4	27.4	0.74	1.307
FR20	13.2	-51.8	29.8	0.73	1.544
FR30	12.2	-52.3	39.1	0.71	1.389
FR40	11.2	-56.6	55.8	0.66	1.217
FR50	11.2	-63.2	60.3	0.63	1.203

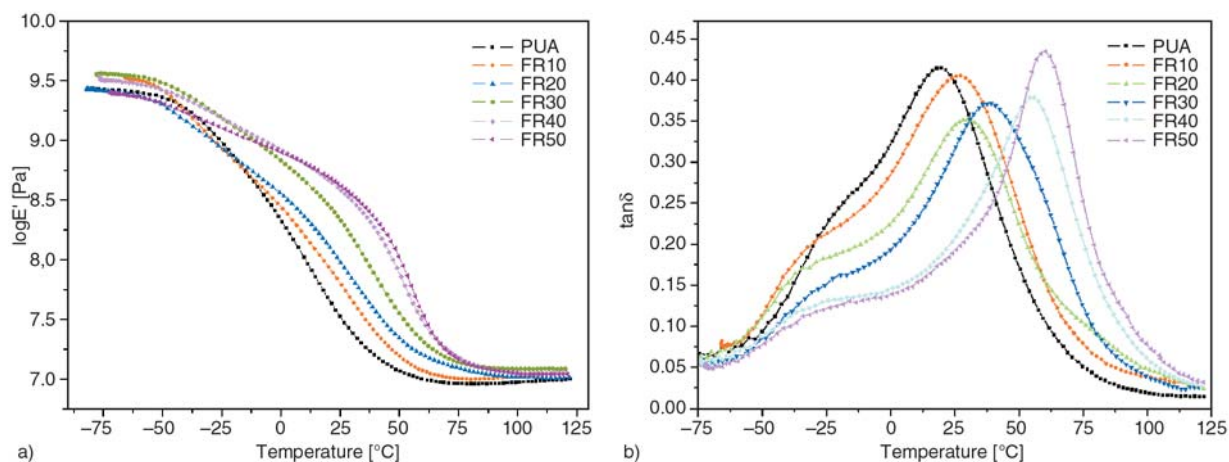


Figure 9. (a) The storage modulus (E') curves of PUA, and PUA/N-PBAAP cured films. (b) The loss factor ($\tan\delta$) curves of PUA, and PUA/N-PBAAP cured films

variation of crosslink densities (XLD) of the samples shows the same trend as that of E' .

These phenomena can be explained as follows. As far as the chemical structures of the two components are concerned, although both UA and N-PBAAP are difunctional oligomers i.e. diacrylates, N-PBAAP has a short molecular chain and low molecular weight compared with UA (Figure 1). As a result, the density of the acrylate group is higher for N-PBAAP than that of UA, which leads to the higher reactivity of N-PBAAP compared with UA oligomer. Therefore, as can be seen from Table 5, there is an increase in the glass transition temperature (T_g) of the samples from 19.7 to 60.3°C with increasing N-PBAAP content, due to the rigid and short chain structure and higher density of acrylate group brought in the blends by N-PBAAP. However, in terms of T_s/T_g , which expresses the width of $\tan\delta$ peak, things are different. It is a rule that a lower T_s/T_g ratio leads to a wider $\tan\delta$ peak. The peak width broadens as the number of branching modes increases, which produces a wider distribution of structures. The range of temperatures at which the different network segments gain mobility therefore increases. From Table 5, the T_s/T_g values of the samples decreased with increasing N-PBAAP content, indicating network heterogeneity increases of PUA/N-PBAAP films. According to the above, it can be concluded that the increasing of N-PBAAP content in the samples will at the same time bring in more functional groups and increase the network heterogeneity of the samples. Both of the two factors lead to the initial increase of the XLD and E' and then a decrease of them as N-PBAAP content increasing in the blends. Whatever, all the blends have a higher XLD than the pure PUA film.

In conclusion, the incorporation of N-PBAAP in the blends can obviously bring in more compactness and rigidity to the films, and increase the T_g of the coatings. To some extent, it is important for practical application. Although the network heterogeneity increases slightly, it doesn't significantly affect the properties of the films.

4. Conclusions

A UV-reactive monomer N-PBAAP has been synthesized, and found effective for improving the flame retardancy of an ether-type PUA coating.

The MCC test revealed that the pHRR and HRC of the PUA coatings are reduced significantly in comparison with the pure PUA film. The THR values of all blends are lower than that of the pure PUA. The results suggested that N-PBAAP is an effective flame retardant for PUA coatings. The TG results showed that the PUA/N-PBAAP cured films have different degradation processes in air and in nitrogen when the N-PBAAP loading is low. And the char residues of the PUA coatings are obviously enhanced by the incorporation of N-PBAAP. The RT-FTIR analysis gave evidences for different flame retarding mechanisms of N-PBAAP when incorporated in the PUA films at different ratios. With 10 wt% of N-PBAAP loading in the coating formulation, probably a gas phase mechanism holds the dominant effect as the blend is burning. But when the content of N-PBAAP increases to 50 wt%, a solid phase mechanism is proposed for the improved fire resistance of the film. According to the DMA analysis, it was found that the incorporation of N-PBAAP in the PUA films results in an increase of T_g and a highest cross linking density for the sample containing 20 wt% of N-PBAAP.

Acknowledgements

The work was financially supported by the Program for Specialized Research Fund for the Doctoral Program of Higher Education (200803580008), the Program for Science and Technology of SuZhou (SG-0841), the Program for the graduate innovation fund in University of Science and Technology of China and the Opening Project of State Key Laboratory of Environmental Adaptability for Industrial Products.

References

- [1] Roose P., Fallais I., Vandermiers C., Olivier M-G., Poelman M.: Radiation curing technology: An attractive technology for metal coating. *Progress in Organic Coatings*, **64**, 163–170 (2009). DOI: [10.1016/j.porgcoat.2008.08.020](https://doi.org/10.1016/j.porgcoat.2008.08.020)
- [2] Masson F., Decker C., Jaworek T., Schwalm R.: UV-radiation curing of waterbased urethane-acrylate coatings. *Progress in Organic Coatings*, **39**, 115–126 (2000). DOI: [10.1016/S0300-9440\(00\)00128-4](https://doi.org/10.1016/S0300-9440(00)00128-4)
- [3] Uhl F. M., Davuluri S. P., Wong S-C., Webster D. C.: Organically modified montmorillonites in UV curable urethane acrylate films. *Polymer*, **45**, 6175–6187 (2004). DOI: [10.1016/j.polymer.2004.07.001](https://doi.org/10.1016/j.polymer.2004.07.001)

- [4] Kim B. K., Ahn B. U., Lee M. H., Lee S. K.: Design and properties of UV cured polyurethane dispersions. *Progress in Organic Coatings*, **55**, 194–200 (2006). DOI: [10.1016/j.porgcoat.2005.09.015](https://doi.org/10.1016/j.porgcoat.2005.09.015)
- [5] Kim H., Urban M. W.: Molecular level chain scission mechanisms of epoxy and urethane polymeric films exposed to UV/H₂O. Multidimensional spectroscopic studies. *Langmuir*, **16**, 5382–5390 (2000). DOI: [10.1021/la990619i](https://doi.org/10.1021/la990619i)
- [6] Kumar V., Bhardwaj Y. K., Goel N. K., Francis S., Dubey K. A., Chaudhari C. V.: Coating characteristics of electron beam cured Bisphenol A diglycidyl ether diacrylate-co-aliphatic urethane diacrylate resins. *Surface and Coatings Technology*, **202**, 5202–5209 (2008). DOI: [10.1016/j.surfcoat.2008.06.047](https://doi.org/10.1016/j.surfcoat.2008.06.047)
- [7] Yeh J-T., Shu Y-C.: Characteristics of the degradation and improvement of the thermal stability of poly(siloxane urethane) copolymers. *Journal of Applied Polymer Science*, **115**, 2616–2628 (2010). DOI: [10.1002/app.29023](https://doi.org/10.1002/app.29023)
- [8] Yen F. S., Lin L. L., Hong J. L.: Hydrogen-bond interactions between urethane-urethane and urethane-ester linkages in a liquid crystalline poly(ester-urethane). *Macromolecules*, **32**, 3068–3079 (1999). DOI: [10.1021/ma9804186](https://doi.org/10.1021/ma9804186)
- [9] Chattopadhyay D. K., Raju K. V. S. N.: Structural engineering of polyurethane coatings for high performance applications. *Progress in Polymer Science*, **32**, 352–418 (2007). DOI: [10.1016/j.progpolymsci.2006.05.003](https://doi.org/10.1016/j.progpolymsci.2006.05.003)
- [10] Lu W. H., Xu W. J., Wu Y. M., Zhou X., Lu Y. B., Xiong Y. Q.: Synthesis of dendritic poly(urethane acrylate) used for UV-curable coatings. *Progress in Organic Coatings*, **56**, 252–255 (2006). DOI: [10.1016/j.porgcoat.2005.10.004](https://doi.org/10.1016/j.porgcoat.2005.10.004)
- [11] Decker C., Zahouily K.: Photodegradation and photooxidation of thermoset and UV-cured acrylate polymers. *Polymer Degradation and Stability*, **64**, 293–304 (1999). DOI: [10.1016/S0141-3910\(98\)00205-5](https://doi.org/10.1016/S0141-3910(98)00205-5)
- [12] Xing W. Y., Hu Y., Song L., Chen X. L., Zhang P., Ni J. X.: Thermal degradation and combustion of a novel UV curable coating containing phosphorus. *Polymer Degradation and Stability*, **94**, 1176–1182 (2009). DOI: [10.1016/j.polymdegradstab.2009.02.014](https://doi.org/10.1016/j.polymdegradstab.2009.02.014)
- [13] Jimenez M., Duquesne S., Bourbigot S.: Intumescent fire protective coating: Toward a better understanding of their mechanism of action. *Thermochimica Acta*, **449**, 16–26 (2006). DOI: [10.1016/j.tca.2006.07.008](https://doi.org/10.1016/j.tca.2006.07.008)
- [14] Gu J-W., Zhang G-C., Dong S-L., Zhang Q-Y., Kong J.: Study on preparation and fire-retardant mechanism analysis of intumescent flame-retardant coatings. *Surface and Coatings Technology*, **201**, 7835–7841 (2007). DOI: [10.1016/j.surfcoat.2007.03.020](https://doi.org/10.1016/j.surfcoat.2007.03.020)
- [15] Chen X. L., Hu Y., Jiao C. M., Song L.: Preparation and thermal properties of a novel flame-retardant coating. *Polymer Degradation and Stability*, **92**, 1141–1150 (2007). DOI: [10.1016/j.polymdegradstab.2007.01.031](https://doi.org/10.1016/j.polymdegradstab.2007.01.031)
- [16] Zhu S. W., Shi W. F.: Thermal degradation of a new flame retardant phosphate methacrylate polymer. *Polymer Degradation and Stability*, **80**, 217–222 (2003). DOI: [10.1016/S0141-3910\(02\)00401-9](https://doi.org/10.1016/S0141-3910(02)00401-9)
- [17] Fang Z. P., Guo F., Tong L. F.: Effect of a novel phosphorous-nitrogen containing intumescent flame retardant on the fire retardancy and the thermal behaviour of poly(butylene terephthalate). *Polymer Degradation and Stability*, **91**, 1295–1299 (2006). DOI: [10.1016/j.polymdegradstab.2005.08.013](https://doi.org/10.1016/j.polymdegradstab.2005.08.013)
- [18] Nguyen C., Kim J.: Thermal stabilities and flame retardancies of nitrogen-phosphorus flame retardants based on bisphosphoramidates. *Polymer Degradation and Stability*, **93**, 1037–1043 (2008). DOI: [10.1016/j.polymdegradstab.2008.03.024](https://doi.org/10.1016/j.polymdegradstab.2008.03.024)
- [19] Lyon R. E., Walters R. N., Stoliarov S. I.: Screening flame retardants for plastics using microscale combustion calorimetry. *Polymer Engineering and Science*, **47**, 1501–1510 (2007). DOI: [10.1002/pen.20871](https://doi.org/10.1002/pen.20871)
- [20] Lyon R. E.: Heat release kinetics. *Fire and Materials*, **24**, 179–186 (2000). DOI: [10.1002/1099-1018\(200007/08\)24:4<179::AID-FAM736>3.0.CO;2-V](https://doi.org/10.1002/1099-1018(200007/08)24:4<179::AID-FAM736>3.0.CO;2-V)
- [21] Lin M-F., Tsen W-C., Shu Y-C., Chung F-S.: Effect of silicon and phosphorus on the degradation of polyurethanes. *Journal of Applied Polymer Science*, **79**, 881–899 (2001). DOI: [10.1002/1097-4628\(20010131\)79:5<881::AID-APP130>3.0.CO;2-I](https://doi.org/10.1002/1097-4628(20010131)79:5<881::AID-APP130>3.0.CO;2-I)
- [22] Chuang F. S., Tsen W. C., Shu Y. C.: The effect of different siloxane chain-extenders on the thermal degradation and stability of segmented polyurethanes. *Polymer Degradation and Stability*, **84**, 69–77 (2004). DOI: [10.1016/j.polymdegradstab.2003.10.002](https://doi.org/10.1016/j.polymdegradstab.2003.10.002)
- [23] Matsunaga K., Tajima M., Yoshida Y.: Thermal degradation of carboxylate-based polyurethane anionomers. *Journal of Applied Polymer Science*, **101**, 573–579 (2006). DOI: [10.1002/app.23574](https://doi.org/10.1002/app.23574)
- [24] Duquesne S., Bras M., Bourbigot S., Delobel R., Camino G., Eling B., Lindsay C., Roels T., Vezin H.: Mechanism of fire retardancy of polyurethanes using ammonium polyphosphate. *Journal of Applied Polymer Science*, **82**, 3262–3274 (2001).
- [25] Wang T-L., Cho Y-L., Kuo P-L.: Flame-retarding materials. II. Synthesis and flame-retarding properties of phosphorus-on-pendent and phosphorus-on-skeleton polyols and the corresponding polyurethanes. *Journal of Applied Polymer Science*, **82**, 343–357 (2001). DOI: [10.1002/app.1858](https://doi.org/10.1002/app.1858)

- [26] Wang G. A., Cheng W. M., Tu Y. L., Wang C. C., Chen C. Y.: Characterizations of a new flame-retardant polymer. *Polymer Degradation and Stability*, **91**, 3344–3353 (2006).
DOI: [10.1016/j.polymdegradstab.2006.06.001](https://doi.org/10.1016/j.polymdegradstab.2006.06.001)
- [27] Hsiue G-H., Shiao S-J., Wei H-F., Kuo W-J., Sha Y-A.: Novel phosphorus-containing dicyclopentadiene-modified phenolic resins for flame-retardancy applications. *Journal of Applied Polymer Science*, **79**, 342–349 (2001).
DOI: [10.1002/1097-4628\(20010110\)79:2<342::AID-APP180>3.0.CO;2-8](https://doi.org/10.1002/1097-4628(20010110)79:2<342::AID-APP180>3.0.CO;2-8)
- [28] Setnescu R., Jipa S., Setnescu T., Kappel W., Kobayashi S., Osawa Z.: IR and X-ray characterization of the ferromagnetic phase of pyrolysed polyacrylonitrile. *Carbon*, **37**, 1–6 (1999).
DOI: [10.1016/S0008-6223\(98\)00168-7](https://doi.org/10.1016/S0008-6223(98)00168-7)
- [29] Bugajny M., Bourbigot S., Bras M., Delobel R.: The origin and nature of flame retardance in ethylene-vinyl acetate copolymers containing hostaflam AP 750. *Polymer International*, **48**, 264–270 (1999).
DOI: [10.1002/\(SICI\)1097-0126\(199904\)48:4<264::AID-PI118>3.0.CO;2-M](https://doi.org/10.1002/(SICI)1097-0126(199904)48:4<264::AID-PI118>3.0.CO;2-M)

Dynamic wettability and contact angles of poly(vinylidene fluoride) nanofiber membranes grafted with acrylic acid

F. L. Huang¹, Q. Q. Wang¹, Q. F. Wei^{1*}, W. D. Gao¹, H. Y. Shou², S. D. Jiang¹

¹Key Laboratory of Eco-Textiles(Jiangnan University), Ministry of Education, 214122 Wuxi, China

²Zhejiang Province New Textile Research & Development Emphasised Laboratory, Zhejiang Textile & Garment Science & Technology Co., Ltd., 310009 Hangzhou, China

Received 18 March 2010; accepted in revised form 20 May 2010

Abstract. Wettability has been recognized as one of the most important properties of fibrous materials for both fundamental and practical applications. In this study, the plasma induced grafting of acrylic acid (AAc) was applied to improve the wettability of the electrospun poly(vinylidene fluoride) (PVDF) nanofiber membranes. The diameter and chemical structure of the modified PVDF nanofibers were characterized by scanning electron microscopy (SEM) and Fourier transform infrared (FTIR). Nitrogen adsorption based on BET (Brunauer, Emmett and Teller) principle was employed to measure the specific surface areas and porosities of the modified nanofiber membranes. The contact angles of the modified membrane were evaluated by drop shape analysis (DSA) and the modified Washburn method. The dependence of contact angles on specific surface area and porosity was also discussed in this paper. Water adsorptions were used to evaluate the dynamic wetting behavior of the grafted membranes by a dynamic adsorption apparatus (CDCA100-F). The experimental results revealed that the wettability of the modified PVDF membrane was significantly affected by both surface and porous contact angles.

Keywords: *polymer membranes, electrospinning, contact angles, poly (vinylidene fluoride)*

1. Introduction

PVDF has been intensively studied due to its excellent bulk properties, such as high electric resistance as well as good thermostability, light weight and good processability [1–3]. These properties have made PVDF increasingly used in various fields such as filtration, air cleaning, and rechargeable batteries. These applications require materials with well-defined properties and functionalities. Nanofibers produced by electrospinning have attracted a great deal of attentions in these applications due to its remarkable properties, such as small fiber diameters, porous structures as well as high surface area [4, 5]. However, their applications are hampered in many cases because of its poor wettability and adhesion property with other materials [6].

In recent years, various techniques have been tried to improve the wettability of PVDF materials, such as plasma treatment, iron irradiation and sputter coating [6, 7]. In these modifications, plasma-induced graft polymerization of vinyl monomers has been found to be an extremely attractive technique for chemically modifying the surfaces of polymeric materials [8]. Although both surface energy and surface roughness are the dominant factors for wettability of materials, surface roughness is the key factor once the components of materials have been selected.

In this study, electrospun PVDF nanofiber membranes were modified by plasma-induced grafting of acrylic acid to improve their wettability. The PVDF membranes with different structures were

*Corresponding author, e-mail: qfwei@jiangnan.edu.cn
© BME-PT

prepared by electrospinning for the investigation into the relationship between dynamic wettability and fibrous structures.

The wettability of a material can be characterized by contact angles. Two types of measurements, drop shape analysis and Washburn method [9], have been widely used to characterize the contact angles. However, due to the complicated surface structures, few literatures have focused on the surface contact angle of nanofiber membrane. And also, the complicated internal geometry in the nanofiber membrane has also been the obstructive factor for the analysis of Washburn contact angle. In this work, the Washburn equation was modified to evaluate the porous contact angles of the grafted PVDF nanofiber membrane, and the effect of porous structures on contact angles was also discussed.

2. Experimental

2.1. Materials

PVDF with average molecular weight (M_n) of $5.5 \cdot 10^5 \text{ g} \cdot \text{mol}^{-1}$ was purchased from Shanghai 3F New Materials Co., Ltd (Shanghai, China). N,N-Dimethyl formamide (DMF), acetone and acrylic acid (AAc) were supplied by Sinopharm Chemical Reagent Co., Ltd (Shanghai, China) and used without further purification.

2.2. Preparation of PVDF nanofibers

PVDF nanofiber membranes with four different fiber diameters were prepared in this study. PVDF was dissolved in a mixture of DMF and acetone (20/80, w/w) to make 15% (wt) solutions for electrospinning.

The apparatus for electrospinning included a plastic syringe, an 18 gauge stainless steel needle, a microinfusion pump (Medical Instrument Co., Zhejiang, China), a high-voltage power supply (Dongwen Co., Tianjing, China), and an aluminum foil as the fiber collector. The ejection rate of the solution was set at 1.0 ml/h, and the distance between the needle tip and the fiber collector was 15.0 cm. Electrospinning was performed at the electrostatic voltages of 8, 12, 16 and 20 kV respectively with the adjustable-voltage power supply. The electrospinning was performed in a fume chamber at the

temperature of 20°C and humidity of 45%. After three hours deposition, all the membranes were collected on the aluminium foil substrate. The membranes were dried in vacuum to remove the solvent. The membranes were then cut at the weight of 5.0 g.

2.3. Plasma-induced grafting of PVDF nanofibers

The process of plasma pretreatment followed by surface grafting with acrylic acid (AAc) on the membrane is described in Figure 1. The nanofiber membrane was treated with an argon plasma which was performed in a HD-1A vertical plasma treatment machine (Changzhou Shitai Co, China). The pretreatment was performed at a pressure of 15 Pa and power of 75 W for 120 s. After being taken out from the reactor, the sample was allowed to stay in air atmosphere for 30 min and then immersed in a solution of acrylic acid (30%, wt). The grafting reaction was carried out by placing ampoules at 60°C temperature in a water bath for 2 h. The samples were, then, washed extensively in deionized water at 60°C in a water bath to remove the poly (acrylic acid) which was not covalently bound to the PVDF surface. The membranes were then dried in an oven at 70°C.

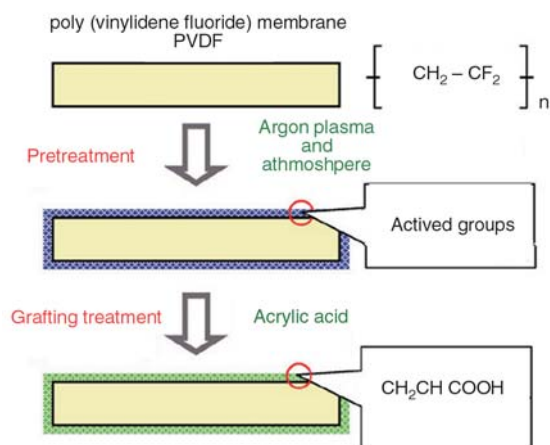


Figure 1. Schematic diagram of pretreatment and grafting on PVDF nanofiber membrane

2.4. SEM and FTIR

The fibrous structures of the nanofibers were examined using a scanning electron microscopy (SEM, JEOL JSM-5610LV, Japan). Before SEM imaging,

the samples were sputtered with a thin layer of gold. The diameters of nanofibers were also measured using the software Photoshop 10.0.

The surface chemistry of the modified PVDF nanofiber membranes was examined by Fourier Transform Infrared (FTIR) (Thermo Electron Corporation). Spectra were recorded in air by use of a FTIR Nexus spectrometer. Approximately 64 scans were co-added to achieve the signal-to-noise ratio shown. The spectral resolution was 4 cm⁻¹.

2.5. Specific surface area and pore structure

The specific surface areas and pore structures of the grafted nanofiber membranes were examined using low temperature (77.38 K) nitrogen adsorption isotherms measured over a wide range of relative pressure from 0.02 to 1. Adsorption measurements were performed on an ASAP2010 volumetric adsorption apparatus. High purity nitrogen (99.9999%) was used in this experiment. Prior to measurement, the samples were degassed at 100°C for 3 h in the degas pot of the adsorption analyzer.

2.6. Contact angles

The surface contact angles were firstly measured on a Drop Shape Analysis System (DSA100) (KRUSS, Germany). Deionized water was dropped onto the sample from a needle on a microsyringe during the test. A picture of the drop was captured after the drop set onto the sample. The contact angles could be calculated by the software through analyzing the shape of the drop. The contact angle θ was an average of 20 measurements.

Washburn method [9] has been recognized as the most effective tool to analyze the contact angle of powder materials. In this study, modified Washburn method was used to characterize the contact angles of porous media. The measurement was performed using a CDCA-100F (a dynamic contact angle apparatus made by the Camtel Ltd. Co., UK). The method for measuring the contact angle relies on the test fluids penetrating the porous sample, which can be expressed by the theory of Washburn (Equation (1)):

$$\frac{l^2}{t} = \frac{\sigma r \cos \theta}{2\eta} \quad (1)$$

Where l , σ , r , θ and η represent rising height, surface tension of liquid, radius of capillary, advancing contact angle and viscosity of liquid, respectively.

For the nanofiber membrane, this equation can be modified such that they are seen as a bundle of capillaries with a mean radius of capillary, r . A modified Washburn equation can be used (Equation (2)):

$$\frac{l^2}{t} = \frac{(cr)\sigma \cos \theta}{2\eta} \quad (2)$$

In this equation, c is a constant to estimate the tortuous path of the capillaries.

The relationship becomes non-linear at higher σ values i.e. the rise height decreases. Once (cr) is determined for a given sample, the advancing angle of liquids with $\cos \theta < 1$. l can be calculated by replacing the rise height of the liquid with the weight gain of the sample. Hence the Equation (2) becomes Equation (3):

$$\frac{W^2}{t} = \frac{[(cr)\omega^2(\pi R^2)]\rho^2\sigma \cos \theta}{2\eta} = \frac{K\rho^2\sigma \cos \theta}{2\eta} \quad (3)$$

Where W , ρ , ω , R , represent weight of penetrating liquid, density of measuring liquid, relative porosity and inner radius of the measuring tube.

For a given sample, i.e. nanofiber membrane in this study, K , the geometric factor was found by conducting a preliminary test on the nanofiber membrane using n-hexane as a totally wetting liquid ($\cos \theta = 1$), which can be characterized by the Equation (4):

$$K = \frac{2W^2\eta}{t\rho^2\sigma} \quad (4)$$

Thus, the Washburn contact angle of nanofiber membrane can be calculated by Equations (3) and (4).

2.7. Dynamic wetting

Dynamic wetting tests were performed on a Camtel CDCA-100F dynamic adsorption apparatus (Camtel, UK). Each sample was cut to a size of 1 cm x 5 cm with sharp scissors. When the specimen was immersed into water, the weight of adsorbed water was detected and recorded. The dynamic water adsorption was plotted as a function of time.

3. Results and discussion

3.1. Diameters of PVDF nanofibers

To investigate the effect of fibrous structures on contact angle and wettability, the nanofibers with various diameters were prepared by adjusting electrospinning voltage. SEM images of the grafted membranes prepared by electrospinning with different voltages are presented in Figure 2. It can be clearly observed from the images that the average diameter of the PVDF nanofibers decreases with increasing applied voltage. The effect of voltage on diameters of nanofibers has been extensively investigated in some literatures [10–12]. The drawing rate of the nanofibers can be enhanced by increasing the electrostatic forces brought by the electrostatic voltage. The average diameters of the grafted PVDF nanofibers electrospun with different static voltages are illustrated in Figure 2f.

3.2. Surface chemistry

Figure 3 shows the infrared spectra for the original PVDF nanofiber membrane, the samples treated with argon plasma and acrylic acid grafting. The spectrum of original PVDF membrane (Figure 3a) exhibits some intensive bands at 1400, 1280, 1076, 835 cm^{-1} , which are assigned to the characteristic vibration of C–H and C–F. Compared to the pris-

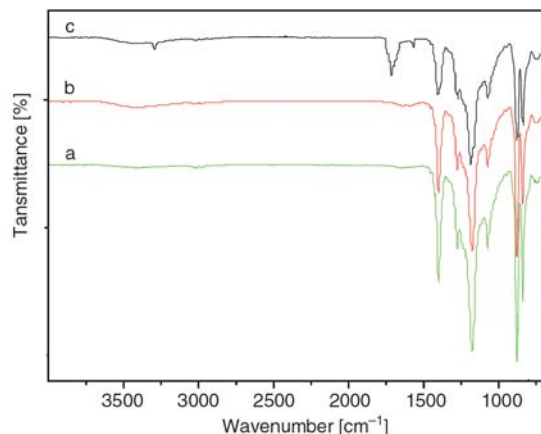


Figure 3. FTIR spectrum of (a) original PVDF membrane, (b) plasma treated PVDF membrane and (c) grafted PVDF membrane

tine PVDF membrane, there is no obvious change on the membrane after plasma treatment as illustrated in Figure 3b. This step only attributes to the formation of activated radicals. For grafted nanofiber membrane, the appearance of representative bands at 3380 cm^{-1} , as shown in Figure 3c, which attests the presence of the –O–H. From the spectra, stretching vibration of O=C–O– at 1727 cm^{-1} is well observed as well as the symmetric stretching vibration of –C=O at 1695 cm^{-1} . It can be concluded from these observations that a layer of acrylic acid is grafted on the PVDF nanofiber membrane. This result can be also ascertained from the

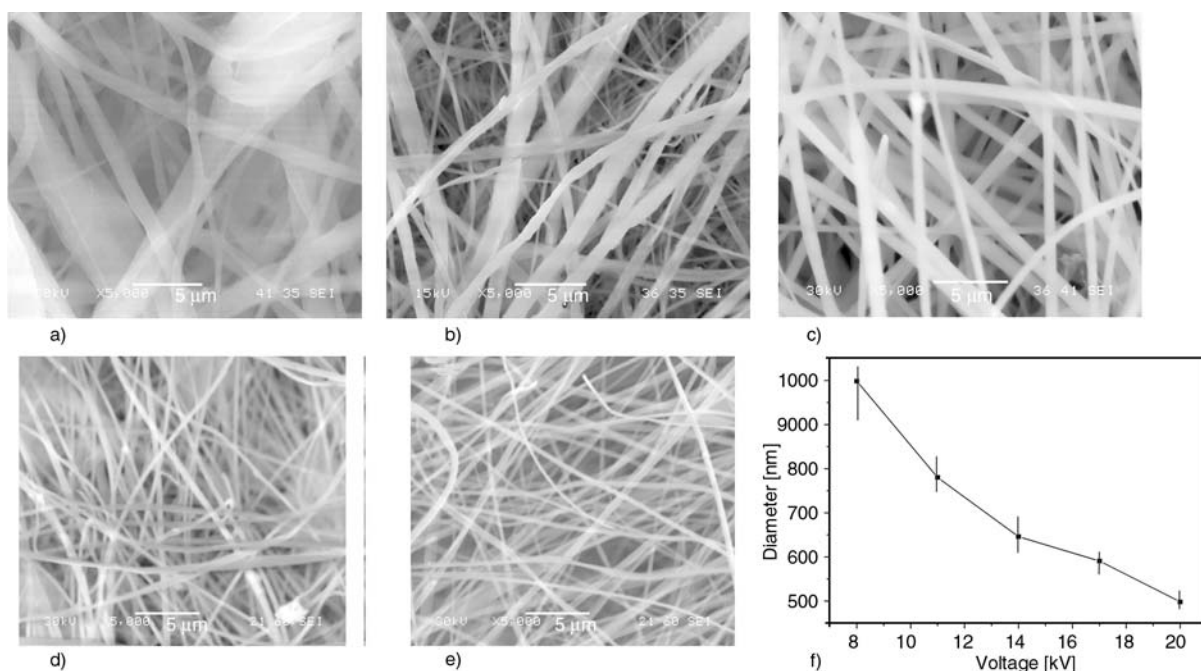


Figure 2. SEM images of PVDF membranes prepared with voltage of (a) 8 kV, (b) 11 kV, (c) 14 kV, (d) 17 kV, (e) 20 kV and (f) curve of diameter with voltage

typical vibration of C–F and C–H from 800–1400 cm^{-1} , which obviously appears weakened on the FTIR spectra of modified membrane.

3.3. Specific surface area and porous structure

It is well known that the difference in fiber size leads to change in the material structures such as specific surface area and pore size distribution. In this study, electrospun voltage was adjusted to control fibrous structures of the modified PVDF membrane. The BET specific surface areas of the nanofiber mats grafted with acrylic acid are summarized in Figure 4. It can be seen from Figure 4 that BET specific surface area has a tendency to increase with reduction of fibre diameter obtained by reducing the voltage. The specific surface area increases from 8 to 24 m^2/g as the diameter reduced from 1000 to 500 nm (and voltage raised from 8 to 22 kV). This phenomenon is attributed to the enhanced stretching effect of the electrostatic forces as the electrostatic voltage increases. Each value of BET surface area is much higher than the traditional fibrous materials, though these values are slightly lower than that of untreated nanofiber membrane. The specific surface area of untreated nanofiber membrane electrospun with the voltage of 22 kV is about 28.4 m^2/g .

A shifting trend in the porosity of the grafted PVDF membrane is also revealed in Figure 4 and the results indicate that the porosity doesn't show a monotone increase in contrast to BET surface area. It is shown that the porosity of the grafted PVDF membrane changes in the range between 25.1 and 59%. As the applied voltage alters from 8 to 14 kV,

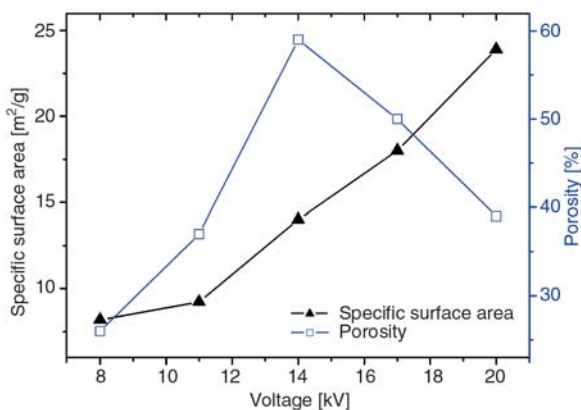


Figure 4. Specific surface area and porosity of PVDF nanofiber membrane

the porosity presents an evident increase and reaches to a top value of 59%. However, the values of the porosity have an opposite trend as the voltage is above 14 kV. The porosity of the PVDF nanofiber membrane decreases from 59% (14 kV) to 38.8% (20 kV). This phenomenon may be attributed to a more compressed assembly of the nanofibers generated by the higher voltage.

3.4. Contact angles

Surface contact angle of the grafted nanofiber membrane is measured using sessile drop observation. Figure 5a shows a water droplet formed on the untreated PVDF nanofiber membrane. The surface contact angle of the nanofiber membrane is 91.2° , in agreement with the strong hydrophobicity of PVDF material to water. The image in Figure 5b shows a significant decrease in the contact angle on the grafted PVDF membrane, which may be ascribed to the grafting of hydrophilic radical, $-\text{COOH}$. However, it is proved from the observations that the surface chemical feature is not the only factor influencing the surface contact angle. The membranes obtained with different electrospinning voltages and grafted under the same conditions present varied contact angles, as illustrated in Figure 6. This observation can be explained by

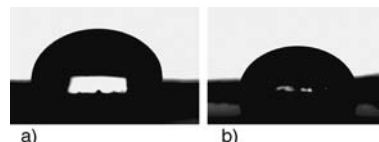


Figure 5. Micrograph of surface contact angle of (a) untreated membrane (b) membrane grafted with acrylic acid

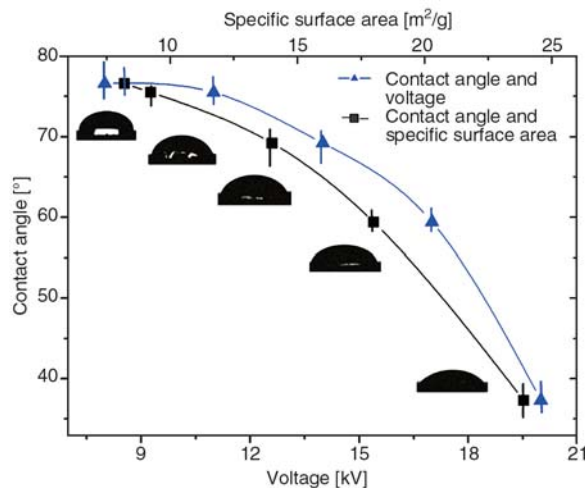


Figure 6. Surface contact angles of the PVDF membrane

the Wenzel equation [13]. This equation indicates that the water contact angle of the surface decreases with increasing surface roughness when the surface is composed of hydrophilic substances. Roughness, however, is so complicated that it is difficult to develop a general method for the roughness measurement. In this study, specific surface area based on BET method is used for roughness characterization (see Equations (5) and (6)):

$$B = \frac{S_r}{m} \tag{5}$$

$$R = \frac{S_r}{S_p} = \frac{mB}{S_p} \tag{6}$$

Where S_r is the real surface area of nanofibrous membrane, S_p is the projected area, B is the specific surface area, and m represents the mass of a membrane.

Then the contact angle of the grafted membrane can be expressed by the Equations (7) and (8):

$$\cos \theta' = R \cos \theta = \frac{mB}{S_p} \cos \theta \tag{7}$$

$$\theta' = \arccos(R \cos \theta) = \arccos\left(\frac{mB}{S_p} \cdot \cos \theta\right) \tag{8}$$

It can be seen from the Equation (8) that the contact angle, θ' of the membrane depends on the ideal contact angle, θ and surface area, and the specific surface area plays an important role in the contact angle of a material. Larger specific surface area, as shown in Figure 6, leads to lower contact angles, fitting the curve of arccosine.

Porous contact angle is an important fact influencing the wetting behavior of fibrous membrane, which can be calculated by a modified Washburn equation as described in Section 2.3. As displayed in Figure 7, the Washburn contact angles of the five grafted membranes were calculated to be 67, 50, 40, 46 and 44°, respectively. The values obtained by this technique show an obvious difference from those obtained by sessile drop tests. The contact angle doesn't show a monotone change with the electrospinning voltage. Interestingly, it is also found from Figure 7 that the Washburn contact angle of the PVDF nanofiber membrane is closely related to its porosity. The membrane with higher porosity shows a lower contact angle. The highest porosity of 59% seems to bring the lowest contact

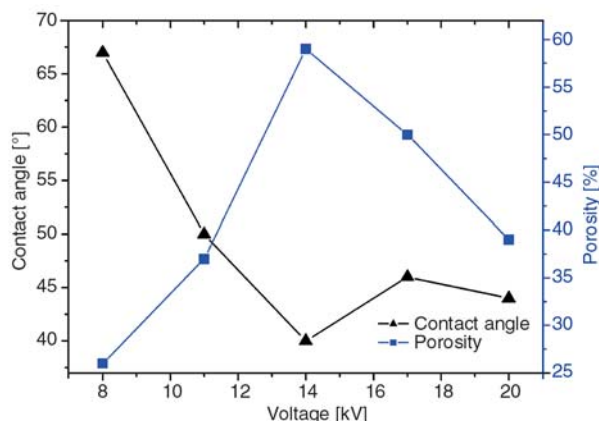


Figure 7. Diagram of the Washburn contact angle and porosity

angle of 40°. This phenomenon can be also analyzed by the modified Washburn Equation (3). However, it should also be noted that the Washburn contact angle of the membrane presents a descendent trend when the electrospinning voltage is over 17 kV, which may be attributed to the effect of other porous factors in the nanofiber membrane, for example, pore size and its distribution.

3.5. Dynamic wetting

The results of the water adsorption tests reveal the dynamic wetting behavior of the PVDF nanofiber membranes. The membrane shows a very low adsorption before the acrylic acid grafting, as shown in Figure 8. When the sample is immersed into water, the effect of buoyancy of water pushes the materials upwards since the surface contact angle is higher than 90°. This observation confirms the hydrophobic behavior of the PVDF nanofiber membrane. It can be seen from Figure 8 that the adsorption curve of the grafted membrane (electro-

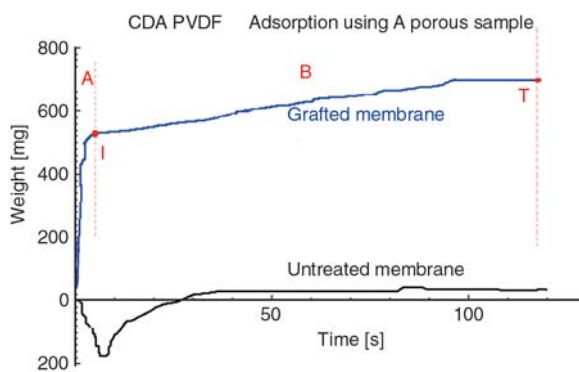


Figure 8. Dynamic water adsorption of PVDF membrane before and after acrylic acid grafting

spun with voltage of 20 kV) displays a contrary evolution to that of the untreated membrane. The acrylic acid grafting considerably improves the water adsorption properties of the PVDF nanofiber membrane due to the lower contact angles.

The effect of the electrospinning voltage on the water wetting behavior can be obviously observed from the dynamic adsorption tests, as illustrated in Figure 9. All five samples electrospun with different voltages were grafted with acrylic acid under the same processing conditions. It can be seen from the image that all the grafted membranes show hydrophilic properties and the amount of water adsorbed is all over 300 mg. Although the adsorption curves show similar trends, they also exhibit varied phenomena as indicated in Figure 9.

It is observed from the adsorption curves that they appear to have two zones, as shown in Figure 9. The first zone, *A* is the initial water adsorption, which occurs over the first few seconds. And a crucial inflexion labeled *I* represents the top value of water adsorption in the first zone. The weight of adsorption water of each sample can be respectively denoted by W_8 , W_{11} , W_{14} , W_{17} , W_{20} , corresponding to voltage of 8, 11, 14, 17 and 20 kV, and the time of reaching to each inflexions is T_8 , T_{11} , T_{14} , T_{17} and T_{20} . These values can be easily obtained from Figure 9, which are expressed by the following orders: $T_8 > T_{11} > T_{14} > T_{17} > T_{20}$ and $W_8 < W_{11} < W_{14} < W_{17} < W_{20}$. During the initial adsorption, it can be found that higher voltage results in a quicker adsorption and a larger amount of water absorbed. Since the water mainly contact with the outmost fibers in the first zone, the surface contact angle may play the essential role in the ini-

tial adsorption. The lower contact angle leads to the quicker adsorption and larger weight of water.

Then, the water is adsorbed into the fibrous webs and transferred through capillary. This could be called transferring zone, *B*, as shown in Figure 9. It can be seen from the image that another important point, *T*, which presents the total water adsorption. It is observed from Figure 9, that the grafted membrane with the electrospinning voltage of 14 kV obtained the largest weight of adsorption. It may be explained by the effect of porous contact angle on the water adsorption. In the transferred zone, lower porous contact angle leads to faster transferring rate and a larger amount of adsorption. And it can also be concluded from the results that surface contact angle determines the initial adsorption, and the porous contact angle influences the capillary adsorption.

4. Conclusions

This study has revealed that the plasma-induced grafting of acrylic acid significantly improved the wetting behaviour of the PVDF nanofiber membrane. PVDF membranes with different surface structures were prepared by electrospinning to investigate the relationship between dynamic wetting behavior and structures. The BET tests have shown that applied voltage obviously altered the specific surface area and porosity, which have been proved to be the key facts influencing the surface and Washburn contact angles. It is observed from the adsorption curves that they appear to have two zones, initial water adsorption and capillary water adsorption. It was also found from the water adsorption measurement that surface contact angle determined the initial adsorption, and the porous contact angle influenced the capillary adsorption.

Acknowledgements

The work was financially supported by the Fundamental Research Funds for the Central Universities of Jiangnan University (No. JUSRP20903), the Program for Key Laboratory of Textile Science & Technology, Ministry of Education, Donghua University, and the Doctoral Program of Higher Education of China (No. 200802951011 and No. 20090093110004).

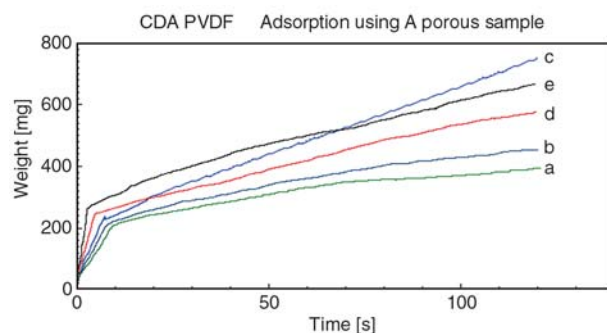


Figure 9. Dynamic water adsorption of the membrane electrospun with (a) 8 kV (b) 11 kV (c) 14 kV (d) 17 kV and (e) 20 kV

References

- [1] Khayet M., Feng C. Y., Khulbe K. C., Matsuura T.: Preparation and characterization of polyvinylidene fluoride hollow fiber membranes for ultrafiltration. *Polymer*, **43**, 3879–3890 (2002).
DOI: [10.1016/S0032-3861\(02\)00237-9](https://doi.org/10.1016/S0032-3861(02)00237-9)
- [2] García-Payo M. C., Essalhi M., Khayet M.: Effects of PVDF-HFP concentration on membrane distillation performance and structural morphology of hollow fiber membranes. *Journal of Membrane Science*, **347**, 209–219 (2010).
DOI: [10.1016/j.memsci.2009.10.026](https://doi.org/10.1016/j.memsci.2009.10.026)
- [3] Kim J-U., Park S-H., Choi H-J., Lee W-K., Lee J-K., Kim M-R.: Effect of electrolyte in electrospun poly(vinylidene fluoride-co-hexafluoropropylene) nanofibers on dye-sensitized solar cells. *Solar Energy Materials and Solar Cells*, **93**, 803–807 (2009).
DOI: [10.1016/j.solmat.2008.09.045](https://doi.org/10.1016/j.solmat.2008.09.045)
- [4] Gao K., Hu X. G., Dai C. S., Yi T. F.: Crystal structures of electrospun PVDF membranes and its separator application for rechargeable lithium metal cells. *Materials Science and Engineering: B*, **131**, 100–115 (2006).
DOI: [10.1016/j.mseb.2006.03.035](https://doi.org/10.1016/j.mseb.2006.03.035)
- [5] Huang Z-M., Zheng Y-Z., Kotaki M., Ramakrishna S.: A review on polymer nanofibers by electrospinning and their applications in nanocomposites. *Composites Science and Technology*, **63**, 2223–2253 (2003).
DOI: [10.1016/S0266-3538\(03\)00178-7](https://doi.org/10.1016/S0266-3538(03)00178-7)
- [6] Hietala S., Skou E., Sundholm F.: Gas permeation properties of radiation grafted and sulfonated poly(vinylidene fluoride) membranes. *Polymer*, **40**, 5567–5573 (1999).
DOI: [10.1016/S0032-3861\(98\)00768-X](https://doi.org/10.1016/S0032-3861(98)00768-X)
- [7] Liu F., Du C-H., Zhu B-K., Xu Y-Y.: Surface immobilization of polymer brushes onto porous poly(vinylidene fluoride) membrane by electron beam to improve the hydrophilicity and fouling resistance. *Polymer*, **48**, 2910–2918 (2007).
DOI: [10.1016/j.polymer.2007.03.033](https://doi.org/10.1016/j.polymer.2007.03.033)
- [8] Lu W-L., Huang C-Y., Roan M-L.: Effect of plasma treatment on the degree of AAm grafting for high-density polyethylene. *Surface and Coatings Technology*, **172**, 251–261 (2003).
DOI: [10.1016/S0257-8972\(03\)00337-2](https://doi.org/10.1016/S0257-8972(03)00337-2)
- [9] Washburn E. W.: Dynamics of capillary flow. *Physical Review*, **17**, 273–283 (1921).
- [10] Helgeson M. E., Wagner N. J.: A correlation for the diameter of electrospun polymer nanofibers. *AIChE Journal*, **53**, 51–55 (2007).
DOI: [10.1002/aic.11056](https://doi.org/10.1002/aic.11056)
- [11] Feng J. J.: Stretching of a straight electrically charged viscoelastic jet. *Journal of non-Newtonian Fluid Mechanics*, **116**, 55–70 (2003).
DOI: [10.1016/S0377-0257\(03\)00173-3](https://doi.org/10.1016/S0377-0257(03)00173-3)
- [12] Spivak A. F., Dzenis Y. A., Reneker D. H.: A model of steady state jet in the electrospinning process. *Mechanics Research Communications*, **27**, 37–42 (2000).
DOI: [10.1016/S0093-6413\(00\)00060-4](https://doi.org/10.1016/S0093-6413(00)00060-4)
- [13] Wenzel R. N.: Resistance of solid surfaces to wetting by water. *Industrial and Engineering Chemistry*, **28**, 988–994 (1936).
DOI: [10.1021/ie50320a024](https://doi.org/10.1021/ie50320a024)

Investigation of correlation between dielectric parameters and nanostructures in aqueous solution grown poly(vinyl alcohol)-montmorillonite clay nanocomposites by dielectric relaxation spectroscopy

R. J. Sengwa*, S. Choudhary

Dielectric Research Laboratory, Department of Physics, J N V University, Jodhpur – 342005 India

Received 27 March 2010; accepted in revised form 23 May 2010

Abstract. Poly(vinyl alcohol) (PVA)-montmorillonite (MMT) clay nanocomposite films up to 10 wt% clay concentration were synthesized by aqueous solution grown technique. The relative complex dielectric function, alternating current electrical conductivity, electric modulus and impedance properties of these organic-inorganic nanocomposites were investigated in the frequency range from 20 Hz to 1 MHz at ambient temperature. The PVA-MMT clay nanocomposite films show a large decrease in the real part and loss of relative dielectric function at 1 wt% MMT clay loading compared to pure PVA film and anomalous behaviour is observed with further increase of clay concentration in PVA matrix. Two dielectric relaxation processes were observed in these nanocomposites; a high frequency relaxation associated with PVA segmental motion and a low frequency relaxation resulting from PVA/dispersed MMT clay interfacial polarization (Maxwell-Wagner relaxation). Dielectric relaxation times corresponding to these processes were determined by fitting dc conductivity corrected complex dielectric function data to the Havriliak-Negami expression. A correlation between change in dielectric relaxation strength, relaxation time and hindrance to the PVA-chain dynamics with the degree of exfoliated structures of dispersed nanoscale MMT clay filler in the PVA matrix were explored. Results confirm the application of dielectric relaxation spectroscopy as a potential tool in the confirmation of nanocomposite formation and their structure characterization.

Keywords: nanocomposites, dielectric spectroscopy, dielectric properties, PVA dynamics, MMT clay

1. Introduction

Synthesis and structural characterization of polymer-clay (organic-inorganic) nanocomposites (PCNs) are of technological interest due to significant improvement in the useful properties of composite materials over those of the pure polymer [1–12]. For the preparation of poly(vinyl alcohol) (PVA)-layered silicate nanocomposite, montmorillonite (MMT) clay is the most commonly used, which has hydrophilic property, and 2:1 phyllosilicate laminar structure. Synthesis of PVA-MMT clay nanocomposites by solution casting technique and their structural characterization have been sub-

ject of several investigations [13–17]. Structural and morphological studies of PVA-MMT clay nanocomposite materials investigated by X-ray diffraction (XRD), Fourier transform infra-red (FTIR) spectroscopy, differential scanning calorimetry (DSC), atomic force microscopy (AFM), transmission electron microscopy (TEM), and scanning electron microscopy (SEM) have established the high degree intercalation and exfoliation behaviour of MMT clay in the PVA matrix, which improves their thermal, mechanical and permeability properties. Due to the transparent nature of PVA-MMT clay films, these nanocomposites have established

*Corresponding author, e-mail: rjsengwa@rediffmail.com

© BME-PT

their potential use in paper coating. Survey of literature exhibits that, the structure-dielectric properties relationship in PVA-MMT clay nanocomposites has not yet been studied in detail, which is needed for their technological and microelectronic applications, and as electrolyte materials in solid-state batteries.

In the present paper, the dielectric relaxation spectroscopic study of aqueous solution grown PVA-MMT clay nanocomposite films up to 10 wt% MMT clay concentration was carried out to characterize the dielectric properties and their correlation with PVA local chain dynamics in view of low dielectric constant materials as passivation layers in modern microelectronic devices. The complex dielectric function, alternating current (ac) electrical conductivity, impedance properties and electric modulus spectra of the PVA-MMT clay nanocomposite films were investigated over the frequency range 20 Hz to 1 MHz. An attempt is made to correlate the values of various dielectric parameters with structural behaviour of these nanocomposite materials to establish the use of dielectric relaxation spectroscopy as diagnostic tool for the development of on-line testing and monitoring of the nanocomposite formation in PCNs materials [18–33].

2. Materials and methods

2.1. Materials

The PVA of average molecular weight $77\,000\text{ g}\cdot\text{mol}^{-1}$ of laboratory grade was obtained from Loba Chemie, Mumbai, India. Polymer grade hydrophilic montmorillonite (MMT) clay (Nanoclay, PGV), a product of Nanocor® was purchased from Sigma-Aldrich. The MMT clay is white in colour, and has 145 meq/100 g cation exchange capacity (CEC), 150–200 aspect ratio, 2.6 g/cc specific gravity, and 9–10 pH value on 5% dispersion. This is the best MMT clay for the preparation of nanocomposites with the PVA matrix recommended by the manufacturer.

2.2. Preparation of PVA-MMT clay nanocomposite by solution-grown technique

For the 0, 1, 2, 3, 4, 5 and 10 wt% MMT clay concentration (weight fraction concentration for a total

3 g of PVA-MMT clay), 0.00, 0.03, 0.06, 0.09, 0.12, 0.15 and 0.30 g amounts of MMT clay powder were colloiddally suspended each in 5 ml double distilled deionized water in separate glass bottles with airtight caps by vigorous stirring with Teflon® coated magnetic stir bar on a magnetic stir plate for 24 hrs at room temperature. The balance weight 3.00, 2.97, 2.94, 2.91, 2.88, 2.85 and 2.70 g of PVA corresponding to the 0 to 10 wt% clay concentration were dissolved each separately in 22 ml double distilled deionized water at 90°C in separate glass bottles. After that, the respective concentration clay colloidal solutions were mixed with the PVA solutions. For proper intercalation and exfoliation of the clay, these mixtures were again stirred vigorously with Teflon® coated magnetic stir bar on a magnetic stir plate each for 24 hrs. PVA-MMT clay nanocomposite films were cast by pouring the PVA-MMT clay hydrocolloidal suspensions of varying clay concentration into 60 mm diameter stainless steel rings directly onto optically smooth glass plates and were left to dry at room temperature for one week. Room dried films of thickness ~0.4 mm were further dried under vacuum for 24 hrs before their dielectric/electric measurements. All the prepared PVA-MMT clay nanocomposite films were found optically clear to the eyes.

2.3. Measurements

Agilent 4284A precision LCR meter and Agilent 16451B solid dielectric test fixture having a four terminals nickel-plated cobalt (an alloy of 17% cobalt + 29% nickel + 54% iron) electrodes of diameter 38 mm, were used for the measurement in the frequency range 20 Hz to 1 MHz. Frequency dependent values of parallel capacitance C_p , parallel resistance R_p and loss tangent $\tan\delta$ (dissipation factor D) with sample, were measured for the determination of dielectric/electrical functions of the PVA-MMT clay nanocomposite films at ambient temperature (30°C). Prior to the sample measurements, the open circuit calibration of the cell was performed to eliminate the effect of stray capacitance. The details of the evaluation of complex dielectric function $\epsilon^*(\omega) = \epsilon' - j\epsilon''$, complex alternating current (ac) electrical conductivity $\sigma^*(\omega) = \sigma' + j\sigma''$, complex electric modulus $M^*(\omega) = M' + jM''$ and complex impedance $Z^*(\omega) = Z' - jZ''$

of the solid PCNs films are described by us elsewhere [29–31, 34].

3. Results and discussion

3.1. Complex dielectric function

Figure 1a shows that the real part ϵ' of the complex dielectric function of PVA-MMT clay nanocomposites decreases with the increase in frequency of applied alternating electric field from 20 Hz to 1 MHz, which confirms the dielectric dispersion in these materials. The ϵ' values of the nanocomposite films are found to be lower than that of the pure PVA film and have anomalous variation with increase of MMT clay concentration. These observations reveal that the intercalated and exfoliated MMT clay structures in PVA matrix change dramatically with the increase of MMT clay concentration in aqueous solution grown PVA-MMT clay nanocomposite films. Such anomalous variation was also observed in ϵ' values with the increase of MMT clay concentration in PVA-MMT clay hydro-

colloids over the same frequency region [23]. This behaviour is not surprising, because in aqueous solutions the flexible PVA chain and dispersed clay exist with a variety of hydrogen bonded structures. Recently, Wang *et al.* [20, 21] investigated the dielectric properties of solution intercalated polystyrene-MMT clay and poly(methyl methacrylate)-MMT clay nanocomposite films within the frequencies of 100 Hz–1 MHz and found that loading of 1 wt% MMT clay significantly reduces the ϵ' values as compared to the pure polymer film, which is mainly due to reduction in the number of aligned dipolar groups in the presence of randomly distributed exfoliated clay nanoplatelets in the polymer matrix.

In PVA-MMT clay nanocomposites, the intercalation of PVA in clay galleries and exfoliation of MMT clay nanoplatelets occur simultaneously [13–17]. The XRD, TEM and DSC studies established that in aqueous solution grown PVA-MMT clay nanocomposites up to 10 wt% MMT clay loading have well dispersed MMT nanoplatelets throughout the PVA matrix, i.e., nanocomposites formed are mostly exfoliated hybrids [14]. The exfoliation of layers is attributed to the water casting method used, since the water suspended layers become kinetically trapped by the polymer and cannot re-aggregate. Further, the formation of the hydrogen bonds between the PVA vinyl alcohol group and silicate oxygen force the PVA chains to create long adsorbed trains due to the atomically smooth dispersed MMT surfaces. The large reduction in ϵ' value at 1 wt% MMT clay concentration in PVA-MMT clay nanocomposites also suggests that the amount of exfoliated structures is very high as compared to that of the PVA intercalated clay structures [14, 15], which is the common characteristics of solution grown PCNs at very low clay concentration [18–34].

The loss part ϵ'' spectra of complex dielectric function (Figure 1b) reflects the presence of two relaxation processes in the PVA-MMT clay nanocomposite films over the frequency range 20 Hz–1 MHz, which can be seen in their complex plane plots (ϵ'' vs. ϵ') (Figure 2). The frequency values of the experimental data points increases on going from right to left side on these plane plots. The higher frequency arc in Figure 2 is corresponding to the PVA local chain motion, whereas the lower frequency arc represents the contribution of direct

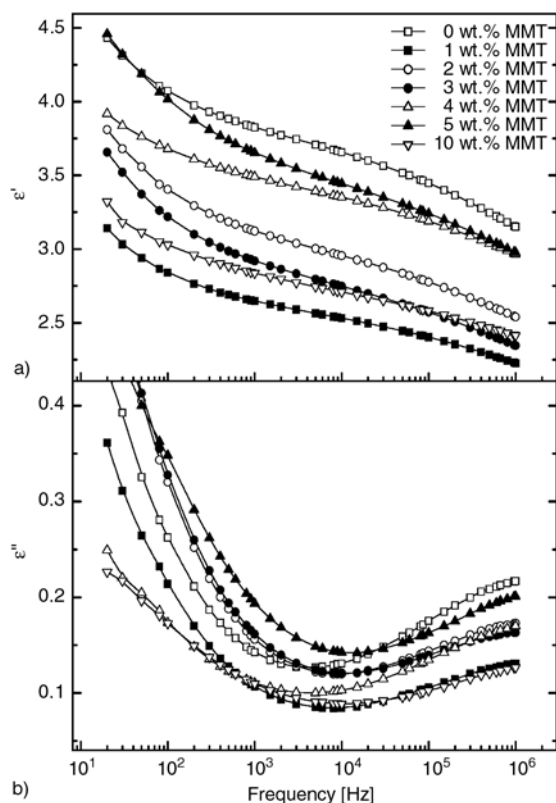


Figure 1. Frequency dependent real part ϵ' and loss ϵ'' of complex dielectric function of solution grown PVA-MMT clay nanocomposite films of varying MMT clay concentration [wt%]. The solid lines are smooth joining of the experimental data points, as guides for the eyes.

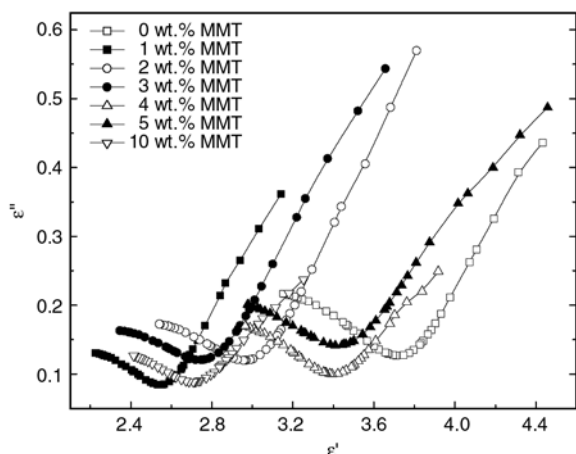


Figure 2. Complex plane plots (ϵ'' vs. ϵ') of solution grown PVA-MMT clay nanocomposite films of varying MMT clay concentration [wt%]

current (dc) conductivity and Maxwell-Wagner (MW) interfacial polarization relaxation process. To explore the dispersed MMT clay nanoplatelets structures and their effects on the PVA molecular local chain dynamics, the higher frequency dielectric data (above 10^4 Hz) were fitted by the Havriliak-Negami (HN) expression [35]. The fit parameters namely limiting real part of dielectric function ϵ_s at lower frequencies and ϵ_∞ at higher frequencies, the dielectric relaxation strength $\Delta\epsilon = \epsilon_s - \epsilon_\infty$, the mean relaxation time τ , and the symmetric and asymmetric broadening parameters α and β , respectively, are recorded in Table 1 and also plotted in Figure 3.

The static dielectric constant ϵ_s (limiting lower frequency ϵ' value) of the 1 wt% MMT clay loaded PVA-MMT clay nanocomposite film decreases nearly by 1 as compared to that of the pure PVA film (Figure 3a and Table 1). The decrease in ϵ_s value confirms the formation of PVA-MMT clay nanocomposites with large amount of exfoliated MMT clay structures in the PVA matrix, as revealed by the dielectric studies of different PCNs materials [1, 2, 18–24, 33, 34]. The $\epsilon_s \sim 2.4$ at the

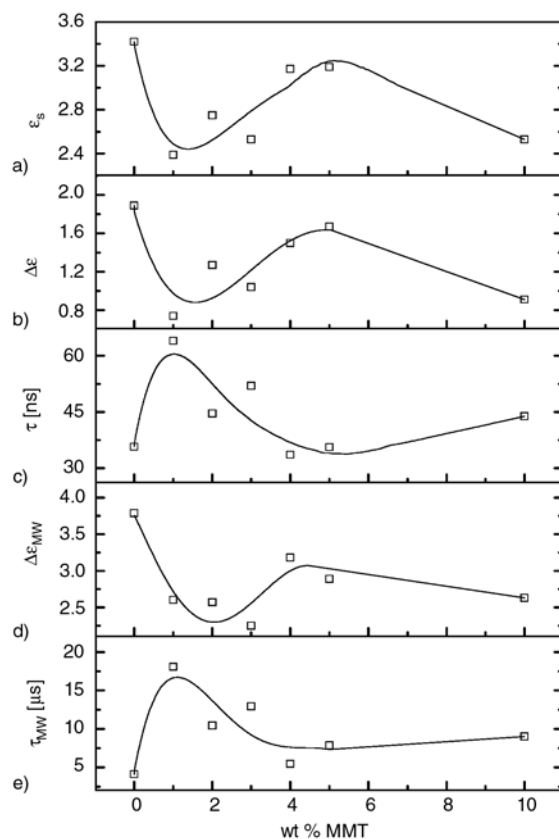


Figure 3. MMT clay concentration [wt%] dependent static dielectric constant ϵ_s , dielectric relaxation strength $\Delta\epsilon$ and mean relaxation time τ of PVA molecular polarization dispersion and, dielectric relaxation strength $\Delta\epsilon_{MW}$ and relaxation time τ_{MW} of MW interfacial polarization process of solution grown PVA-MMT clay nanocomposite films. The solid lines are B-spline fit of the experimental data points, as guides for the eyes.

1 wt% MMT clay concentration in PVA-MMT clay nanocomposite suggests its possible use as low dielectric constant material of improved thermal and mechanical properties in microelectronic devices [1, 2]. At 2 and 3 wt% MMT clay concentration, the ϵ_s values of these nanocomposites are found to be close to that of the 1 wt% MMT clay loaded nanocomposite film, which suggest that the degree of exfoliated MMT clay structures remains

Table 1. Dielectric parameters of PVA–MMT clay nanocomposites of varying MMT clay concentration [wt%]

MMT clay [wt%]	PVA molecular polarization process dielectric parameters					MW interfacial polarization process dielectric parameters					$\sigma_{dc} \cdot 10^{11}$ [S/m]	s
	ϵ_s	$\Delta\epsilon$	τ [ns]	α	β	ϵ_{sMW}	$\Delta\epsilon_{MW}$	τ_{MW} [μ s]	α_{MW}	β_{MW}		
0	3.42	1.89	35.7	0.92	0.78	3.97	3.79	4.1	0.97	0.78	1.68	0.30
1	2.39	0.74	63.9	0.90	0.76	2.82	2.60	18.1	0.97	0.82	1.34	0.30
2	2.75	1.27	44.6	0.91	0.78	3.30	2.57	10.4	0.62	0.76	2.79	0.35
3	2.53	1.04	52.0	0.91	0.80	3.11	2.25	13.0	0.95	0.74	2.28	0.32
4	3.17	1.50	33.5	0.94	0.78	3.60	3.18	5.5	0.98	0.83	0.63	0.22
5	3.19	1.67	35.6	0.93	0.81	3.85	2.89	7.9	0.95	0.72	1.36	0.23
10	2.53	0.91	43.8	0.90	0.75	2.97	2.63	9.0	0.98	0.82	0.51	0.19

nearly the same up to 3 wt% MMT clay loading in PVA matrix. At 4 and 5 wt% MMT clay concentration, the ϵ_s values are found to be slightly less than that of the pure PVA film, which reveals that exfoliated MMT clay structures at these concentrations still dominate over the PVA intercalated clay structures. This finding confirms that at 4 to 5 wt% MMT clay loading in PVA matrix brings critical changes in its mechanical and thermal behaviour without affecting the dielectric constant. At 10 wt% MMT clay concentration the exfoliated structures again increase as compared to the intercalated structures of the MMT clay and their ratio is nearly equal to the 1 to 3 wt% MMT clay concentrations, because the ϵ_s at 10 wt% MMT clay concentration is of the order of 1 to 3 wt% MMT clay loaded nanocomposites. Recently, Pluta *et al.* [27] also confirmed that in polylactide/MMT nanocomposites, large exfoliated nanostructures are formed up to the 3 wt% MMT clay loading due to combined interactions of MMT surfactant with polymer chains, whereas at the 10 wt% MMT clay loading, mixed intercalated and exfoliated nanostructures are formed, which is in agreement with the nanostructures discussed in PVA-MMT clay nanocomposites. Figure 3b also shows that the MMT clay concentration dependent values of dielectric relaxation strength $\Delta\epsilon$ of these nanocomposites vary according to the variation in their ϵ_s values.

The MMT clay concentration dependent mean relaxation time τ of PVA-MMT clay nanocomposites (Table 1 and Figure 3c) confirms that the PVA local chain dynamics is governed by the amount of exfoliated structures of the MMT clay nanoplatelets in the PVA matrix. As discussed above by considering their ϵ_s values, the exfoliated clay structures dominates at the 1 wt% clay loading, which is also favoured by the large increase in τ value at this concentration as compared to that of the pure PVA. The silanol (Si–O) groups of exfoliated clay structures have large range H-bonded interactions with –OH groups of PVA chain, which results in the adsorption of PVA on exfoliated clay surfaces and hence produces large hindrance to its local chain dynamics, thus enhancing the corresponding relaxation time. Kanapitsas *et al.* [18] also observed that for the PCNs, when ϵ' decreases the overall mobility of the polymer chain decreases, as compared to the pure polymer matrix. The decrease in polymer chain segmental mobility relaxation time in nano-

composite provides an explanation for the increased thermal and mechanical stability in the PCNs. Davis *et al.* [24], Kim *et al.* [28], and Sengwa *et al.* [34] also concluded that the increase of τ value represents an increase in clay exfoliation in the PCNs. At varying MMT clay concentrations, good resemblance is observed between the change in the ϵ_s and τ values (Figure 3). The MMT clay concentration at which ϵ_s decreases, τ increases and vice versa is in good agreement with the above discussed correlation between the ϵ_s values and the amount of exfoliated clay structures in the solution grown PVA-MMT clay nanocomposites.

Recently, Bandi and Schiraldi [17] have investigated the glass transition temperature T_g of solution intercalated PVA-MMT clay films as a function of clay size, concentration and dispersion in the PVA matrix. They observed that T_g exhibits a maximum value at 1 wt% concentration of MMT clay and for higher concentration its value decreases anomalously. Further, they explained that at 1 wt% MMT clay concentration, there is the existence of large amount of exfoliated MMT clay nanoplatelets with greater interfacial area, which favours the coupling of PVA chains to the clay surfaces through the adsorption and hydrogen bonding, and simultaneously strengthen the disordered interfaces leading to an increase of the T_g value and the reduce of PVA chain dynamics. The present dielectric study also confirms that a large reduction of the ϵ_s and also the increase of τ value at 1 wt% MMT clay loading results in the formation of large range crosslinked hydrogen bonded structures between exfoliated MMT clay sheets and the randomly coiled and flexible PVA chains, which reduces the net dielectric polarization and increases the hindrance to the PVA local chain dynamics. Wang *et al.* [20] also concluded that a large amount of exfoliated MMT clay structures in PCNs enhances the T_g value and simultaneously reduces the ϵ_s value. The increase in τ value is also related to the increased amount of layered silicate surface area as a result of the increased degree of exfoliation [24, 28]. Above 1 wt% MMT clay loading both the interfacial area and intercalation are enhanced and more PVA chains are confined between the MMT clay sheets. Under confinement the PVA molecules inside the MMT clay galleries are aligned mechanically, resulting from fewer entanglements and bringing enhanced relaxation dynamics within the

composite and reduces its T_g values [17]. The anomalous decrease in τ values (Figure 3c) with the increase in MMT clay loading above 1 wt% are in good agreement with the structural properties of solution intercalated PVA-MMT clay films as explored from their T_g values [17].

The SEM, TEM, FTIR and XRD study of these nanocomposites established that the exfoliated structures in PVA matrix have mixed nanomorphology [16]. Individual silicate layers, along with two, three and four layer stacks (tactoids) exfoliate in the PVA matrix in addition to some large intercalated tactoids. Further, crystalline morphology of pure PVA approaches to amorphous state as the MMT clay concentration increases in PVA matrix. The anomalous decrease in the τ value of nanocomposites above 1 wt% clay loading (Figure 3c) suggests that the mixed nanomorphology of the exfoliated clay tactoids randomly changes with the increase in MMT clay concentration in the aqueous solution grown PVA-MMT clay nanocomposite films, since the water suspended silicate layers becomes kinetically trapped by the randomly coiled and flexible PVA chains. The atomic force microscopy (AFM) of these nanocomposites also revealed that the PVA has a tendency to cover completely the tactoids, which is driven by strong specific interactions between the hydroxyl groups of PVA monomer units and the silanol groups of silicates and causes a strong wetting of PVA on the delaminated clay surfaces [15].

Table 1 shows that the values of PVA local chain relaxation process shape parameters α and β describing the broadening of the relaxation peak that varies anomalously with increase of MMT clay concentration in the PVA-MMT clay nanocomposites. The α and β values of these nanocomposites are found in the ranges 0.90–0.94 and 0.76–0.82, respectively, which confirms that there is an asymmetric broadening of the relaxation peak corresponding to PVA dynamics.

At frequencies below 10^4 Hz the direct current conductivity contribution in the ϵ'' spectra corresponding to low frequency dispersion was fitted with the power law relation $\epsilon'' = \sigma_{dc}/\epsilon_0\omega^s$, where σ_{dc} is the dc conductivity and s is an exponent fitting parameter. For ohmic contacts and no MW polarization, $s = 1$ holds. In the most practical cases $0 < s \leq 1$ is obtained [25], which confirms the contribution of MW interfacial polarization. The dc

conductivity corrected low frequency ϵ'' data were also fitted to HN expression [35] for the evaluation of MW interfacial relaxation time, τ_{MW} and the corresponding dielectric relaxation strength, $\Delta\epsilon_{MW}$. The observed values of σ_{dc} and s along with the dielectric parameters of MW interfacial polarization relaxation process (ϵ_{sMW} , $\Delta\epsilon_{MW}$, τ_{MW} , α_{MW} and β_{MW}) evaluated from the HN expression of the PVA-MMT clay nanocomposites are recorded in Table 1 with varying wt% MMT clay concentration. The values of $\Delta\epsilon_{MW}$ and τ_{MW} of these nanocomposites are also plotted against wt% MMT clay in Figures 3d and 3e, respectively. Table 1 shows that the σ_{dc} values of PVA-MMT clay nanocomposites vary anomalously within one order of magnitude with the increase in MMT clay concentration. The σ_{dc} value of the pure PVA film was found to be in good agreement with the earlier reported value [36]. The values of exponent parameter s are found less than unity (Table 1), which confirms the contribution of MW polarization with dc conduction in lower frequency dielectric dispersion of these nanocomposites. In the MW phenomena, the free charges build up during the electromigration at the interfacing boundaries of different dielectric constants or conductivities components of the composite materials, which results the formation of nanocapacitors in the composite dielectric material at low frequency alternating current electric field [18]. At sufficiently high frequencies, such short-range movements of free charges can not follow the fast changes developed in the applied ac electric field and thus only molecular polarization occurs. In the investigated PVA-MMT clay nanocomposites, at ambient temperature, the MW phenomena contributed in dielectric properties up to 10^4 Hz and above that the dielectric dispersion is due to the PVA molecular polarization. Further, it is found that the s values vary in the same trend of σ_{dc} values with increase of MMT clay concentration in the PVA-MMT clay nanocomposites (Table 1).

In PVA-MMT clay nanocomposites, the interface between non-intercalated galleries of layered silicate (tactoids) and PVA gives rise to the formation of large dipoles, enhancing the electric inertia of interfacial relaxation phenomena, leading to slower motion or greater relaxation time. On the other hand, the interface between PVA and intercalated layered silicates results in formation of relatively smaller dipoles allowing faster motion. Recently,

Noda *et al.* [19] and Bur *et al.* [22] analyzed the MW interfacial relaxation to correlate it with the clay dispersion and the amount of exfoliation in the PCNs materials for on-line process monitoring and off-line measurements. As exfoliation proceeds, nanosize silicate flakes present an ever expanding polymer/silicate interface area that increases the internal capacitance of the composite where the moving charge can accumulate. Silicate flakes act as the nanocapacitors in a sea of dielectric polymer, and as the capacitance increases with exfoliation the characteristic frequency of the MW relaxation decreases and the relaxation time increases. The MW relaxation time τ_{MW} of a nanocomposite is given by the relation $\tau_{MW} = RC$, where R is the resistance of the polymer matrix and C is the capacitance of the dispersed silicate platelets in the matrix [19]. During exfoliation of silicate platelets the value of R remains constant and C changes. Therefore, the RC time constant (τ_{MW}) is controlled solely by the capacitance of the silicate in the aggregate, intercalated, or exfoliated state or any combination thereof.

Figure 3e shows that the MMT clay concentration dependent τ_{MW} values are higher than that of the pure PVA film, which is in good agreement with the formation of large exfoliated clay structures in these nanocomposites, as discussed above on the basis of the comparative change in their ϵ_s and τ values. The MW relaxation process in pure PVA film occurs due to its semicrystalline behaviour. Further, the variation in τ_{MW} values with increase of MMT clay concentration is found to be in good agreement with the trend in the variation of τ values, which reveals that in the PCNs materials the polymer local chain motion relaxation time and MW interfacial polarization relaxation time are coupled processes and provide the same information regarding the nanostructures formation. The τ_{MW} values of these nanocomposites are found to be three to four orders of magnitude higher than that of their τ values. Further, Table 1 and Figure 3d shows that the values of $\Delta\epsilon_{MW}$ are significantly greater than that of the $\Delta\epsilon$ values but the shape parameters values of both the processes vary in the same range with the increase of MMT clay concentration in the investigated nanocomposite films.

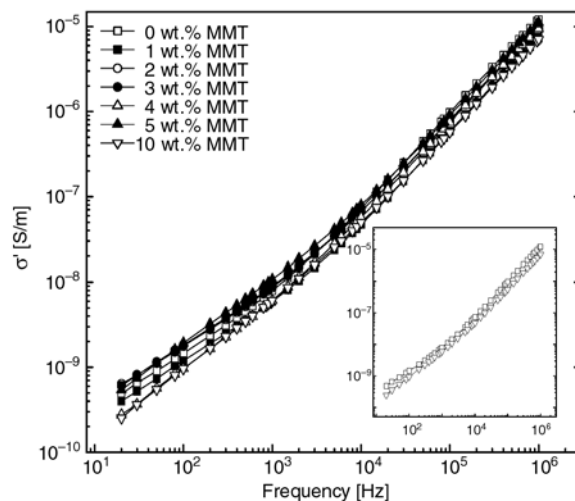


Figure 4. Frequency dependent real part of ac conductivity σ' of solution grown PVA-MMT clay nanocomposite films of varying MMT clay concentration [wt%]. Inset shows the σ' spectra of pure PVA film and the 10 wt% MMT clay concentration PVA-MMT clay nanocomposite film.

3.2. AC conductivity

The real part of ac conductivity σ' of PVA-MMT clay nanocomposite films increases with the increase in frequency and shows an anomalous variation with the increase of MMT clay concentration (Figure 4). The turn in slope of frequency dependent σ' values around 10^4 Hz also reflect the presence of two dispersion processes in lower frequency and upper frequency regions of the experimental frequency range, which are corresponding to the MW interfacial polarization and the PVA molecular polarization processes, respectively, as discussed above.

3.3. Electric modulus spectra

Interpretation of relaxation phenomena via electric modulus formalism offers some advantages upon permittivity and conductivity relaxation treatments since large variation in the ϵ' and ϵ'' values at low frequencies and high temperature are minimized [23, 26, 29–31, 37]. Further, difficulties occurring in the analysis of dielectric spectra from the electrode nature (electrode material), the electrode-specimen electrical contact and the injection of space charges and absorbed impurities can be neg-

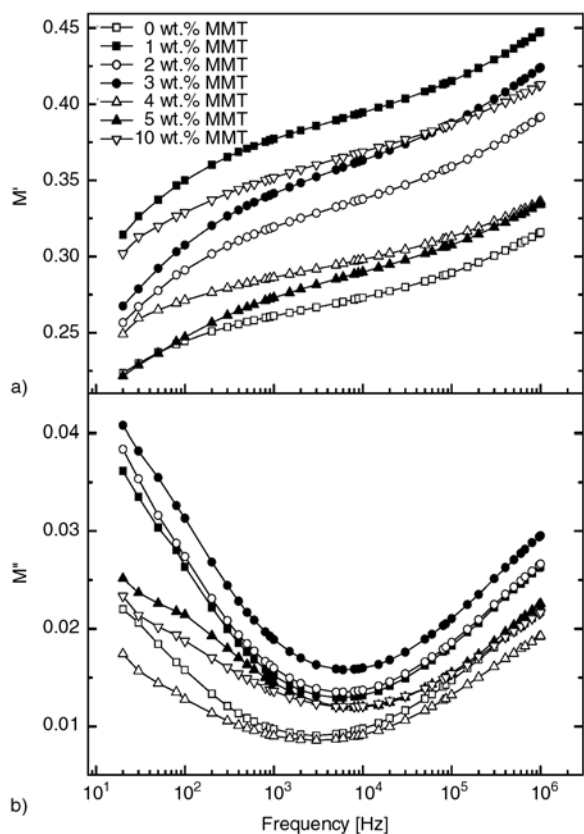


Figure 5. Frequency dependent real part M' and loss M'' of complex electric modulus of solution grown PVA-MMT clay nanocomposite films of varying MMT clay concentration [wt%]. The solid lines are smooth joining of the experimental data points, as guides for the eyes.

lected in the electric modulus spectra. It is observed that the real part of electric modulus M' of PVA-MMT clay nanocomposite films increases with the increase of frequency at lower frequencies of the M' spectra (Figure 5a), which confirms that the measured dielectric/electrical properties are free from the contribution of EP effect. Generally, the dielectric materials, having the contribution of EP effect in their measured dielectric properties, show a plateau at lower frequencies and an abrupt increase in M' spectra at higher frequencies [26, 29–31, 36, 37]. The M'' dispersion spectra (Figure 5b) of the investigated PVA-MMT clay films also confirms the presence of two relaxation processes in these nanocomposite materials in the experimental frequency range. Figure 6 shows the master-curve representation of ϵ'' , M'' and σ' values of the 1 wt% MMT clay concentration PVA-MMT clay film. The consistency in the dispersion spectra of different formalisms confirms the presence of two relaxation processes in the same frequency

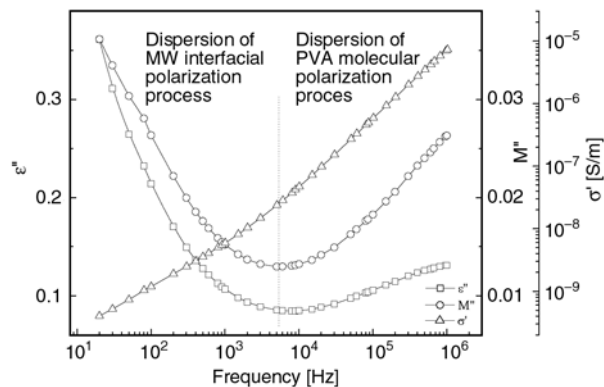


Figure 6. Frequency dependent loss of dielectric function ϵ'' , loss of electric modulus M'' and real part of ac conductivity σ' of solution grown PVA-MMT clay nanocomposite films of the 1 wt% MMT clay concentration. Vertical dotted line shows the turning point in the spectra, which separates two relaxation processes.

range and their suitability in the analysis of nanostructure formation and dynamical behaviour in the PVA-MMT clay nanocomposite materials.

3.4. Impedance spectra

Complex impedance spectroscopy is commonly used to separate the electrode polarization (EP) effect and bulk material properties, which is distinguished by the appearance of two different arcs in the complex impedance plane plots (Z'' vs. Z') [12, 37, 38–40]. The EP phenomena occur due to formation of electric double layer (EDL) capacitances by the free charges that build up at the interface between the dielectric material and electrode surfaces in plane geometry. This is reflected by the large increase of the complex dielectric function with decreasing frequency in the lower frequency region of the dielectric spectra and an additional arc in the complex impedance plane plots. Figure 7 shows that the Z'' versus Z' plots of PVA-MMT clay nanocomposites have only one arc over the entire experimental frequency range, which is corresponding to the properties of bulk material. The single arc plots confirm that in the frequency range 20 Hz to 1 MHz, the PVA-MMT clay nanocomposites have good electrical contact with nickel-plated cobal electrodes and there is no formation of EDL capacitances. Further, the large values of imaginary part Z'' as compared to real part Z' of the complex impedance confirm a highly capacitive behaviour of these films [34, 40].

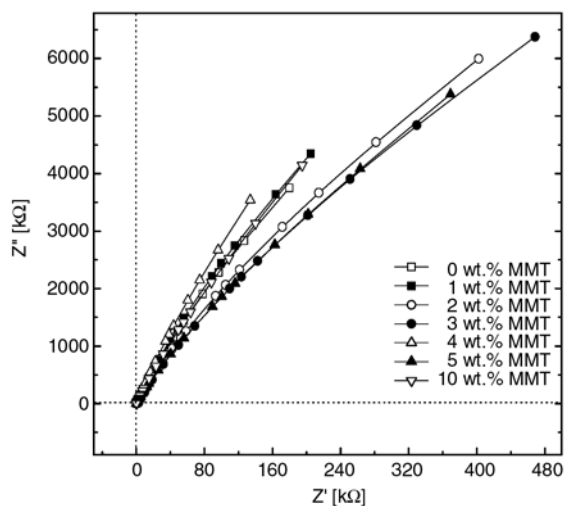


Figure 7. Complex impedance plane plots (Z'' vs. Z') of solution grown PVA-MMT clay nanocomposite films of varying MMT clay concentration [wt%]

4. Conclusions

Earlier studies on the aqueous solution grown PVA-MMT clay nanocomposites materials have established their large enhancement of the Young's modulus, a very moderate decrease of toughness, improved thermal degradation properties, decrease of water permeability, and high melting point at a small amount of MMT clay loading in the PVA matrix and these are also optically clear to eyes [14–16]. In addition to these, the present dielectric relaxation spectroscopy study of these nanocomposite materials confirmed the significant decrease in real part and loss of dielectric function at the 1 wt% MMT clay loading as compared to that of the pure PVA film, which is owing to the formation of a large amount of exfoliated MMT clay nanostructures in the PVA matrix. The anomalous variation in the static dielectric constant values of different processes with the increase of MMT clay in these nanocomposites has good resemblance with the variation in their glass transition temperature [17]. The ϵ'' and M'' spectra of these PCN films confirm the two relaxation processes in the frequency range 20 Hz to 1 MHz. The detailed dielectric study revealed that the static dielectric constant value can be tuned in the magnitude of nearly 1 by loading the 1 wt% MMT clay in PVA matrix for their use as low dielectric constant materials in microelectronic technology and also as electrolytes in solid-state batteries with improved thermal and

mechanical properties. The impedance spectra confirm that in the experimental frequency range there is no contribution of electrode polarization process, but Maxwell-Wagner polarization process and dc electrical conductivity contributed to the lower frequency dielectric dispersion. A strong correlation is observed between the change in static dielectric constant, dielectric relaxation strength and relaxation times of the PVA local chain dynamics and MW interfacial polarization relaxation with the degree of exfoliated clay structures in the PVA matrix. Results suggest that the dielectric relaxation spectroscopy can be applied for the development of testing and monitoring technique in the area of nanocomposite formation, specially confirmation of the amount of exfoliated nanoscale MMT clay platelets in the polymer matrix and their hindrance to the polymer local chain dynamics. At low amount of MMT clay loading the high degree of exfoliated MMT clay structures in polymer matrix significantly reduces the dielectric constant due to the decrease in the number of aligned dipolar groups and simultaneously increases the relaxation time of the polymer local chain motion because of the formation of large range hydrogen bond interactions between exfoliated nanoplatelets of MMT clay and hydroxyl groups of PVA monomer units. The exfoliated MMT clay structures also increase the capacity of PVA/MMT clay interfacial nanocapacitors and enhances the MW interfacial relaxation time, which are responsible for the enhancement in their mechanical and thermal properties.

Acknowledgements

Authors are grateful to the Department of Science and Technology, New Delhi for providing the experimental facilities through project No. SR/S2/CMP-09/2002. One of the authors SC is thankful to the University Grants Commission, New Delhi for the award of RFSMS fellowship.

References

- [1] Alexandre M., Dubois P.: Polymer-layered silicate nanocomposites: Preparation, properties and uses of a new class of materials. *Materials Science and Engineering R: Reports*, **28**, 1–63 (2000). DOI: [10.1016/S0927-796X\(00\)00012-7](https://doi.org/10.1016/S0927-796X(00)00012-7)

- [2] Tanaka T., Montanari G. C., Mülhaupt R.: Polymer nanocomposites as dielectrics and electrical insulation—perspectives for processing technologies, material characterization and future applications. *IEEE Transactions on Dielectrics and Electrical Insulation*, **11**, 763–784 (2004).
DOI: [10.1109/TDEI.2004.1349782](https://doi.org/10.1109/TDEI.2004.1349782)
- [3] Darder M., Colilla M., Ruiz-Hitzky E.: Chitosan-clay nanocomposites: Application as electrochemical sensors. *Applied Clay Science*, **28**, 199–208 (2005).
DOI: [10.1016/j.clay.2004.02.009](https://doi.org/10.1016/j.clay.2004.02.009)
- [4] Ray S. S., Bousmina M.: Biodegradable polymers and their layered silicate nanocomposites: In greening the 21st century materials world. *Progress in Materials Science*, **50**, 962–1079 (2005).
DOI: [10.1016/j.pmatsci.2005.05.002](https://doi.org/10.1016/j.pmatsci.2005.05.002)
- [5] Pavlidou S., Papaspyrides C. D.: A review on polymer-layered silicate nanocomposites. *Progress in Polymer Science*, **33**, 1119–1198 (2008).
DOI: [10.1016/j.progpolymsci.2008.07.008](https://doi.org/10.1016/j.progpolymsci.2008.07.008)
- [6] Auad M. L., Nutt S. R., Pettarin V., Frontini P. M.: Synthesis and properties of epoxy-phenolic clay nanocomposites. *Express Polymer Letters*, **1**, 629–639 (2007).
DOI: [10.3144/expresspolymlett.2007.86](https://doi.org/10.3144/expresspolymlett.2007.86)
- [7] Pannirselvam M., Genovese A., Jollands M. C., Bhatnagar S. N., Shanks R. A.: Oxygen barrier property of polypropylene-polyether treated clay nanocomposite. *Express Polymer Letters*, **2**, 429–439 (2008).
DOI: [10.3144/expresspolymlett.2008.52](https://doi.org/10.3144/expresspolymlett.2008.52)
- [8] Fritzsche J., Das A., Jurk R., Stöckelhuber K. W., Heinrich G., Klüppel M.: Relaxation dynamics of carboxylated nitrile rubber filled with organomodified nanoclay. *Express Polymer Letters*, **2**, 373–381 (2008).
DOI: [10.3144/expresspolymlett.2008.44](https://doi.org/10.3144/expresspolymlett.2008.44)
- [9] Das A., Jurk R., Stöckelhuber K. W., Heinrich G.: Rubber curing chemistry governing the orientation of layered silicate. *Express Polymer Letters*, **1**, 717–723 (2007).
DOI: [10.3144/expresspolymlett.2007.99](https://doi.org/10.3144/expresspolymlett.2007.99)
- [10] Chow W. S., Yap Y. P.: Optimization of process variable on flexural properties of epoxy/organo-montmorillonite nanocomposite by response surface methodology. *Express Polymer Letters*, **2**, 2–11 (2008).
DOI: [10.3144/expresspolymlett.2008.2](https://doi.org/10.3144/expresspolymlett.2008.2)
- [11] Mishra S. B., Luyt A. S.: Effect of organic peroxides on the morphological, thermal and tensile properties of EVA-organoclay nanocomposites. *Express Polymer Letters*, **2**, 256–264 (2008).
DOI: [10.3144/expresspolymlett.2008.31](https://doi.org/10.3144/expresspolymlett.2008.31)
- [12] Pradhan D. K., Choudhary R. N. P., Samantaray B. K.: Studies of structural, thermal and electrical behavior of polymer nanocomposite electrolytes. *Express Polymer Letters*, **2**, 630–638 (2008).
DOI: [10.3144/expresspolymlett.2008.76](https://doi.org/10.3144/expresspolymlett.2008.76)
- [13] Kokabi M., Sirousazar M., Hassan Z. M.: PVA-clay nanocomposite hydrogels for wound dressing. *European Polymer Journal*, **43**, 773–781 (2007).
DOI: [10.1016/j.eurpolymj.2006.11.030](https://doi.org/10.1016/j.eurpolymj.2006.11.030)
- [14] Strawhecker K. E., Manias E.: Structure and properties of poly(vinyl alcohol)/Na⁺ montmorillonite nanocomposites. *Chemistry of Materials*, **12**, 2943–2949 (2000).
DOI: [10.1021/cm000506g](https://doi.org/10.1021/cm000506g)
- [15] Strawhecker K. E., Manias E.: AFM of poly(vinyl alcohol) crystals next to an inorganic surface. *Macromolecules*, **34**, 8475–8482 (2001).
DOI: [10.1021/ma0101862](https://doi.org/10.1021/ma0101862)
- [16] Yu Y-H., Lin C-Y., Yeh J-M., Lin W-H.: Preparation and properties of poly(vinyl alcohol)-clay nanocomposite materials. *Polymer*, **44**, 3553–3560 (2003).
DOI: [10.1016/S0032-3861\(03\)00062-4](https://doi.org/10.1016/S0032-3861(03)00062-4)
- [17] Bandi S., Schiraldi D. A.: Glass transition behavior of clay aerogel/poly(vinyl alcohol) composites. *Macromolecules*, **39**, 6537–6545 (2006).
DOI: [10.1021/ma0611826](https://doi.org/10.1021/ma0611826)
- [18] Kanapitsas A., Pissis P., Kotsilkova R.: Dielectric studies of molecular mobility and phase morphology in polymer-layered silicate nanocomposites. *Journal of Non-Crystalline Solids*, **305**, 204–211 (2002).
DOI: [10.1016/S0022-3093\(02\)01107-9](https://doi.org/10.1016/S0022-3093(02)01107-9)
- [19] Noda N., Lee Y-H., Bur A. J., Prabhu V. M., Snyder C. R., Roth S. C., McBrearty M.: Dielectric properties of nylon 6/clay nanocomposites from on-line process monitoring and off-line measurements. *Polymer*, **46**, 7201–7217 (2005).
DOI: [10.1016/j.polymer.2005.06.046](https://doi.org/10.1016/j.polymer.2005.06.046)
- [20] Wang H-W., Chang K-C., Chu H-C., Liou S-J., Yeh J-M.: Significant decreased dielectric constant and loss of polystyrene-clay nanocomposite materials by using long-chain intercalation agent. *Journal of Applied Polymer Science*, **92**, 2402–2410 (2004).
DOI: [10.1002/app.20192](https://doi.org/10.1002/app.20192)
- [21] Wang H-W., Shieh C-F., Chang K-C., Chu H-C.: Synthesis and dielectric properties of poly(methyl methacrylate)-clay nanocomposite materials. *Journal of Applied Polymer Science*, **97**, 2175–2181 (2005).
DOI: [10.1002/app.21817](https://doi.org/10.1002/app.21817)
- [22] Bur A. J., Lee Y-H., Roth S. C., Start P. R.: Measuring the extent of exfoliation in polymer/clay nanocomposites using real-time process monitoring methods. *Polymer*, **46**, 10908–10918 (2005).
DOI: [10.1016/j.polymer.2005.08.091](https://doi.org/10.1016/j.polymer.2005.08.091)
- [23] Sengwa R. J., Choudhary S., Sankhla S.: Dielectric spectroscopy of hydrophilic polymers-montmorillonite clay nanocomposite aqueous colloidal suspension. *Colloids and Surfaces A: Physicochemical and Engineering Aspects*, **336**, 79–87 (2009).
DOI: [10.1016/j.colsurfa.2008.11.015](https://doi.org/10.1016/j.colsurfa.2008.11.015)

- [24] Davis R. D., Bur A. J., McBrearty M., Lee Y-H., Gilman J. W., Start P. R.: Dielectric spectroscopy during extrusion processing of polymer nanocomposites: A high throughput processing/characterization method to measure layered silicate content and exfoliation. *Polymer*, **45**, 6487–6493 (2004). DOI: [10.1016/j.polymer.2004.07.047](https://doi.org/10.1016/j.polymer.2004.07.047)
- [25] Mijovic J., Lee H., Kenny J., Mays J.: Dynamics in polymer-silicate nanocomposites as studied by dielectric relaxation spectroscopy and dynamic mechanical spectroscopy. *Macromolecules*, **39**, 2172–2182 (2006). DOI: [10.1021/ma051995e](https://doi.org/10.1021/ma051995e)
- [26] Psarras G. C., Gatos K. G., Karahaliou P. K., Georga S. N., Krontiras C. A., Karger-Kocsis J.: Relaxation phenomena in rubber/layered silicate nanocomposites. *Express Polymer Letters*, **1**, 837–845 (2007). DOI: [10.3144/expresspolymlett.2007.116](https://doi.org/10.3144/expresspolymlett.2007.116)
- [27] Pluta M., Jeszka J. K., Boiteux G.: Polylactide/montmorillonite nanocomposites: Structure, dielectric, viscoelastic and thermal properties. *European Polymer Journal*, **43**, 2819–2835 (2007). DOI: [10.1016/j.eurpolymj.2007.04.009](https://doi.org/10.1016/j.eurpolymj.2007.04.009)
- [28] Kim D. H., Cho K. S., Mitsumata T., Ahn K. H., Lee S. J.: Microstructural evolution of electrically activated polypropylene/layered silicate nanocomposites investigated by *in situ* synchrotron wide-angle X-ray scattering and dielectric relaxation analysis. *Polymer*, **47**, 5938–5945 (2006). DOI: [10.1016/j.polymer.2006.06.029](https://doi.org/10.1016/j.polymer.2006.06.029)
- [29] Sengwa R. J., Choudhary S., Sankhla S.: Low frequency dielectric relaxation processes and ionic conductivity of montmorillonite clay nanoparticles colloidal suspension in poly(vinyl pyrrolidone)-ethylene glycol blends. *Express Polymer Letters*, **2**, 800–809 (2008). DOI: [10.3144/expresspolymlett.2008.93](https://doi.org/10.3144/expresspolymlett.2008.93)
- [30] Sengwa R. J., Choudhary S., Sankhla S.: Dielectric behaviour and relaxation processes of montmorillonite clay nano-platelet colloidal suspensions in poly(vinyl pyrrolidone)-ethylene glycol oligomer blends. *Polymer International*, **58**, 781–789 (2009). DOI: [10.1002/pi.2592](https://doi.org/10.1002/pi.2592)
- [31] Sengwa R. J., Sankhla S., Choudhary S.: Dielectric relaxation processes and ionic conduction behaviour in poly(ethylene oxide)-montmorillonite clay nanocomposite aqueous colloidal suspensions. *Colloids and Polymer Science*, **287**, 1013–1024 (2009). DOI: [10.1007/s00396-009-2056-6](https://doi.org/10.1007/s00396-009-2056-6)
- [32] Kortaberria G., Solar L., Jimeno A., Arruti P., Gómez C., Mondragon I.: Curing of an epoxy resin modified with nanoclay monitored by dielectric spectroscopy and rheological measurements. *Journal of Applied Polymer Science*, **102**, 5927–5933 (2006). DOI: [10.1002/app.25108](https://doi.org/10.1002/app.25108)
- [33] Kriptou S., Pissis P., Savelyev Y. V., Robota L. P., Travinskaya T. V.: Polymer dynamics in polyurethane/clay nanocomposites studied by dielectric and thermal techniques. *Journal of Macromolecular Science Part B: Physics*, **49**, 86–110 (2010). DOI: [10.1080/00222340903344309](https://doi.org/10.1080/00222340903344309)
- [34] Sengwa R. J., Sankhla S., Choudhary S.: Dielectric characterization of solution intercalation and melt intercalation poly(vinyl alcohol)-poly(vinyl pyrrolidone) blend- montmorillonite clay nanocomposite films. *Indian Journal of Pure and Applied Physics*, **48**, 196–204 (2010).
- [35] Havriliak S., Negami S.: A complex plane analysis of α -dispersions in some polymer systems. *Journal of Polymer Science Part C: Polymer Symposia*, **14**, 99–117 (1966). DOI: [10.1002/polc.5070140111](https://doi.org/10.1002/polc.5070140111)
- [36] Mishra R., Rao K. J.: Electrical conductivity studies of poly(ethyleneoxide)-poly(vinylalcohol) blends. *Solid State Ionics*, **106**, 113–127 (1998). DOI: [10.1016/S0167-2738\(97\)00493-1](https://doi.org/10.1016/S0167-2738(97)00493-1)
- [37] Aziz S. B., Abidin Z. H. Z., Arof A. K.: Influence of silver ion reduction on electrical modulus parameters of solid polymer electrolyte based on chitosansilver triflate electrolyte membrane. *Express Polymer Letters*, **4**, 300–310 (2010). DOI: [10.3144/expresspolymlett.2010.38](https://doi.org/10.3144/expresspolymlett.2010.38)
- [38] Sengwa R. J., Sankhla S.: Solvent effects on the dielectric dispersion of poly(vinyl pyrrolidone)-poly(ethylene glycol) blends. *Colloids and Polymer Science*, **285**, 1237–1246 (2007). DOI: [10.1007/s00396-007-1676-y](https://doi.org/10.1007/s00396-007-1676-y)
- [39] Sengwa R. J., Sankhla S.: Dielectric dispersion study of coexisting phases of aqueous polymeric solution: Poly(vinyl alcohol) + poly(vinyl pyrrolidone) two-phase systems. *Polymer*, **48**, 2737–2744 (2007). DOI: [10.1016/j.polymer.2007.03.030](https://doi.org/10.1016/j.polymer.2007.03.030)
- [40] Wang M., Dong S.: Enhanced electrochemical properties of nanocomposite polymer electrolyte based on copolymer with exfoliated clays. *Journal of Power Sources*, **170**, 425–432 (2007). DOI: [10.1016/j.jpowsour.2007.04.031](https://doi.org/10.1016/j.jpowsour.2007.04.031)

Nanocomposites of poly(methyl methacrylate) (PMMA) and montmorillonite (MMT) Brazilian clay: A tribological study

W. Brostow^{1,2*}, M. Dutta^{1,4}, J. Ricardo de Souza^{1,3}, P. Rusek², A. Marcos de Medeiros³, E. N. Ito³

¹Laboratory of Advanced Polymers & Optimized Materials (LAPOM), Department of Materials Science and Engineering and Center for Advanced Research and Technology (CART), University of North Texas, 1155 Union Circle #305310, Denton, TX 76203-5017, USA

²College of Mechanics and Robotics, AGH University of Science and Technology, Adama Mickiewicza 30, 30 – 059 Cracow, Poland

³Department of Materials Engineering, Federal University of Rio Grande do Norte, Avenida Senador Salgado Filho, 3000, CEP 59078-970/Natal – RN, Brasil;

⁴Now at Department of Materials, University of Oxford, Parks Road, Oxford OX1 3PH, United Kingdom

Received 17 February 2010; accepted in revised form 28 May 2010

Abstract. Nanocomposites of PMMA+MMT Brazilian clays were developed by mechanical mixing in co-rotational twin-screw extrusion and injection molding with varying weight fraction of MMT Brazilian clays. The clays were purchased in crude form and then washed and purified to extract the organic materials and contaminants.

Dynamic friction and wear rate of these composites were studied as a function of concentration of the Brazilian clay. With an increase in the amount of MMT Brazilian clay, the dynamic friction of the nanocomposites increases, a clear but not large effect. It can be explained by sticky nature of clay; clay in the composite is also on the surface and sticks to the partner surface. The wear rate as a function of the clay concentration passes through a minimum at 1 wt% MMT; at this concentration the clay provides a reinforcement against abrasion. At higher clay concentrations we see a dramatic increase in wear – a consequence of clay agglomeration and increased brittleness. The conclusions are confirmed by microscopy results.

Keywords: nanocomposites, poly(methyl methacrylate), montmorillonite, dynamic friction, wear

1. Introduction

Most of the work on tribology to date, in particular at the micro- and nano-scale, is focused on metals and ceramics used for nano-electronics industry and microelectro-mechanical systems (MEMS). Although polymers and polymer nanocomposites, owing to their adequate strength, lightness, versatility, ease of processing and low cost, have been widely employed to replace the traditional metals and ceramics in microelectronic packaging, coatings, aerospace, automotive, food packaging and biomedical applications, not much research has been done on them in this regard. This may be due

to their viscoelastic properties, which makes the processes and analysis complicated. Additionally, in the case of polymer nanocomposites, detailed knowledge of the role of nano-fillers during the tribological processes, and the precise relationships between structures, properties and processing are required [1].

Nanostructured materials promise fruitful development for applications in the aerospace sector due to their high strength, low density and thermal stability. These applications include equipping aircrafts, rockets, space stations and platforms for planetary or solar exploration [2]. Nanotechnology has

*Corresponding author, e-mail: wbrostow@yahoo.com
© BME-PT

attracted the interest of numerous research groups around the world due to its potential for application in various industries [3].

Poly(methyl methacrylate) (PMMA) is an important amorphous thermoplastic with desirable properties, including clarity (the transparency is close to the ultraviolet region and also the infrared), chemical resistance, good moldability, protection against ultraviolet radiation, good weatherability, high strength, and dimensional stability [4–6]. Moreover, PMMA has good resistance to both acidic and alkaline environments. PMMA is resistant to many inorganic reagents, aliphatic hydrocarbons, non-polar solvents and acidic and alkaline solutions [7]. However, PMMA has limitations in its thermal stability and mechanical-dynamical properties at high temperatures. One way to improve the performance of polymers is the addition of nanoparticles such as clays, silica or carbon nanotubes to the polymer matrix [8–11]. Nanocomposites based on layered smectite clays as the reinforcing part of the matrix often exhibit improved mechanical properties [6]. Usually, PMMA nanocomposites offer a potential for reduced gas permeability, improved physical performance, and increased heat resistance – often without a sacrifice in optical clarity [6].

Understanding the physical nature of friction, the definition of wear, its consequences, its mechanisms and ways to control its effects are fundamental to modern engineering. The purpose of this study was to evaluate the tribological performance of nanocomposites consisting of PMMA and montmorillonite (MMT) Brazilian clay.

2. Experimental

2.1. Materials

Neat PMMA Cristal 01-DH-ECL used was kindly donated by the Unigel SA (Sao Bernardo Do Campo, Brazil) company. Its melt index is 2.5 g/10 min (ASTM D 1238). MMT Brazilian clay from the company Bentonisa was used as a filler. There is no significant difference between the clay we have used and clays from other countries.

2.2. Preparation of clay

The clay was purchased in crude form and was washed and purified to extract the organic materials and contaminants. It was subsequently dried in an

oven with circulating air for 48 h at 60°C to remove any excess water remaining after washing.

2.3. Processing

Initially, before the steps of extrusion mixing and injection molding, all materials were kept in vacuum at 60°C for 15 h to remove any humidity absorbed by the materials.

Table 1 shows the formulations of nanocomposites mixed in a twin-screw extruder, B&P Process Equipment, model MP19-TC ($d = 19$ mm and $L/D = 25$), using a temperature profile of 180°C in the feed zone and 200/210/220/210°C in the subsequent areas. The extruder was used in co-rotating configuration.

The samples were injection molded in an Arburg Allrounder model 270V machine using the following temperature profile: 210/220/230/230/240°C and mold temperature of 50°C.

Table 1. Formulations of nanocomposites

#	Composition	% Weight fraction
1	Neat PMMA	100
2	PMMA/MMT	99/1
3	PMMA/MMT	97/3
4	PMMA/MMT	95/5

2.4. Friction determination

Nanovea pin-on-disc tribometer from Micro Photonics Inc., was used for determining dynamic friction. A SS 302 grade stainless ball with diameter 3.20 mm was used as the pin. The pin was loaded onto the test sample with a precisely known weight of 5.0 N. The highly stiff elastic arm insures a nearly fixed contact point and thus a stable position in the friction track. Dynamic friction is determined during the test by measuring the deflection of the elastic arm by direct measurement of the change in torque [12]. The rotation speed of the disc was 100.0 rpm and the radius of wear track was 2.0 mm. The test was performed for 5000 revolutions under room temperature conditions. The results reported are averages from 3 runs.

2.5. Wear rate determination

Wear rate was determined through the wear track resulted due to the pin-on-disc friction test after 5000 revolutions. The wear track width was deter-

mined using a Veeco Dektak 150 profilometer. A profilometer measures the vertical depth of a horizontal material and is often used for determination of relative surface roughness of a material. It amplifies and records the vertical motions of a stylus (in contact with the test material) which is slowly dragged along the surface of the material at a constant speed. As the stylus moves, the stylus rides over the sample surface detecting surface deviations; i.e., the vertical deflection of the stylus measures the change in step height [13].

A stylus with tip radius of 12.5 μm was used. The force applied to the sample was 1.0 mg, and scan rate was 26.7 μm/s. The scan length was 800 μm and the measurement range was 65.5 μm.

Seven values of wear track width were measured at different locations on each sample and averaged for the purpose of accuracy. All samples were cleaned by high pressure air to remove all debris before each test.

Volume loss due to wear V_m was then calculated using the Equation (1) as suggested by the ASTM G99-05 standard:

$$V_m = 2\pi RA^2 \tag{1}$$

where V_m is the volume loss in mm³, R is the wear track radius in mm (2.0 mm in this case), and A is the wear area width in mm².

Wear rate Z was then calculated using Equation (2):

$$Z = \frac{V_m}{WX} \tag{2}$$

where Z is in mm³/Nm, V_m is the volume loss due to wear in mm³, W is the load in N, and X is the sliding distance in m.

3. Dynamic friction

Results of dynamic friction determination for neat PMMA, and PMMA with 1.0, 3.0 and 5.0 wt% of MMT clay are presented in Figure 1. It can be observed that the friction variation among the samples tested is quite small. However, for the values of average dynamic friction seen in Figure 2, there is a certain growing trend with increasing percentage of MMT clay. This can be explained by the sticky nature of clay; clay present in the composite appears also on the surface, thus sticks to the partner surface and enhances friction somewhat.

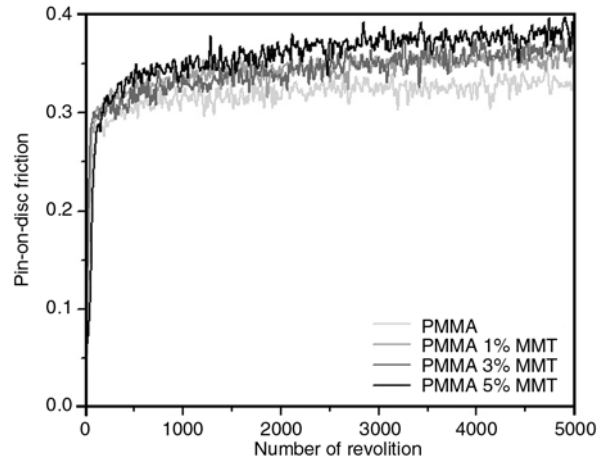


Figure 1. Pin-on-disc friction vs. number of revolutions

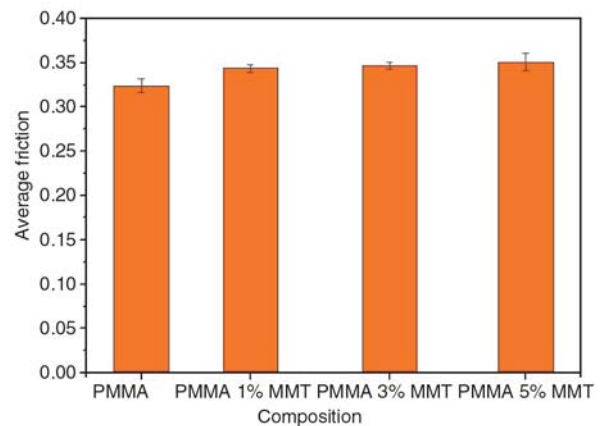


Figure 2. Average friction vs composition

4. Wear rate

In Figure 3 it can be observed that the wear rate as a function of the clay concentration passes through a minimum at 1.0% clay. Thus, for neat PMMA and PMMA with 1.0% MMT clay, the wear rates are much lower than for the composites with 3.0 and

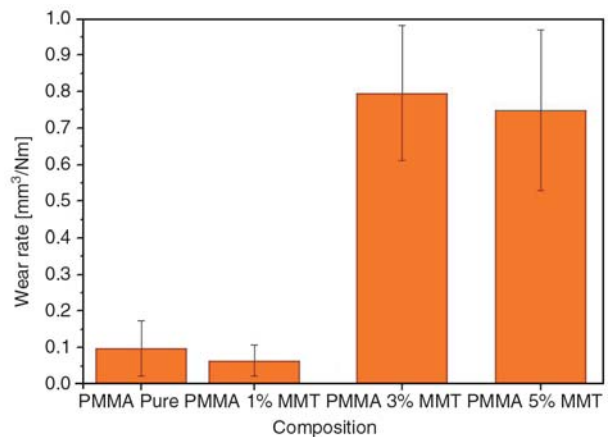


Figure 3. Wear rate for several compositions

5.0% of MMT clay. Usually the presence of clay decreases the elongation at break ϵ_b of the material. Since ϵ_b is inversely proportional to the brittleness of the material [14–16], the brittleness increases leading to an increase in wear rate.

Furthermore, it is important to note that the dispersion values of wear rates for samples of PMMA with 3 and 5% of MMT are higher than the dispersion values of wear rate for samples of neat PMMA and 1% MMT. Thus, the samples with higher MMT concentration have less uniform morphologies – a consequence of agglomeration (see below SEM microscopy results).

5. Optical microscopy

Surfaces of the samples subjected to pin-on-disc tests were analyzed by optical microscopy in order to observe the wear tracks generated. Figure 4

shows the optical micrographs of the composites obtained through Olympus GX 51 optical microscope at 50 \times using Image Pro Plus software.

It can be observed that the wear tracks in case of PMMA with 3 and 5% of MMT are much deeper than for neat PMMA and 1% of MMT – in agreement with wear rates seen in Figure 3. We also see that the worn surfaces of the track exhibit layer-like waves.

6. A survey of results

Tribology of polymer-based materials (PBMs) has still a way to go, although certain mechanisms are emerging [17–19]. Fillers are a way to improve a variety of properties of PBMs [20] and clays have been used for that purpose [21–25]. We find that clay content in the nanocomposites has an influence on the dynamic friction and wear rate values.

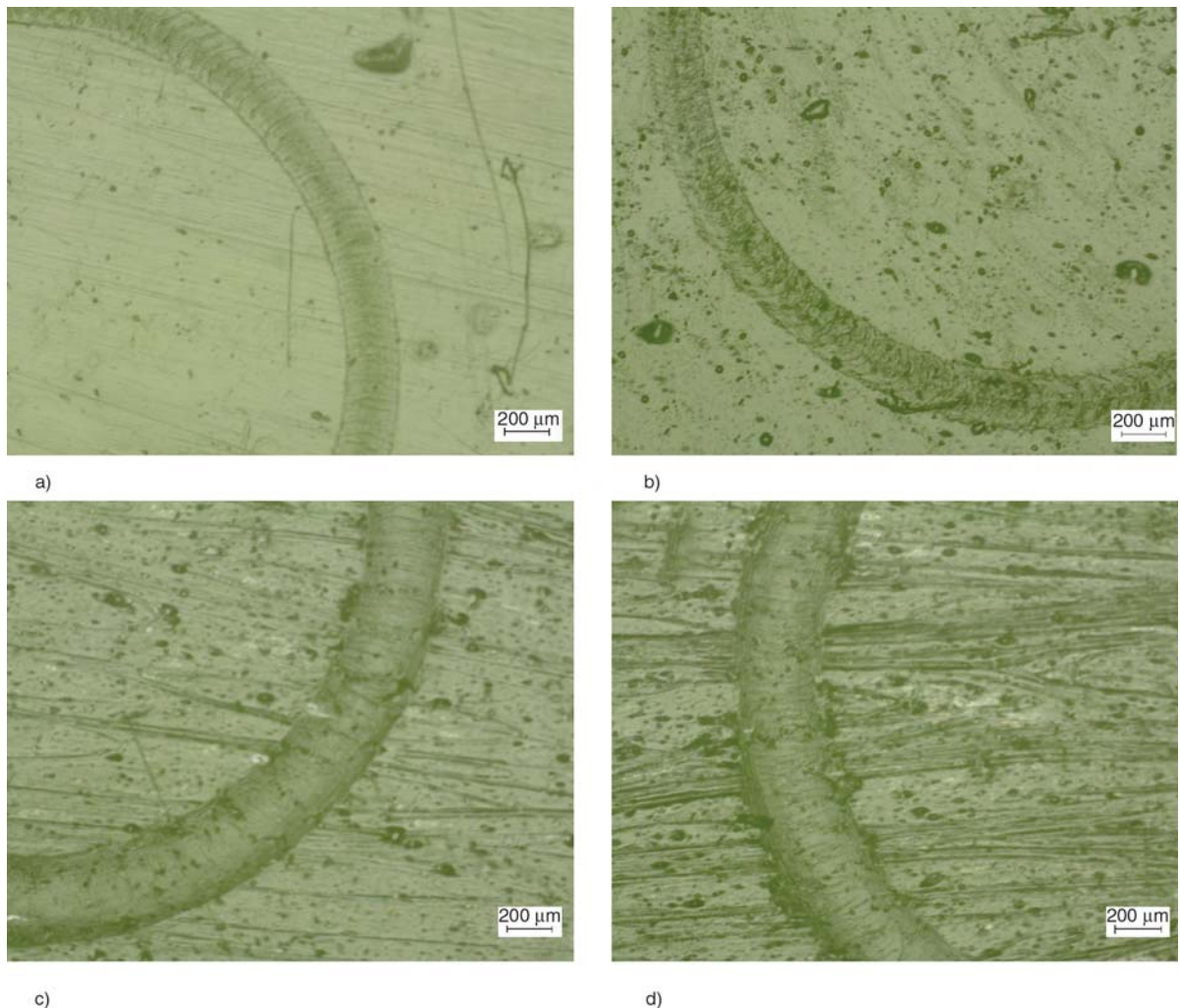


Figure 4. Optical micrographs of the worn surfaces at 50 \times . (a) Neat PMMA; (b) PMMA + 1.0 wt% MMT; (c) PMMA + 3.0% MMT; (d) PMMA + 5.0% MMT.

We have determined dynamic friction using a technique applied before [26–29]. With increase in the amount of MMT Brazilian clay, the dynamic friction of the nanocomposites increases. Above we have explained these results by the sticky nature of clay.

The wear rate as a function of concentration of clay diagram has a more complex shape and exhibits a minimum at 1 wt% MMT. We infer that addition of 1% clay provides a reinforcement since the clay particles are well dispersed in the matrix. Thus, the pin of the tribometer encounters more resistance than it had ‘attacking’ neat polymer; this is why the wear is lower than in neat PMMA.

The presence of clay is known to decrease the elongation at break ϵ_b of the material and – as argued above – the brittleness increases. This effect is apparently small when we have only 1% clay. When we put in 3% MMT, *agglomeration* of clay manifests itself. As expected, the agglomeration is even stronger for 5% MMT – as seen in Figure 4. Also the wear tracks for 3 and 5% are wider – another consequence of agglomeration and a direct contributor to wear. This is why we see a dramatic increase of wear for 3% MMT after the 1% minimum. Interestingly, the wear for 5% is somewhat lower than for 3%. Apparently, present at 3%, MMT only disrupts the structure of the polymer and weakens the material. At 5% MMT, its agglomerations are large enough to offer ‘their own’ resistance to deformation and wear.

As argued among others in [17], there is much more activity concerning mechanical properties of composites than tribological ones. However, these two classes of properties are connected. Thus, it was demonstrated in [14] that brittleness is related to recovery (healing) in scratch testing. Lower brittleness is seen along with more healing, a simple relationship found for a large variety of materials and composites. Sometimes the relations between mechanical and tribological properties are more complicated. The degree of improvement of any property depends on the choice of filler origin, particles size and shape. The challenges in this area of high-performance polymers consist in obtaining a significant improvement in the adhesion between the interphases and to achieve a homogeneous dispersion of the filler in the polymer matrix [29]. For polypropylene (PP) + polystyrene (PS) blends,

addition of a compatibilizer enhances the impact strength [30]. The same compatibilizer either increases or decreases static and dynamic friction; the change depends on the PP/PS ratio.

Acknowledgements

We thank the companies Unigel (Grupo Unigel S. A., São Paulo) and Bentonisa (Bentonite Northeast S. A., Boa Vista, Paraíba) for donating materials. We would also like to thank Prof. Elias Hage Jr. of DEMA-UFSCar (Department of Materials Engineering, Federal University of São Carlos, São Paulo) for his support in the use of infrastructure and processing. We also thank CNPq (National Council for Scientific and Technological Development of Brazil) for supporting the research project No. 474821/2008-0 and the Robert A. Welch Foundation, Houston, for supporting the research project # B-1203.

References

- [1] Dasari A., Yu Z-Z., Mai Y-W.: Fundamental aspects and recent progress on wear/scratch damage in polymer nanocomposites. *Materials Science and Engineering R: Reports*, **63**, 31–80 (2009). DOI: [10.1016/j.mser.2008.10.001](https://doi.org/10.1016/j.mser.2008.10.001)
- [2] Youtie J., Iacopetta M., Graham S.: Assessing the nature of nanotechnology: can we uncover an emerging general purpose technology? *The Journal of Technology Transfer*, **33**, 315–329 (2008). DOI: [10.1007/s10961-007-9030-6](https://doi.org/10.1007/s10961-007-9030-6)
- [3] Durán N., Mattoso L. H. C., Morais P. C.: *Nanotecnologia* (in Portuguese). Artliber, São Paulo (2006).
- [4] Mark H. F.: *Encyclopedia of polymer science and technology*. Wiley, New York (1985).
- [5] Bamfor C. H., Tipper C. F. H.: *Degradation of polymers*. Elsevier, Amsterdam (1975).
- [6] Silva A., Soares B. G., Zaioncz S., Dahmouche K.: Poly(methyl methacrylate)-clay nanocomposites prepared by in situ intercalative polymerization: The effect of the acrylic acid. *LNLS 2007 Activity Report* (2007).
- [7] Gross S., Camozzo D., Di Noto V., Armelao L., Tonello E.: PMMA: A key macromolecular component for dielectric low- κ hybrid inorganic-organic polymer films. *European Polymer Journal*, **43**, 673–696 (2007). DOI: [10.1016/j.eurpolymj.2006.12.012](https://doi.org/10.1016/j.eurpolymj.2006.12.012)
- [8] Etienne S., Becker C., Ruch D., Grignard B., Cartigny G., Detrembleur C., Calberg C., Jerome R.: Effects of incorporation of modified silica nanoparticles on the mechanical and thermal properties of PMMA. *Journal of Thermal Analysis and Calorimetry*, **87**, 101–104 (2007). DOI: [10.1007/s10973-006-7827-4](https://doi.org/10.1007/s10973-006-7827-4)

- [9] Kashiwagi T., Morgan A. B., Antonucci J. M., Van-Landingham M. R., Harris R. H., Awad W. H., Shields J. R.: Thermal and flammability properties of a silica-poly(methylmethacrylate) nanocomposite. *Journal of Applied Polymer Science*, **89**, 2072–2078 (2003). DOI: [10.1002/app.12307](https://doi.org/10.1002/app.12307)
- [10] Kashiwagi T., Du F., Douglas J. F., Winey K. I., Harris R. H., Shields J. R.: Nanoparticle networks reduce the flammability of polymer nanocomposites. *Nature Materials*, **4**, 928–933 (2005). DOI: [10.1038/nmat1502](https://doi.org/10.1038/nmat1502)
- [11] Medeiros A. M., Santos C. J. C., Paskocimas C. A., Melo J. D. D., Ito E. N., Araújo E. M., Hage Jr. E.: Preliminary study on the development of nanocomposites of poly(methyl methacrylate) (PMMA) and montmorillonite (MMT) brazilian clay. in 'Proceeding of 10th Brazilian Polymer Congress. Fox do Iguacu, Brasil' 2–4 (2009).
- [12] Dutta M.: Modified epoxy coatings on mild steel: A study of tribology and surface energy. Masters' thesis, University of North Texas (2009).
- [13] Bhushan B.: Introduction to tribology. Wiley, New York (2002).
- [14] Brostow W., Hagg Lobland H. E., Narkis M.: Sliding wear, viscoelasticity and brittleness of polymers. *Journal of Materials Research*, **21**, 2422–2428 (2006). DOI: [10.1557/JMR.2006.0300](https://doi.org/10.1557/JMR.2006.0300)
- [15] Brostow W., Hagg Lobland H. E.: Predicting wear from mechanical properties of thermoplastic polymers. *Polymer Engineering and Science*, **48**, 1982–1985 (2008). DOI: [10.1002/pen.21045](https://doi.org/10.1002/pen.21045)
- [16] Brostow W., Hagg Lobland H. E.: Brittleness of materials: Implications for composites and a relation to impact strength. *Journal of Materials Science*, **45**, 242–250 (2010). DOI: [10.1007/s10853-009-3926-5](https://doi.org/10.1007/s10853-009-3926-5)
- [17] Brostow W., Deborde J-L., Jaklewicz M., Olszynski P.: Tribology with emphasis on polymers: Friction, scratch resistance and wear. *Journal of Materials Education*, **25**, 119–132 (2003).
- [18] Myshkin N. K., Petrokovets M. I., Kovalev A. V.: Tribology of polymers: Adhesion, friction, wear, and mass-transfer. *Tribology International*, **38**, 910–916 (2005). DOI: [10.1016/j.triboint.2005.07.016](https://doi.org/10.1016/j.triboint.2005.07.016)
- [19] Brostow W., Simoes R.: Tribological and mechanical behavior of metals and polymers simulated by molecular dynamics. *Journal of Materials Education*, **27**, 19–28 (2005).
- [20] Rabello M.: Aditivacão de polimeros. Artliber, São Paulo (2000).
- [21] Gatos K. G., Thomann R., Karger-Kocsis J.: Characteristics of ethylene propylene diene monomer rubber/organoclay nanocomposites resulting from different processing conditions and formulations. *Polymer International*, **53**, 1191–1197 (2004). DOI: [10.1002/pi.1556](https://doi.org/10.1002/pi.1556)
- [22] Chow W. S., Mohd Ishak Z. A., Karger-Kocsis J.: Atomic force microscopy study on blend morphology and clay dispersion in polyamide-6/polypropylene/organoclay systems. *Journal of Polymer Science Part B: Polymer Physics*, **43**, 1198–1204 (2005). DOI: [10.1002/polb.20408](https://doi.org/10.1002/polb.20408)
- [23] Karger-Kocsis J., Shang P. P., Mohd Ishak Z. A., Rösch M.: Melting and crystallization of in-situ polymerized cyclic butylene terephthalates with and without organoclay: A modulated DSC study. *Express Polymer Letters*, **1**, 60–68 (2007). DOI: [10.3144/expresspolymlett.2007.12](https://doi.org/10.3144/expresspolymlett.2007.12)
- [24] Pegoretti A., Dorigato A., Penati A.: Tensile mechanical response of polyethylene-clay nanocomposites. *Express Polymer Letters*, **1**, 123–131 (2007). DOI: [10.3144/expresspolymlett.2007.21](https://doi.org/10.3144/expresspolymlett.2007.21)
- [25] Arribas A., Bermúdez M-D., Brostow W., Carrion-Vilches F. J., Olea-Mejia O.: Scratch resistance of a polycarbonate + organoclay nanohybrid. *Express Polymer Letters*, **3**, 621–629 (2009). DOI: [10.3144/expresspolymlett.2009.78](https://doi.org/10.3144/expresspolymlett.2009.78)
- [26] Brostow W., Datashvili T., Huang B.: Tribological properties of blends of melamine-formaldehyde resin with low density polyethylene. *Polymer Engineering and Science*, **48**, 292–296 (2008). DOI: [10.1002/pen.20898](https://doi.org/10.1002/pen.20898)
- [27] Brostow W., Chonkaew W., Datashvili T., Menard K. P.: Tribological properties of epoxy + silica hybrid materials. *Journal of Nanoscience and Nanotechnology*, **8**, 1916–1921 (2008). DOI: [10.1166/jnn.2009.368](https://doi.org/10.1166/jnn.2009.368)
- [28] Brostow W., Chonkaew W., Menard K. P., Scharf W.: Modification of an epoxy resin with a fluoroepoxy oligomer for improved mechanical and tribological properties. *Materials Science and Engineering: A*, **507**, 241–251 (2009). DOI: [10.1016/j.msea.2008.12.008](https://doi.org/10.1016/j.msea.2008.12.008)
- [29] Brostow W., Datashvili T., Kao D., Too J.: Tribological properties of LDPE + boehmite composites. *Polymer Composites*, **31**, 417–425 (2010).
- [30] Brostow W., Holjevac Grguric T., Olea-Mejia O., Pietkiewicz D., Rek V.: Polypropylene + polystyrene blends with a compatibilizer. Part 2. Tribological and mechanical properties. *e-Polymers*, no. 034 (2008).

Systematically varied interfaces of continuously reinforced glass fibre/polypropylene composites: Comparative evaluation of relevant interfacial aspects

J. Rausch, R. C. Zhuang, E. Mäder*

Department of Composites, Leibniz Institute of Polymer Research Dresden, Hohe Strasse 6, 01069 Dresden, Germany

Received 10 May 2010; accepted in revised form 9 June 2010

Abstract. Interface related mechanical properties of unidirectional continuous glass fibre (GF)/polypropylene (PP) composites made of commingled yarns have been systematically studied according to a three level, three-factor factorial design. The three systematically varied factors comprised different silane coupling agent and film former contents in GF sizings as well as a varying GF diameter. Besides the statistical evaluation of those main effects on the transverse tensile and compression shear strengths of the composites, interfacial shear strength measurements on model composites have been performed. The latter ones as well as the results of the dynamic mechanical thermal analysis support the statistical significance of sizing components, the sizing content on the GF, and GF diameter for the mechanical properties of the composites. This highlights the interplay of proper sizing formulation and reproducible GF-spinning conditions, as both affect the interfacial bonding of continuously reinforced GF/PP composites.

Keywords: polymer composites, adhesion, coatings, reinforcements, mechanical properties

1. Introduction

In order to take advantage of the reinforcing ability of fibres in composite materials, the external stress is transferred to the fibres via the fibre/matrix interface. Thus, the composites properties are not only limited by the characteristics of the reinforcing fibres and the matrix polymer, but are affected to a great extent by the interfacial bonding between fibre and matrix as well as the interphasial properties. The interphase is a three dimensional region between fibre and matrix, mainly formed by the interdiffusion of the sizing and the matrix in the course of composite consolidation. The local properties, such as thermal, mechanical, chemical, and morphological characteristics are different from the ones of the surrounding bulk matrix.

Nowadays, the existence of a transition region between fibre and matrix is widely accepted and

new characterization methods revealed locally different properties within a region of a few tens to a few hundreds of nanometers [1–5]. Sizing chemistry and interdiffusion play a great part in the development of interphases, which have been investigated in our earlier work [5]. When the sizing layer becomes the ‘weak point’ of the system, failure occurs within it [4, 6, 7].

Considering GF sizings, which commonly amount to 0.5–1% of the fibre weight [8], their formulation consists of mainly three constituents: organofunctional silanes, polymeric film formers, and processing aids. The primary importance of organofunctional silanes is their ability to serve as an adhesion promoter or coupling agent providing a link between the matrix and the fibre surface by covalent bonding [9]. Polymeric film formers represent the biggest weight fraction in GF sizings. Besides

*Corresponding author, e-mail: emaeder@ipfdd.de
© BME-PT

their vital importance for fibre protection and processability of the yarns, they affect the wetting of the fibre as well as the distribution of the silane on the fibre surface and consequently the mechanical performance of the composites [10]. Processing aids can include substances providing anti-static properties and lowering the friction during spinning and textile processing. Besides conventional sizing formulations, recent studies report on the incorporation of nanoparticles into aqueous sizings or coatings for enhanced fibre matrix adhesion [11–13] or functionalisation of the interphase by creating diffusion barriers [14]. Moreover, nanoparticles, namely carbon nanotubes, have been used for interphasial strain sensing [15–18].

Upon consolidation of the composites, interdiffusion of the sizing constituents with the matrix polymer takes place, resulting in graded physical properties within a transition zone, i.e. the interphase, between the fibre and the bulk polymer [7]. As the film former content in GF sizings is comparably high, its amount on the fibre surface as well as its chemical composition largely influence the evolution of the interphase [19]. Due to the currently available characterization techniques, the interphase dimensions and properties can be detected directly. In this context, atomic force microscopy (AFM) related measurements, e.g. phase imaging, nano-scratch and nano-indentation [5, 20, 21] or the use of microthermal analysis [22, 23] have revealed gradient properties as well as the local extension of the interphase for several fibre/matrix systems. Additionally, the effects of different fibre treatments, including the application of different silanes, film formers and coatings have been studied and related to the mechanical properties of the composites [24–27]. Regarding the local extension of the interphase, it was mentioned that increasing the interphases thickness could turn them into ‘weak spots’ with regard to the mechanical performance of the composites [4, 6]. However, the interphase related properties do not solely depend on the local extension of the interphase, but rather depend on a complex interplay of many factors. To date, a large body of literature contributing information to silanes and interfacial or interphasial issues in composites materials is available. Reviews on certain aspects can be found in [2, 9, 28–30].

This study is concerned with the systematic evaluation of a sizing system, consisting of γ -amino-

propyltriethoxysilane (APS) and a PP film former, and its effect on interphase dominated micro and macro mechanical properties of continuously GF reinforced PP. The effects of the different sizing contents and formulations on the composite properties are evaluated statistically following a factorial design approach. Besides the constituents of the sizing formulation, the GF diameter, accounting for different surface areas and thus varying the average sizing thickness has been included into the factorial design. This approach allows determining the importance and interplay of the above mentioned factors on the dependent variables, i.e. the composites transverse and compression shear strength. In conjunction with the results of the factorial design by means of other methods, e.g. single fibre pull-out (SFPO) tests, dynamic mechanical thermal analysis (DMA), differential scanning calorimetry (DSC) and high temperature gel permeation chromatography (HT-GPC), additional information on selected composites and composites properties is presented providing an insight into the mechanisms of interphase related composite failure.

2. Experimental

2.1. Composite manufacturing

Hybrid yarns, consisting of E-glass and PP filaments (approximately 50 vol% GF) were spun as described elsewhere [31]. For the spinning of the polymeric filaments the PP (HG455 FB from Borealis, Germany; weight average molecular weight (M_w) = 217 600 g/mol, melt flow rate (ISO 1133): 27 g/10 min) was melt blended with 2 wt% maleic anhydride grafted polypropylene (MAH-PP) (Exxelor PO1020 from Exxon mobile, USA; M_w = 86 000 g/mol). During the spinning process, different sizings based on APS and a PP film former were applied on the GF. The latter one is a MAH-PP based aqueous dispersion (Permanol 602 from Clariant, Switzerland), with M_w = 147 600 g/mol and a mean particle size of approximately 100 nm. The sizing content was determined quantitatively by pyrolysis following DIN EN ISO 1172.

The manufacturing of the unidirectional specimens for mechanical testing was achieved by filament winding of the hybrid yarns on a rotating steel core. The textile preform was compression moulded (KV 207, Rucks GmbH, Germany) at 225°C for 45 min in a computer controlled long term cycle (heating,

consolidation and cooling in the mould). In detail, heating from ambient temperature to 225°C took 23 min at a pressure of 0.5 MPa, followed increasing the pressure to 3 MPa for 2 min, before cooling down to 40°C within 20 min. During the cooling pressure was kept constant at 3 MPa. As determined by pyrolysis, the GF content of all specimens was determined to be 74 ± 1.5 wt%, equal to ~ 50 vol%.

2.2. Mechanical testing and characterization

The transverse tensile strength was measured according to specification ISO 527-5 with a velocity of $1 \text{ mm}\cdot\text{min}^{-1}$ for at least 10 specimens ($2 \times 10 \times 140 \text{ mm}^3$) of each test series. Compression shear strength (CST) of the unidirectional composites was determined using a self-made testing device according to [32]. The CST test is a method for determining the apparent inter- and intralaminar shear strength of continuous fibre reinforced composites and involves a nearly pure and homogeneous shear load in the fracture plane of the specimen. Detailed information on the test setup is described elsewhere [32]. 10 specimens with the dimensions of $4 \times 10 \times 10 \text{ mm}^3$ were tested at $1 \text{ mm}\cdot\text{min}^{-1}$. Similar to the determination of the transverse tensile strength, the mechanical characterisation was performed on a UPM 1456 from Zwick GmbH & Co KG, Germany. For the determination of the interfacial shear strength (IFSS), SFPO measurements were performed on GF embedded $800 \mu\text{m}$ into the same matrix as used for the unidirectional composites. Details of the test setup are described elsewhere [33]. The Differential Scanning Calorimetry (DSC) measurements of the matrix PP as well as the film former was performed on a Q2000 (TA Instruments, USA) under nitrogen atmosphere in a temperature range from -50 to 205°C with a heating/cooling rate of $10 \text{ K}\cdot\text{min}^{-1}$. All samples had been dried in a vacuum oven at 23°C for 3 h prior to DSC measurement. DMA on the composites was performed on a Q800 (TA Instruments, USA) calibrated with standardized steel plates by TA instruments. The temperature calibration of the DMA was performed using an indium standard. The specimens were tested in transverse fibre direction using a single cantilever bend mode with an amplitude of $20 \mu\text{m}$. The fre-

quency was set to 1 Hz and the heating rate was $1 \text{ K}\cdot\text{min}^{-1}$.

The scanning electron microscopy (SEM) micrographs were obtained using an Ultra 55 (Carl Zeiss SMT AG, Germany), after sputtering a 5 nm thick platinum layer onto the samples. The molecular weight of the matrix PP and the PP film former was determined by high temperature gel permeation chromatography (HT-GPC) at 150°C on a GPC220 (Varian Inc., USA) equipped with 2 PL mixed B LS columns using triple detection (refractive index, light scattering, and viscosity). 1,2,4-trichlorobenzene was used as solvent and eluent with a flow rate of $1 \text{ ml}\cdot\text{min}^{-1}$.

2.3. Statistical analysis of the factorial design

Composites with different sizing formulations and varying GF diameters, according to a three level, three-factor factorial design, were prepared. The chosen Box-Behnken design resulted in 15 experiments shown in Table 1. Besides the stepwise variation of the average GF diameter, the amount of silane and film former within the sizing formulation were changed. In the case of the GF diameter the indications ‘-’, ‘0’, and ‘+’ are related to diameters of 11 , 13 and $16.5 \mu\text{m}$, respectively. For the silane and film former the indications ‘-’, ‘0’, ‘+’ refer to 0 , 1.5 , $3.0 \text{ wt}\%$ and 1.75 , 7.875 , $17.5 \text{ wt}\%$ solid content of the sizing, respectively. In the case of the film former, the lower and upper concentration result in less than 0.5 and around $2 \text{ wt}\%$ of organic content on the GF, respectively. The statistical analysis of the experimental results was performed by analyzing the factorial design with a statistical software (Statgraphics, Centurion). By creating regression equations a model fit was obtained relating the results of the mechanical testing to main and secondary effects, respectively. The former ones are in this case the silane and film former content of the sizing as well as the GF diameter, whereas the secondary effects describe quadratic contributions of the main effects or interactions between different main effects. Analysis of variance (ANOVA) allows determining the statistical significance of each effect by comparing the mean square of the model fit against an estimate of the experimental error. If the resulting P-values for the observed effects are less than 0.05 this is an

indication that they are significantly different from zero at the 95% confidence level. Moreover, the correlation coefficient R^2 for the model is calculated providing a measure for the accuracy of the model fit. In order to establish a ranking of the importance of the observed effects, Pareto charts [34] can be created showing the statistical significance of each effect as a measure of its standardized effect.

3. Results and discussion

3.1. Statistical analysis: Effect of factor variation on composite interfacial strength

Following the factorial design and the stepwise variation of the three factors, the estimated response surfaces represent the best fit to the experimentally obtained values. Figure 1a shows the estimated response surface for the transverse tensile strength as a function of silane and film former contents in the sizing. It can be seen that the transverse tensile strength is highly influenced by the silane content. For the sizings without silane, the transverse tensile strength is found to range at very low values of about 5 MPa. However, at 1.5 wt% silane the transverse tensile strength has considerably improved, being between 20 and 25 MPa. A further increase of the silane content did not result in enhanced composite strength, the values are comparable to those at 1.5 wt% silane, however, the estimated response surface indicates maximum composite strengths between 1.5 and 3 wt% silane. This is related to the parabolic fitting of the estimated surface, although it has been reported that excess silane results in an increased build-up of physisorbed silane layers which can lower the interfacial strength [10, 35].

Regarding the film former, at all silane contents investigated a slight increase of the transverse tensile strength with decreasing film former content can be observed (Figure 1a). However, the effect is much less pronounced than the one of the silane content. The effect of the GF diameter is also statistically significant, but less important for the transverse tensile strength than that of the film former. The regression equation for the estimated response surface of the transverse tensile strength, σ_{90° , is given by Equation (1):

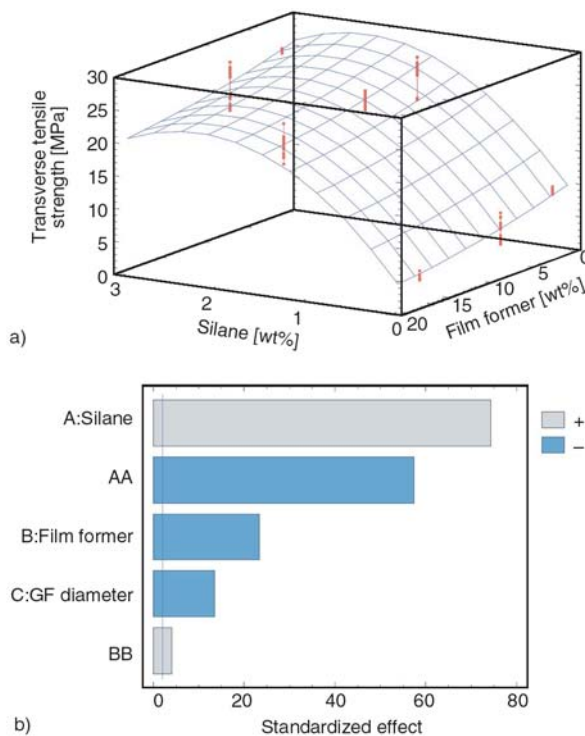


Figure 1. a) Estimated response surface for the transverse tensile strength of the GF/PP composites. The GF diameter was hold constant at 13 μm . The wt% of silane and film former refers to the solid content of the applied sizings. b) Pareto chart showing the statistically significant effects for the transverse tensile strength of the GF/PP composites. A, B, and C denote the main effects (silane and film former content of the sizing, and GF diameter). Statistically significant secondary effects, describing quadratic contributions of the main effects or interactions between different main effects, respectively, are denoted by a two-letter combination of the corresponding main effects.

$$\sigma_{90^\circ} = 16.1 + 16.86 \cdot A - 0.43 \cdot B - 0.47 \cdot C - 3.8 \cdot A^2 + 0.01 \cdot B^2 \quad (1)$$

where A denotes the silane and B the film former content of the sizing, respectively. Both quantities refer to wt% relative to the solid content of the sizings. C is the GF diameter in μm . For Equation (1), the corresponding correlation coefficient R^2 is 0.98. For the discussion of the statistical significance of the main and secondary effects the Pareto chart, presented in Figure 1b, gives a clear indication which factors are of importance to the transverse tensile strength. It shows the ranking of all statistically significant effects with P-values well below 0.05. This includes the main effects, like the amount of silane and film former in the sizing and the GF

diameter, but as well possible quadratic contributions of the main effects like AA and BB, reflected in the curved shaped of the estimated response surface. Moreover, interactions between the main effects, e.g. AB, could be displayed, but those were found not to be significant for the transverse tensile strength. The limit for the statistical significance is indicated by the vertical line in the Pareto chart. As can be seen in Figure 1b, the silane content has the largest influence of all main effects, followed by the film former content and the GF diameter. For the latter one a linear correlation with the transverse tensile strength is found, whereas the other main effects are non-linear. The ‘+’ and ‘-’ in the Pareto chart indicate a positive and negative correlation with the transverse tensile strength, respectively. To put it simply, it can be summarized that a higher silane content in the sizing has a beneficial effect on the transverse tensile strength, whereas an increased film former content as well as a higher GF diameter result in lower values.

Similar to the transverse tensile strength, the dependence of the CST on the main effects was analyzed. Figure 2a shows the estimated response surface as a function of solid content of silane and film former in the sizing. Again, the lowest CST values are found for the sizings without silane, however, compared with Figure 1a the influence of the film former is much more pronounced. While for the transverse tensile strength different film former contents in the sizings affect the absolute values only to a minor extent, the CST is found to be very sensitive to a variation in the film former content of the sizing. Figure 2b shows the ranking of the statistical significance for the fitted estimated response surface in Figure 2a. Among the main effects, the film former is found to be the most significant factor, followed by the GF diameter and the silane content, respectively. Moreover, compared with the Pareto chart of the transverse tensile strength all secondary effects are found to be of statistical significance and contribute to the obtained results. This serves as a good example to demonstrate possible difficulties upon the interpretation of Pareto charts and the related estimated response surfaces. While the statistical analysis aims at the best fit of the experimental results, including secondary interactions as factors in the regression equation, their physical interpretation is not always straightforward. However, for the sake of com-

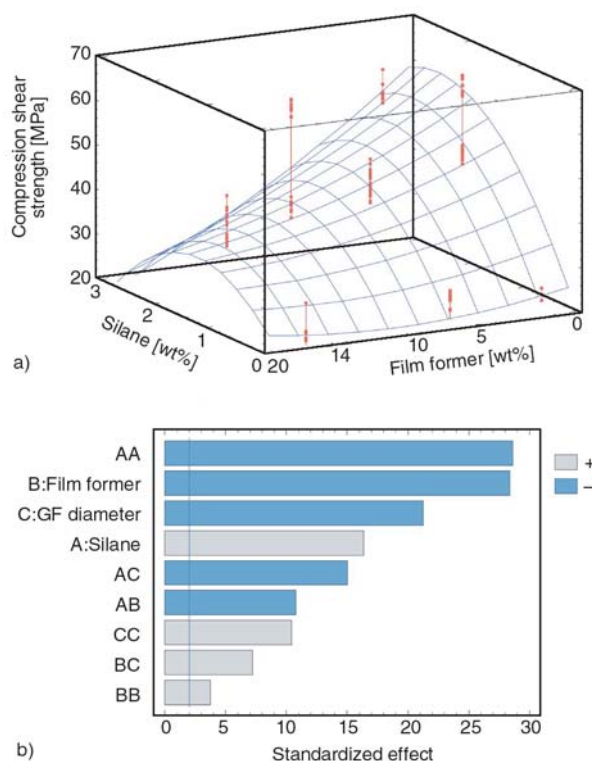


Figure 2. a) Estimated response surface for the compression shear strength of the GF/PP composites. The GF diameter was hold constant at 13 μm. The wt% of silane and film former refers to the solid content of the applied sizings. b) Pareto chart showing the statistically significant effects for the compression shear strength of the GF/PP composites. A, B, and C denote the main effects (silane and film former content of the sizing, and GF diameter). Statistically significant secondary effects, describing quadratic contributions of the main effects or interactions between different main effects, respectively, are denoted by a two-letter combination of the corresponding main effects.

pleteness the Pareto charts in Figure 1b and 2b show all statistically significant effects with P-values below 0.05. As can be seen in Figure 2b, for all three main effects a quadratic interaction can be found. However, in the case of the silane this is questionable since no experimental results are available for the high silane together with high film former contents in the sizing (cf. Table 1).

The regression equation for the best fit of the compression shear strength, σ_{CST} , is described by Equation (2):

$$\sigma_{CST} = 173.9 + 46.04 \cdot A - 2.02 \cdot B - 20.86 \cdot C - 5.9 \cdot A^2 - 0.66 \cdot A \cdot B - 1.32 \cdot A \cdot C + 0.03 \cdot B^2 + 0.1 \cdot B \cdot C + 0.73 \cdot C^2 \quad (2)$$

Table 1. Experimental matrix using a three level, three-factor factorial design, resulting in 15 experiments. ‘+’, ‘0’, and ‘-’ indicate a high, intermediate and low level of the factor. For the amount of silane and film former the indications ‘-’, ‘0’, ‘+’ refer to 0, 1.5, 3.0 wt% and 1.75, 7.875, 17.5 wt% solid content of the sizing, respectively. In the case of the GF diameter the indications ‘-’, ‘0’, and ‘+’ are related to diameters of 11, 13 and 16.5 μm , respectively. The sizing of experiment 5 was not applicable for spinning of the GF, since a significant increase in viscosity upon mixing of silane and film former was observed.

Experiment	Factors		
	Amount of silane	Amount of film former	Glass fibre diameter
1	0	0	0
2	-	-	0
3	+	-	0
4	-	+	+
5	+	+	0
6	-	0	-
7	+	0	-
8	0	0	0
9	-	0	+
10	+	0	+
11	0	-	-
12	0	+	-
13	0	-	+
14	0	+	+
15	0	0	0

For the fit of the CST by Equation (2) the coefficient of correlation is 0.98.

3.2. Effect of sizing formulation and glass fibre diameter on the composites interfacial strength

The statistical analysis of the influence of the main effects highlighted their significance for transverse and compression shear strength of the composites. However, depending on the applied test method, the contribution of the main effects to the observed results is different. It should be noted that both test methods are primarily sensitive to the interphase region. As the fibre volume content and fibre orientation are comparable for all specimens tested, the results reflect the changes in the interphasial strength of the composites.

Not surprising, the absence of silane in the sizing results in composites with very poor mechanical performance. Without silane as adhesion promoter no covalent bonding between the fibre and matrix can be achieved. If silane is present, after hydrolysis of the alkoxy groups, covalent interactions with the inorganic surface of the GF are formed while its organofunctional groups can react with the matrix. The mechanical performance of the composites with an intermediate and high silane content in the sizing is similar, although the estimated response

surfaces suggest a maximum at silane contents between 1.5 and 3 wt%. It should be taken into account, that the intermediate concentration of 1.5 wt% silane was selected owing to the convention for response surface designs to choose the intermediate level as the arithmetic average between the lower and upper limit. However, in our earlier studies, lower silane concentrations around 1 wt% were found to yield similar mechanical performance for this system [31]. Therefore, the increased mechanical performance of the composites related to the silane content in the sizing could possibly be shifted towards lower silane contents. Moreover, for both regression equations the highest composite performance is predicted for the lower limits of the film former content and GF diameter in combination with silane contents between the intermediate and upper level. The physical significance of the proposed amount of silane is questionable, since this could be due to the parabolic nature of the model fit. However, it is known that excessive silane in sizings results in an increasing amount of physisorbed silane which can deteriorate the composite properties [10, 35].

Figure 3 shows SEM micrographs of fractured surfaces of the composites with different sizing formulations after compression shear testing. In Figures 3a and 3b the fractured surfaces of a composite with an intermediate silane and low film former

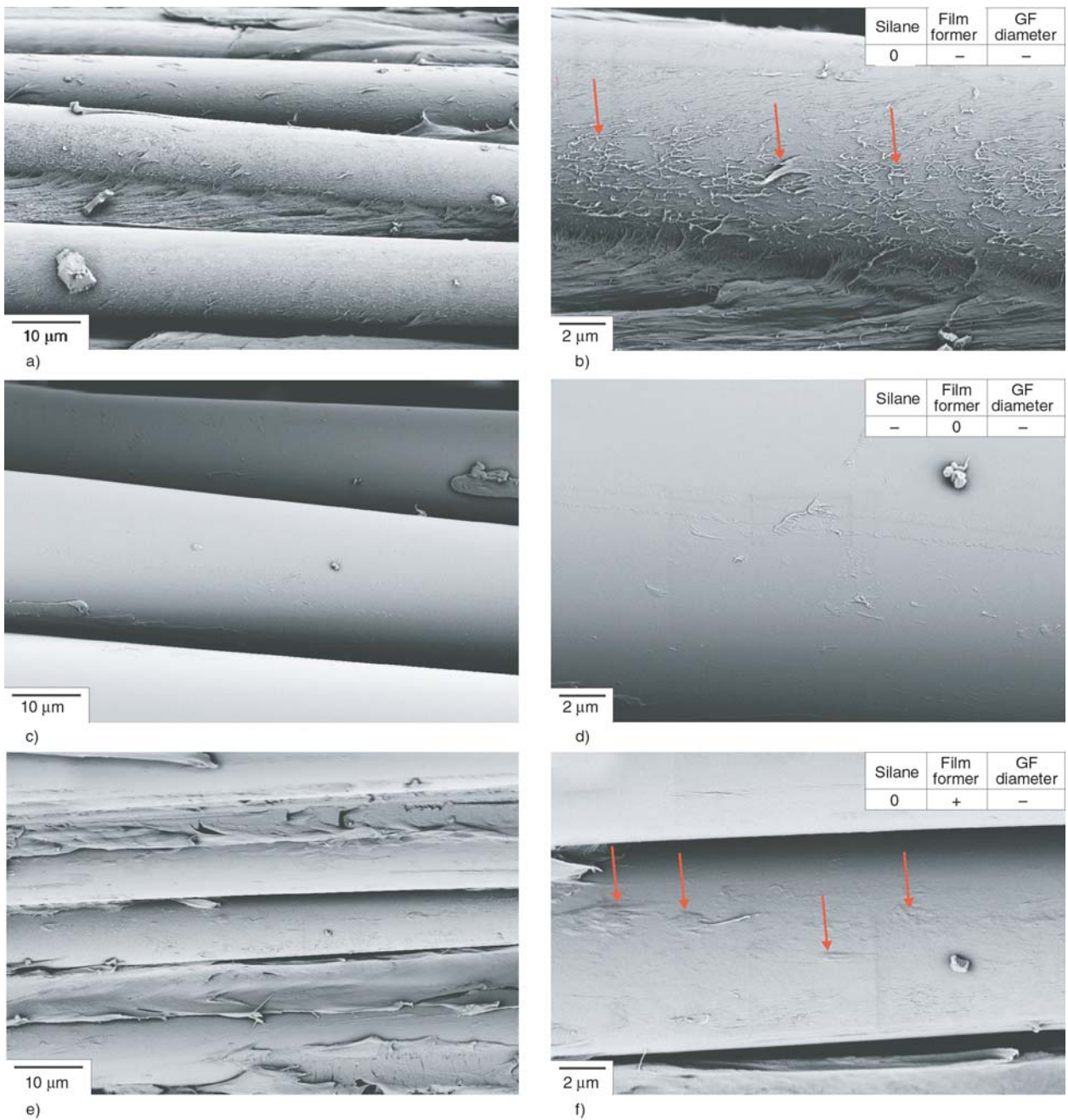


Figure 3. SEM micrographs of fractured surfaces of unidirectional composites with different sizing formulations after compression shear testing. a), b): Experiment 11 – intermediate silane and low film former content. c), d): Experiment 6 – low silane and intermediate film former content. e), f): Experiment 12 – intermediate silane and high film former content.

content are shown. The characteristic feature of the fractured surfaces of this composite is an irregularly shaped GF surface with attached PP, clearly indicating the intense plastic deformation of the matrix PP next to the GF (marked with red arrows). The average CST of this composite was determined to be 63.7 ± 1.7 MPa. For the sizing formulation without silane a drastic reduction in CST to 25.3 ± 2.5 MPa was determined. The associated fractured surfaces show a distinct picture with

almost bare GF (cf. Figures 3c and 3d). This is indicative of an adhesive failure, related to the absence of the silane and the resulting poor GF/matrix adhesion. The micrographs of Figures 3e and 3f represent fractured surfaces of the composite with a CST of 42.1 ± 1.8 MPa owing to intermediate silane and high film former content in the sizing. Although SEM analysis of fractured surfaces is limited to qualitative conclusions, a distinct fracture mechanism compared to that of Figures 3a

and 3b predominates, resulting obviously in lower CST values. Compared to the fractured surface of the specimen with the low film former content in Figures 3a and b, here, a different type of cohesive failure can be observed. Attached PP on the GF can be seen indicating a good bonding of the GF to its vicinity (marked with red arrows). However, the PP residues on the GF appear to be relatively homogeneous and show less plastic deformation than in Figures 3a and 3b. If a thicker film former layer on the GF is present, the GF/matrix interface is not necessarily the weakest region and failure can start within the film former layer due to insufficient shear strength of the film former PP or at the film former/matrix interface. It is known that upon consolidation of the composites the interdiffusion of the GF sizing and matrix polymer results in the formation of the interphase affecting the IFSS of composites [5]. For GF with a thicker film former layer the property gradient in the interphase is more pronounced since the range of interdiffusion is limited. As a consequence, in the vicinity of the fibre the interphalial properties are mainly determined by those of the film former, whereas with increasing distance to the GF interdiffusion with the matrix results in graded properties. This is similar to the results observed in [36], where for model composites made of GF/atactic PP (aPP) a cohesive failure was found indicating a strong fibre/matrix interface. However, the interfacial shear strength was limited by the insufficient matrix shear strength of the aPP resulting in poor overall values.

As can be inferred from the analysis of the main effects on the transverse tensile and compression shear strength, the latter one is much more sensitive to a variation in the film former content. The tensile load in transverse fibre direction results in a Mode I state of stress. This causes composites with strong interphases to fail at around 25 MPa, which is relatively close to the yield stress of neat PP of around 30 MPa. For the CST, values between 22 and 63 MPa were observed and certain specimens showed some extent of plastic deformation in the load transmission region before they failed. Therefore, the state of stress is different from that of the transverse tensile stress and turns the film former related interphase thickness into the main factor for the load bearing capacity of the composites.

Besides the sizing formulation, the GF diameter, as the third factor, was also found to be of statistical

significance for the mechanical properties of the composites. Both, transverse tensile and compression shear strength were found to increase with decreasing GF diameter. As both test methods are related to the interphalial properties, differences in GF strength associated with decreasing diameter of the GF can not account for the results. However, bearing in mind the constant GF weight fraction of 75%, the interfibre distance decreases with decreasing GF diameter. Assuming inhomogeneities in the GF distribution, this results in matrix rich regions of larger dimensions for the specimens with the bigger GF diameters, compared to those with the smaller ones. A second issue related to a decreasing GF diameter is the specific surface. Decreasing the GF diameter from 16.5 to 11 μm entails a gain in specific surface of 50%. In this context, assuming a constant weight fraction of organic content of the fibre as well as a homogeneous coverage of the GF by the sizing, the thickness of the sizing layer on the GF increases for higher diameters. This effect is similar to an increased amount of film former in the sizing for constant GF diameter, which was shown previously to weaken the interphalial strength of the composites (cf. Figures 1 and 2).

The thickness of the sizing layer, d_{siz} , can be estimated as a function of the GF diameter, d_{GF} , and the weight fraction of organic content on the fibre, M_{siz} . The idealized cross sectional area of a sized GF, A_{GF-siz} , is composed of the cross sectional area of the GF itself, A_{GF} , and the additional cross sectional area due to the sizing, A_{siz} . Replacing A_{siz} by the density ratio between GF and sizing, ρ_{GF}/ρ_{siz} , and multiplied by M_{siz} and A_{GF} , A_{GF-siz} can be written as Equation (3):

$$A_{GF-siz} = A_{GF} + \frac{\rho_{GF}}{\rho_{siz}} \cdot M_{siz} \cdot A_{GF} \quad (3)$$

As A_{GF-siz} and A_{GF} can be expressed by π times the corresponding radius squared, the only unknown quantity in Equation (3) is the radius of the sized GF, r_{GF-siz} . Rearranging the equation, r_{GF-siz} becomes Equation (4):

$$r_{GF-siz} = \sqrt{\frac{A_{GF} \cdot \left(\frac{\rho_{GF}}{\rho_{siz}} \cdot M_{siz} + 1 \right)}{\pi}} \quad (4)$$

Now, the thickness of the sizing layer, assuming homogeneous coverage of the GF, can be calcu-

lated by subtracting the radius of the GF, r_{GF} , from the radius of the sized GF, r_{GF-siz} . For the density of the GF and the sizing, values of 2.56 and 0.95 g/cm³, respectively, were used. Based on this estimation, Figure 4 shows the dependency of the sizing thickness on the GF diameter for different weight fractions of organic content on the fibre. From Figure 4 it can be seen that for constant organic contents on the GF the sizing thickness increases linearly for increasing GF diameters. For the composites prepared in this study, the variation of organic contents between 0.5 and about 2 wt%, respectively, theoretically causes differences in the average sizing thickness in the range of 300%. Moreover, the slope of the increase in thickness is steeper for higher weight fraction of organic content on the GF. As a maximum, considering 2 wt% weight fraction of sizing on the fibre and taking the experimentally varied diameters of 11 and 16.5 μm ,

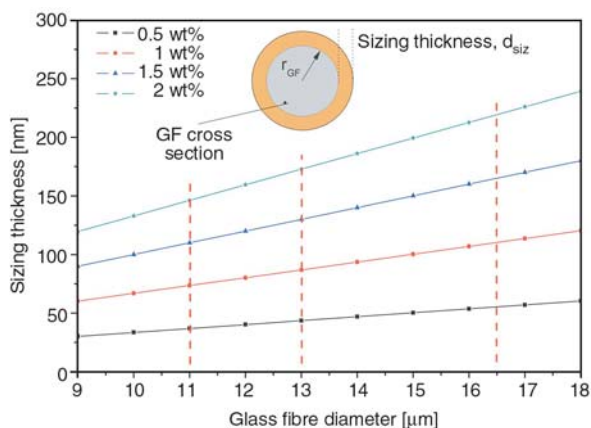


Figure 4. Calculated dependence of the sizing thickness on the GF diameter for different weight fractions of organic content on the GF assuming a homogeneously covered fibre. The vertical dotted lines represent the GF diameters, realized by stepwise variation of the haul-off speed during GF-spinning, i.e. lower, intermediate and high level of this factor. Similarly to this, 0.5 and 2 wt% organic content represent the upper and lower limits of the sizing content on the GF used for the manufacturing of the composites.

respectively, the sizing thickness increases from 146 to 219 nm, corresponding to an increase of 50%. This explains why the GF diameter as one of the main effects in the factorial design can affect the composite strength similarly as the film former content in the sizing.

3.3. Micro mechanical characterization of selected composites

Besides the characterization of the composites in terms of transverse tensile and compression shear strength, micromechanical testing by means of SFPO tests was conducted in order to investigate the relationship between sizing formulation and adhesion strength for model composites. Four sets of differently sized GF were compared, only being different in terms of silane and film former content. During embedding, extreme care was taken to realize identical parameters, as it is known that a variation in temperature and atmosphere can affect the thermo-oxidative degradation of the small amount of matrix to a different extent. For the given matrix system this was evidenced by GPC measurements on SFPO samples embedded at different temperatures and atmospheres (results not discussed in detail here). Under Argon atmosphere, a change in embedding temperature from 255 to 230°C resulted in M_w of 136 300 and 156 300 g/mol, respectively. Embedding at 255°C under ambient atmosphere without Argon results in a reduction of M_w to 112 200 g/mol. For the SFPO data presented in this study, all specimens were embedded under Argon atmosphere at 255°C.

Table 2 shows the IFSS determined by SFPO measurements from the maximum force of the force-displacement curve divided by the perimeter of the embedded GF, as well as the corresponding data of the macro mechanical testing. From the SFPO data it can be inferred that changes in silane or film former content of the sizings are reflected in the IFSS

Table 2. Mechanical properties of selected composites based on micro and macro mechanical characterisation. For the amount of silane and film former the indications ‘-’, ‘0’, ‘+’ refer to 0, 1.5, 3.0 wt% and 1.75, 7.875, 17.5 wt% solid content of the sizing, respectively.

Experiment	Sizing		Interfacial shear strength [MPa]	Transverse tensile strength [MPa]	Compression shear strength [MPa]
	Silane	Film former			
6	-	0	3.2 ± 1.3	8.0 ± 0.8	25.3 ± 2.5
7	+	0	8.4 ± 2.3	25.2 ± 0.6	53.2 ± 1.4
11	0	-	7.2 ± 1.3	26.4 ± 0.4	63.4 ± 1.7
12	0	+	5.2 ± 1.4	22.1 ± 0.4	42.1 ± 1.8

of the samples showing a similar trend as for the macro mechanical testing data. The presented data agrees fairly well with results from literature [36] on the interfacial shear strength of GF/PP model composites. However, in contrast to the manuscript of Hoecker and Karger-Kocsis [36] the amount of film former was varied but not the processing conditions. Thus, the observed effect is mainly related to the thickness of the interphase, whereas the supramolecular structure of the PP is assumed to be similar for all cases. Moreover, for high film former contents the interphase is rather thick. Consequently, the ‘bulk-properties’ of the film former are more important due to the limited interdiffusion between matrix and sizing in the vicinity of the glass fibres, whereas for systems with low film former contents interdiffusion between matrix and sizing results in interphase with more graded properties.

Figure 5 relates the IFSS to the macro mechanical properties of the composites. For both test methods a correlation between the micro and macro mechanical properties can be seen. In the case of SFPO and transverse tensile strength the state of stress upon failure initiation is similar to Mode I [37]. Thus, a correlation between the two sets of data is not surprising. However, although the loading of the specimens for the CST testing is different from Mode I and plastic deformation before failure was found in the load transmission region, a similar trend as for the transverse tensile strength is observed.

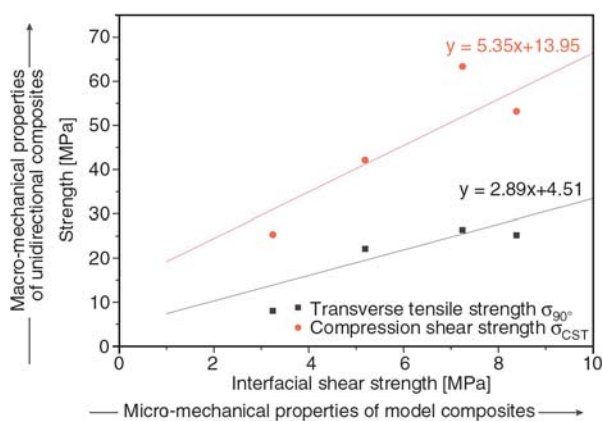


Figure 5. Correlation of the macro mechanical strength of the composites with the IFSS determined by SFPO tests on model composites

3.4. Dynamic mechanical and thermal characterization of selected composites

Besides the quasi-static characterization of composites, DMA was used to investigate the dynamical properties of the continuous fibre reinforced composites, influenced by different silane and film former contents. All samples were tested perpendicular to the fibre direction. Thus, the specimens can be regarded as a series connection of the elements GF-interphase-matrix-interphase. This allows to preferably detect interphase related differences, as not the GF stiffness is dominating the composites response like it is the case when testing in 0° direction of the fibres. Figure 6 shows the storage modulus and $\tan\delta$ of selected composites with different silane and film former concentrations in the GF sizing. Taking a closer look at the storage modulus of the samples, it can be seen that one specimen strongly deviates in its behaviour from the others. Commonly, differences in storage modulus of fibre reinforced composites are related to issues like fibre weight fraction and fibre orientation, respectively, but here they do not account for the observed results as those factors are comparable for all composites tested. The main difference of this sample (experiment 6) compared to the others is that no silane was used in the sizing. As shown before for the quasi-static testing, sizings without silane result in very poor mechanical values (cf. Table 2). Here, at -50°C, the storage modulus is about 6 GPa, whereas the other specimens with an intermediate or high silane content show values in

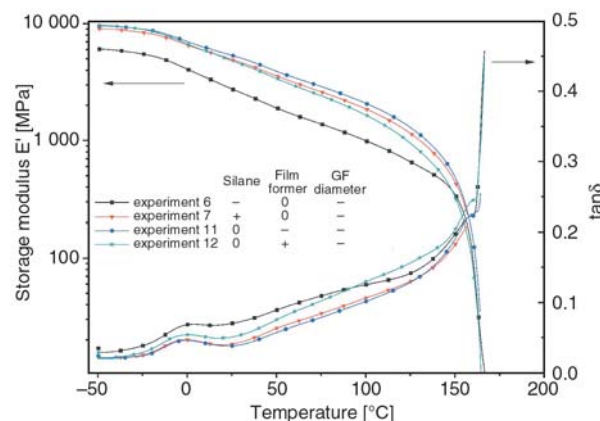


Figure 6. Storage modulus and $\tan\delta$ of unidirectional GF/PP composites with 75 wt% GF. Specimens were tested in 90° direction.

the range of 9 GPa. Obviously, the absence of silane affects the interphasial stiffness in a way that the storage modulus is shifted to lower values because no covalent bonding between GF and matrix takes place. At first glance, the other samples show comparable properties, however, above the glass transition temperature differences between the samples can be observed becoming more pronounced with increasing temperature. Although the absolute differences are relatively small they were confirmed by repeated measurements. Interestingly, the sample with the lowest film former content shows the highest storage modulus, followed by the ones with an intermediate and high level, respectively. This supports the findings of the quasi-static testing that a high film former content on the GF is not beneficial for the mechanical properties of a composite. GPC measurements revealed a lower molecular weight, M_w , of the film former compared to the matrix PP. M_w was found to be 217 600 and 147 600 g/mol for the PP matrix and the PP film former, respectively. Additionally, the melting behaviour of the film former and the matrix PP was characterized by DSC measurements and is shown in Figure 7. For the matrix PP the melting temperature was found to be 168.3°C, whereas the melting temperature of the film former is approximately 8K lower. Taking a melting enthalpy of 207 J/g for a 100% crystalline PP [38], the crystallinity of the film former and the matrix PP calculate to 27 and 48%, respectively. As the crystallinity of the film former is considerably lower, the presence of the film former in the interphase results in a higher content of amorphous PP, thus lowering the storage modulus of the composites. Therefore, thicker interphases due to a higher film

former content on the GF affect the storage modulus.

4. Conclusions

According to a three level, three factor factorial design composites with different interphasial properties have been characterized by micro and macro mechanical test methods. The Pareto charts identify all three main effects as statistically important to the results of both transverse tensile and compression shear strength. Generally, sizings without silane coupling agents resulted in very poor mechanical performance, but no differences were found between the intermediate and high level of silane concentration in the sizing with regard to the mechanical properties. The film former concentration and GF diameter are negatively correlated with the interphasial strength of the composites, i.e. an increased film former concentration as well as an increased GF diameter were found to result in lower transverse tensile and compression shear strength, respectively. This is related to the fact that for constant sizing weight fractions on the fibres, a higher GF diameter is associated with a lower specific surface of the fibres, thus resulting in thicker average sizing layers on GF than compared to smaller diameters. As a consequence, the film former content and the GF diameter were found to affect the composite properties in the same way.

Interphase sensitive SFPO tests and the thereby obtained interfacial shear strength values support the conclusions derived from the factorial design approach on the continuous fibre reinforced composites. Moreover, the characterization of the thermal properties of both, PP film former and matrix PP, in combination with the determination of their molecular weight allows relating the properties of the film former to the interphasial behaviour, thus accounting for the different mechanical properties of the composites.

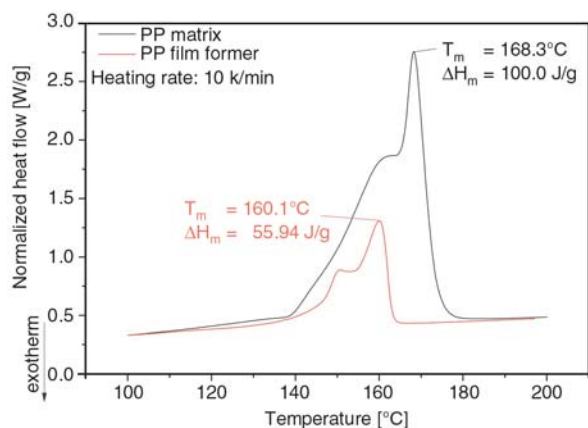


Figure 7. Thermal characterization of the melting behaviour of the PP film former and matrix PP

Acknowledgements

The authors are grateful for the support of this work by the Deutsche Forschungsgemeinschaft (DFG) within the framework of the collaborative research cluster SFB639 (subproject A1). Moreover, the authors are indebted to Dr. Häbler for performing the DMA and DSC measurements and helpful discussions.

References

- [1] Drzal L. T., Rich M. J., Lloyd P. F.: Adhesion of graphite fibers to epoxy matrices: I. The role of fiber surface treatment. *The Journal of Adhesion*, **16**, 1–30 (1982).
DOI: [10.1080/00218468308074901](https://doi.org/10.1080/00218468308074901)
- [2] DiBenedetto A.: Tailoring of interfaces in glass fiber reinforced polymer composites: A review. *Materials Science and Engineering A*, **302**, 74–82 (2001).
DOI: [10.1016/S0921-5093\(00\)01357-5](https://doi.org/10.1016/S0921-5093(00)01357-5)
- [3] Pukánszky B.: Interfaces and interphases in multicomponent materials: Past, present, future. *European Polymer Journal*, **41**, 645–662 (2005).
DOI: [10.1016/j.eurpolymj.2004.10.035](https://doi.org/10.1016/j.eurpolymj.2004.10.035)
- [4] Labronici M., Ishida H.: Toughening composites by fiber coating. A review. *Composite Interfaces*, **2**, 199–234 (1994).
- [5] Gao S-L., Mäder E.: Characterisation of interphase nanoscale property variation in glass fibre reinforced polypropylene and epoxy resin composites. *Composites Part A: Applied Science and Manufacturing*, **33**, 559–576 (2002).
DOI: [10.1016/S1359-835X\(01\)00134-8](https://doi.org/10.1016/S1359-835X(01)00134-8)
- [6] Zhao F. M., Takeda N., Inagaki K., Ikuta N.: A study on interfacial shear strength of GF/epoxy composites by means of microbond tests. *Advanced Composites Letters*, **5**, 113–116 (1996).
- [7] Mäder E., Pisanova E.: Characterization and design of interphases in glass fiber reinforced polypropylene. *Polymer Composites*, **21**, 361–368 (2000).
DOI: [10.1002/pc.10194](https://doi.org/10.1002/pc.10194)
- [8] Mäder E., Moos E., Karger-Kocsis J.: Role of film formers in glass fibre reinforced polypropylene – New insights and relation to mechanical properties. *Composites Part A: Applied Science and Manufacturing*, **32**, 631–639 (2001).
DOI: [10.1016/S1359-835X\(00\)00156-1](https://doi.org/10.1016/S1359-835X(00)00156-1)
- [9] Ishida H.: A review of recent progress in the studies of molecular and microstructure of coupling agents and their functions in composites, coatings and adhesive joints. *Polymer Composites*, **5**, 101–123 (1984).
DOI: [10.1002/pc.750050202](https://doi.org/10.1002/pc.750050202)
- [10] Zhuang R-C., Burghardt T., Mäder E.: Study on interfacial adhesion strength of single glass fibre/polypropylene model composites by altering the nature of the surface of sized glass fibres. *Composites Science and Technology*, **70**, 1523–1529 (2010).
DOI: [10.1016/j.compscitech.2010.05.009](https://doi.org/10.1016/j.compscitech.2010.05.009)
- [11] Mäder E., Rausch J., Schmidt N.: Commingled yarns – Processing aspects and tailored surfaces of polypropylene/glass composites. *Composites Part A: Applied Science and Manufacturing*, **39**, 612–623 (2008).
DOI: [10.1016/j.compositesa.2007.07.011](https://doi.org/10.1016/j.compositesa.2007.07.011)
- [12] Rausch J., Zhuang R. C., Mäder E.: Application of nanomaterials in sizings for glass fibre/polypropylene hybrid yarn spinning. *Materials Technology: Advanced Performance Materials*, **24**, 29–35 (2009).
DOI: [10.1179/175355509X418016](https://doi.org/10.1179/175355509X418016)
- [13] Rausch J., Zhuang R-C., Mäder E.: Surfactant assisted dispersion of functionalized multi-walled carbon nanotubes in aqueous media. *Composites Part A: Applied Science and Manufacturing*, in press (2010).
DOI: [10.1016/j.compositesa.2010.03.007](https://doi.org/10.1016/j.compositesa.2010.03.007)
- [14] Gao S., Mäder E., Plonka R.: Nanostructured coatings of glass fibers: Improvement of alkali resistance and mechanical properties. *Acta Materialia*, **55**, 1043–1052 (2007).
DOI: [10.1016/j.actamat.2006.09.020](https://doi.org/10.1016/j.actamat.2006.09.020)
- [15] Sureeyatanapas P., Young R. J.: SWNT composite coatings as a strain sensor on glass fibres in model epoxy composites. *Composites Science and Technology*, **69**, 1547–1552 (2009).
DOI: [10.1016/j.compscitech.2008.08.002](https://doi.org/10.1016/j.compscitech.2008.08.002)
- [16] Zhang J., Zhuang R. C., Liu J. W., Mäder E., Heinrich G., Gao S-L.: Functional interphases with multi-walled carbon nanotubes in glass fibre/epoxy composites. *Carbon*, **48**, 2273–2281 (2010).
DOI: [10.1016/j.carbon.2010.03.001](https://doi.org/10.1016/j.carbon.2010.03.001)
- [17] Gao S-L., Zhuang R-C., Zhang J-W., Liu J., Mäder E.: Glass fibers with carbon nanotube networks as multifunctional sensors. *Advanced Functional Materials*, **20**, 1885–1893 (2010).
DOI: [10.1002/adfm.201000283](https://doi.org/10.1002/adfm.201000283)
- [18] Rausch J., Mäder E.: Health monitoring in continuous glass fibre reinforced thermoplastics: Manufacturing and application of interphase sensors based on carbon nanotubes. *Composites Science and Technology*, in press (2010).
DOI: [10.1016/j.compscitech.2010.05.018](https://doi.org/10.1016/j.compscitech.2010.05.018)
- [19] Boudewijn J. R., Scholtens B. J. R., Brackman J.: Influence of the film former on fibre-matrix adhesion and mechanical properties of glass-fibre reinforced thermoplastics. *The Journal of Adhesion*, **52**, 115–129 (1995).
DOI: [10.1080/00218469508015189](https://doi.org/10.1080/00218469508015189)
- [20] Kim J-K., Sham M-L., Wu J.: Nanoscale characterisation of interphase in silane treated glass fibre composites. *Composites Part A: Applied Science and Manufacturing*, **32**, 607–618 (2001).
DOI: [10.1016/S1359-835X\(00\)00163-9](https://doi.org/10.1016/S1359-835X(00)00163-9)
- [21] Hodzic A., Kim J. K., Lowe A. E., Stachurski Z. H.: The effects of water aging on the interphase region and interlaminar fracture toughness in polymer-glass composites. *Composites Science and Technology*, **64**, 2185–2195 (2004).
DOI: [10.1016/j.compscitech.2004.03.011](https://doi.org/10.1016/j.compscitech.2004.03.011)
- [22] Häßler R., Mühlen E.: An introduction to μ TA™ and its application to the study of interfaces. *Thermochimica Acta*, **361**, 113–120 (2000).
DOI: [10.1016/S0040-6031\(00\)00552-9](https://doi.org/10.1016/S0040-6031(00)00552-9)
- [23] Mallarino S., Chailan J. F., Vernet J. L.: Interphase investigation in glass fibre composites by micro-thermal analysis. *Composites Part A: Applied Science and Manufacturing*, **36**, 1300–1306 (2005).
DOI: [10.1016/j.compositesa.2005.01.017](https://doi.org/10.1016/j.compositesa.2005.01.017)

- [24] Mäder E., Grundke K., Jacobasch H., Wachinger G.: Surface, interphase and composite property relations in fibre-reinforced polymers. *Composites*, **25**, 739–744 (1994).
DOI: [10.1016/0010-4361\(94\)90209-7](https://doi.org/10.1016/0010-4361(94)90209-7)
- [25] Mäder E., Jacobasch H., Grundke K., Gietzelt T.: Influence of an optimized interphase on the properties of polypropylene/glass fibre composites. *Composites Part A: Applied Science and Manufacturing*, **27**, 907–912 (1996).
DOI: [10.1016/1359-835X\(96\)00044-9](https://doi.org/10.1016/1359-835X(96)00044-9)
- [26] Wu H. F., Dwight D. W., Huff N. T.: Effects of silane coupling agents on the interphase and performance of glass-fiber-reinforced polymer composites. *Composites Science and Technology*, **57**, 975–983 (1997).
DOI: [10.1016/S0266-3538\(97\)00033-X](https://doi.org/10.1016/S0266-3538(97)00033-X)
- [27] Thomason J. L.: The interface region in glass fibre-reinforced epoxy resin composites: 3. Characterization of fibre surface coatings and the interphase. *Composites*, **26**, 487–498 (1995).
DOI: [10.1016/0010-4361\(95\)96806-H](https://doi.org/10.1016/0010-4361(95)96806-H)
- [28] Jones F. R.: Interphase formation and control in fibre composite materials. *Key Engineering Materials*, **116–117**, 41–60 (1996).
DOI: [10.4028/www.scientific.net/KEM.116-117.41](https://doi.org/10.4028/www.scientific.net/KEM.116-117.41)
- [29] Thomason J. L., Adzima L. J.: Sizing up the interphase: An insider's guide to the science of sizing. *Composites Part A: Applied Science and Manufacturing*, **32**, 313–321 (2001).
DOI: [10.1016/S1359-835X\(00\)00124-X](https://doi.org/10.1016/S1359-835X(00)00124-X)
- [30] Shokoohi S., Arefazar A., Khosrokhavar R.: Silane coupling agents in polymer-based reinforced composites: A review. *Journal of Reinforced Plastics and Composites*, **27**, 473–485 (2008).
DOI: [10.1177/0731684407081391](https://doi.org/10.1177/0731684407081391)
- [31] Mäder E., Rothe C., Brünig H., Leopold T.: Online spinning of commingled yarns- Equipment and yarn modification by tailored fibre surfaces. *Key Engineering Materials*, **334–335**, 229–232 (2007).
DOI: [10.4028/www.scientific.net/KEM.334-335.229](https://doi.org/10.4028/www.scientific.net/KEM.334-335.229)
- [32] Schneider K., Lauke B., Beckert W.: Compression shear test (CST) – A convenient apparatus for the estimation of apparent shear strength of composite materials. *Applied Composite Materials*, **8**, 43–62 (2001).
- [33] Mäder E., Gao S-L., Plonka R., Wang J.: Investigation on adhesion, interphases, and failure behaviour of cyclic butylene terephthalate (CBT®)/glass fiber composites. *Composites Science and Technology*, **67**, 3140–3150 (2006).
DOI: [10.1016/j.compscitech.2007.04.014](https://doi.org/10.1016/j.compscitech.2007.04.014)
- [34] Wilkinson L.: Revising the Pareto chart. *The American Statistician*, **60**, 332–334 (2006).
DOI: [10.1198/000313006X152243](https://doi.org/10.1198/000313006X152243)
- [35] Wu S.: *Polymer interface and adhesion*. Marcel Dekker, New York (1982).
- [36] Hoecker F., Karger-Kocsis J.: On the effects of processing conditions and interphase of modification on the fiber/matrix load transfer in single fiber polypropylene composites. *The Journal of Adhesion*, **52**, 81–100 (1995).
DOI: [10.1080/00218469508015187](https://doi.org/10.1080/00218469508015187)
- [37] Zhandarov S., Mäder E.: Characterization of fiber/matrix interface strength: Applicability of different tests, approaches and parameters. *Composites Science and Technology*, **65**, 149–160 (2005).
DOI: [10.1016/j.compscitech.2004.07.003](https://doi.org/10.1016/j.compscitech.2004.07.003)
- [38] Ehrenstein G. W., Riedel G., Trawiel P.: *Praxis der thermischen Analyse von Kunststoffen*. Hanser, München (2003).